CHAPTER I

INTRODUCTION

The goal of this research is to investigate the forces and torques of high speed friction stir welding. The observations are compared to a three dimensional fluid dynamic model. The results are used to develop a working parametric envelope for high speed friction stir welding in order to facilitate the implementation of the process to FSW capable robots. Furthermore, this research will assist in the development of empirical equations for the axial force and welding torque associated with friction stir welding.

Friction stir welding (FSW) was invented and patented by W. M Thomas et al. [1] of the Welding Institute in Cambridge, UK. In FSW, a cylindrical, shouldered tool with a profiled probe is rotated and slowly plunged into the joint line between two pieces of sheet or plate material, which are butted together. The pieces are rigidly clamped onto a backing plate in a manner that prevents the abutting joint faces from being forced apart. Frictional heat is generated between the tool shoulder and the work piece. This heat causes the latter to reach a visco-plastic state that allows traversing of the tool along the weld line. The plasticized material is transferred from the leading edge of the tool to the trailing edge of the tool probe and is forged by the intimate contact of the tool shoulder and the pin profile. It leaves a solid phase bond between the two pieces.

The industries which utilize FSW are the aerospace, railway, land transportation, shipbuilding/marine, and the construction industries. These industries have seen a push towards using lightweight yet strong metals such as aluminum. Many products of these

industries require joining three-dimensional contours, which is not achievable using friction stir welding heavy-duty machine tool type equipment with traversing systems which are limited to only straight line or two-dimensional contours.

For these applications, industrial robots would be a preferred solution for performing friction stir welding for a number of reasons, including: lower costs, energy efficiency, greater manufacturing flexibility, and most significantly, the ability to follow three-dimensional contours. This dissertation examines the forces and torques associated with the FSW process with respect to mechanistic process characterization, and considerations necessary for robotic implementation. It is shown that force control is an important requirement of robotic FSW.

CHAPTER II

BACKGROUND

To understand the process of friction stir welding and the focus of this research, it is worthwhile to define certain terminologies and their usage in this dissertation.

In FSW, the tool typically consists of a cylindrical shoulder with a profiled probe, also called the pin. The material or materials being welded can be called the work-piece, part, sample, or plate. The joint where the samples abutt is referred to as the weld line. The part used to support and clamp the sample is called the backing plate, backing bar, or anvil.

The tool rotates at an angular velocity given in revolutions per minute (RPM), which will be referred to as the rotational speed (RS). The translational velocity at which the tool travels along the weld line is called the feed rate or travel speed (TS), and will be given in millimeters per minute (mm/min), millimeters per second (mm/s), or inches per minute (ipm). The side of the weld where the angular velocity and forward velocity of the pin tool are additive is called the advancing or leading side. The other side where the angular velocity and translational velocity are in opposite directions is called the trailing or retreating side.

As shown in Figure 1, forces act in three dimensions. The forces along the X-axis, Y-axis, and Z-axis will be referred to as the translational (F_x), transverse (F_y), and axial force (F_z) respectively, and will be given in Newtons (N). The moment (Mz) about the axis of rotation will be referred to as the torque and given in Newton-meters (N-m).

Power will be given in Watts (N-m/s). Figure 1 shows a schematic of the process and the given terminologies.

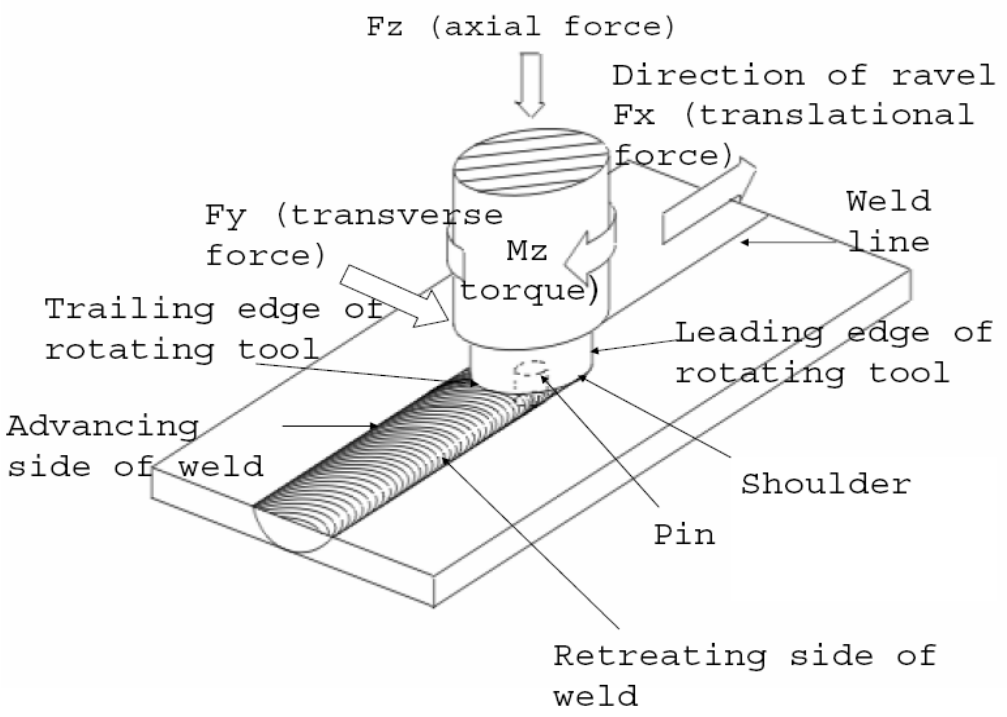

Figure 1: FSW Process Schematic.

Welding Materials

A wide range of materials can be successfully joined. These materials include thermoplastics, lead, zinc, aluminum alloys, copper, silver and gold. Materials with higher melting points (in excess of 1100°C) such as ferrous metals and alloys can also be joined. However they require probes of high temperature materials such as tungsten [1].

Aluminum has been welded in single passes ranging from 0.050" to 2" in thickness. Using a double pass method, welds up to 4" thick have been made [2].

Copper up to 2" thick has been welded. Welds up to 0.5" thick have been successfully made in steel using the double pass method, and 0.37" thick magnesium alloy AZ61A has been welded in a single pass [2].

Friction stir welding has successfully been performed in a variety of joint geometries. Butt welds, corner welds, T-sections, overlap welds, and fillet welds have all been done [2]. Circumferential welds have also been performed in the aerospace industry for the manufacture of large cryogenic tanks [3].

Welding Tools

A FSW tool may be made out of a number of different materials. Choice of a material for a tool is dependent on the type of metal material to be welded, particularly the melting temperature of the material. An additional consideration is the desired travel speed. Table 1 lists different tool material and the maximum operating temperatures [4].

The tool has two basic parts; the shoulder and pin. The tool shoulder has two general functions, create frictional heat at the tool/work piece interface and to cap the plasticized material as it is "stirred".

The pin is a cylindrical pin projecting from the distal shoulder surface and has a longitudinal axis co-extensive with the shoulder longitudinal axis. The pin must be large enough to stay above the plastic stress level at operating temperatures. Current FSW practice uses a pin having a surface profile consistent with the thread of a bolt, much like the end of a machine bolt [5]. The purpose of profiling the pin is to reduce traverse loads and improve material flow [4].

Table 1: Various tool materials [4].

Material	Approximate Max Work Temp (F)
H-13	1000
Ferro-TiC SK	1100
MP-159	1100
Stellite 6B	1600
Ferro-TiC HT-6A	1800
MAR-M-246	1900
Mo-TZM	2400
Rhenium	3600
Tungsten	3600

Tool pin shapes have taken the form of frusto-conical, inverted frusto-conical, spherical, and pear shape, to simple conical, truncated cones, to slightly tapered cylinders [5, 6]. Cocks et al. [7] introduced a pin which has a combined right handed and left handed thread pattern. This "enantionmorphic" pin is said to produce welds of improved mechanical properties [7].

In this research, a tool made of H-13 tool steel heat treated to Rc 48-50 with a 0.5" diameter cylindrical shoulder and a threaded cylindrical pin was be used.

Weld Microstructures

The heat and deformation generated during FSW produce four micro-structurally

distinct regions across the weld. They are the heat affected zone (HAZ), thermo-mechanically affected zone (TMAZ), dynamically recrystallized zone (DXZ) or weld nugget, and the unaffected material [8].

The HAZ is the outermost portion of the weld which is modified by the thermal field of the welding process but does not experience any deformation. It is similar to the heat affected zones observed in welds prepared by more conventional fusion welding processes. Inward from the HAZ is located the TMAZ, where the material experienced plastic deformation due to the stirring process in addition to the heat-induced micro-structural changes. At the center of the weld, where the heat and deformation are the greatest, aluminum alloys undergo significant grain refinement within an onion-shaped region called the weld nugget or DXZ, which is approximately the size of the rotating pin of the tool. The unaffected, or parent-material, is material that is heated but not modified by the thermal field of the weld.

Won-Bae Lee et al. [9] found that reaction layers consisting of mixed layers of elongated and ultra-fine grains of an intermetallic compound layer of Al4Fe with a hexagonal close-packed structure and a thickness of approximately 250 nm formed when austenitic stainless steel and Al alloy are friction stir welded. The elongated grains were shown to consist of a ferrite phase because of their ferromagnetism and a body-centered cubic crystal structure.

Mechanical Properties

In whole-weld tensile tests, most precipitation-strengthened aluminum alloys exhibit similar yielding and fracture behavior [10–13]. During these tests, the tensile

strain becomes localized in the HAZ on both sides of the weld nugget [14]. Fracture will typically occur at this location and will usually be located on the retreating side of the weld [13]. The localization of yield and fracture at the HAZ demonstrates the importance of this region in controlling the mechanical behavior of friction stir welds. Despite this, there have been few systematic examinations of the HAZ to determine the underlying cause of this behavior.

Some studies [10–12, 15–18] have demonstrated that precipitates are significantly coarsened in the HAZ relative to those observed in the unaffected base plate or weld nugget. Sato et al. [19] examined different locations in the HAZ and the weld nugget of AA 6063 FSW and observed that the precipitates experienced increasing dissolution toward the weld center. Su et al. [20] recently reported on precipitate evolutions occurring in AA 7050 FSW. They observed a coarsening of precipitates from the base plate into the TMAZ, with increasing dissolution and re-precipitation occurring from the TMAZ into the weld nugget.

Kwon et al. [21] investigated the influence of the tool rotational speed on the hardness and tensile strength of friction stir welded AL 1050 and concluded that the hardness within the weld was higher on the advancing side than on the retreating side. Also, that in the transition zone between the weld and the parent material the variation in hardness was more drastic on the advancing side than on the retreating side and that the hardness and tensile strength of the weld increased significantly with decreased tool rotation speed.

Lee et al. [22] examined the microstructure and mechanical properties of FSW AL 6005 alloy with increasing welding speed and concluded that the tensile strength

increased as welding speed increased.

Experimental and Theoretical Modeling

In this section, previous works pertaining to thermal-mechanical modeling will be reviewed. Since little is known about the physics involved during the FSW process, these works will help to provide insight into the mechanics of FSW.

Ulysse et al. [23] attempted to model the friction stir-welding process using three-dimensional visco-plastic modeling. The simulation was limited to one tool geometry where the tool pin was 6.4 mm (0.25") in diameter and its depth into the plate was 6.4 mm (0.25"), which is about 1/3 of the plate thickness. The pin was tilted by 3° from the vertical, leaning away from the direction of welding. The tool shoulder was 19 mm (0.75") in diameter. The shoulder face was a 7° concave cone design.

In the model, a cylindrical shoulder recess was assumed in order to approximate the shallow concave area as shown in Figure 2. The tool above the work surface was approximated as a 20 mm (0.79") high cylindrical shaft. The 3D finite-element (FE) friction stir-welding simulations were conducted using the commercial software FIDAP [24]. The mesh used for the FSW simulations are shown in Figures 2 and 3; about 33,000 eight-noded (brick) elements and 29,400 nodes were used in this study.

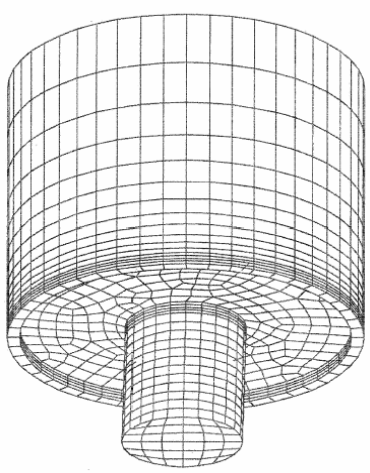

Figure 2: Enlarged view of Ulysse FSW tool FE mesh. [23]

In addition, only butt joints 19.1 mm (0.751") AA 7050-T7451 (2.3% Cu, 2.25% Mg, 6.2% Zn) thick plates were considered in this work. The model of the work-piece region was 60 mm (2.36") wide by 100 mm (3.94") in length as shown in Figure 3. The support table, located underneath the work-piece, is not included in the analysis in order to reduce the size of the numerical model. Therefore, heat transfer to the support table is ignored in this work.

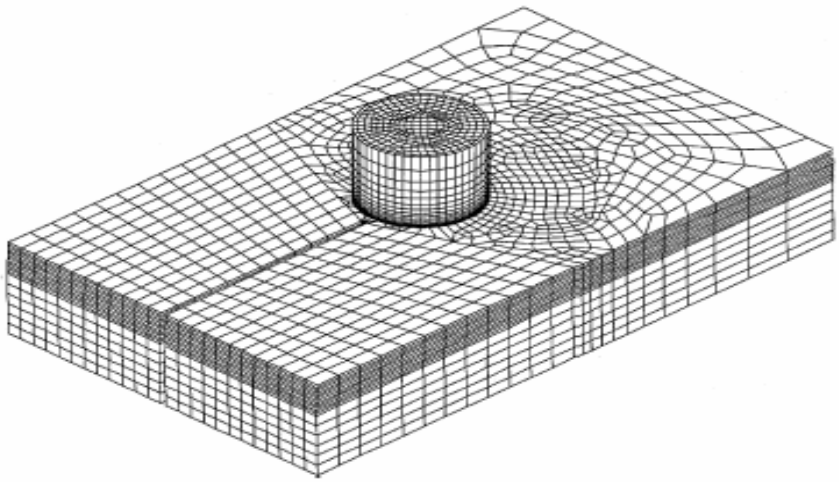

Figure 3: FE mesh of the welding model. [23]

Ulysse [23] modeled the large plastic deformation involved in stir-welding processes by relating the deviatoric stress tensor to the strain-rate tensor. The TMAZ was assumed to be a rigid-visco-plastic material where the flow stress depends on the strain-rate and temperature and is represented by an inverse hyperbolic-sine relation as follows:

$$\sigma_e = \frac{1}{\alpha}\sinh^{-1}\left[\left(\frac{Z}{A}\right)^{\frac{1}{n}}\right] \qquad Z = \dot{\varepsilon}\exp\left(\frac{Q}{RT}\right) \tag{1}$$

where α, Q, A, n are material constants, R the gas constant , T the absolute temperature, and Z is the Zener-Hollomon parameter. The material constants were determined using standard compression tests. The mechanical model equations are complete after appropriate boundary conditions are prescribed.

The temperature distribution is obtained by solving the energy equation, expressed here as the conductive–convective, steady-state equation

$$\rho c_p \cdot \nabla\theta = \nabla\cdot\left(k\nabla\theta\right) + \dot{Q} \tag{2}$$

where ρ is density, c_p the specific heat, u the velocity vector, k the conductivity, θ the temperature and Q is the internal heat generation rate. About 90% of the plastic deformation is assumed to be converted into heat. In this work, temperature-dependent conductivity and specific heat coefficients for aluminum alloys were adopted. The heat generation rate term can be expressed as the product of the effective stress and effective strain-rate [23].

Comparisons of model predictions with experimental data are illustrated in Figures 4. All temperatures are peak temperatures. The trend of the measured data is also indicated for convenience in the figures. The following parameters were used in the comparisons: (1.0 mm/s, 11.7 rev/s), (1.37 mm/s, 8.17 rev/s), (1.9 mm/s, 11.7 rev/s),

(3.54 mm/s, 8.17 rev/s), (2.593 mm/s, 11.7 rev/s), (3.54 mm/s, 8.17 rev/s), (3.54 mm/s, 25.5rev/s).

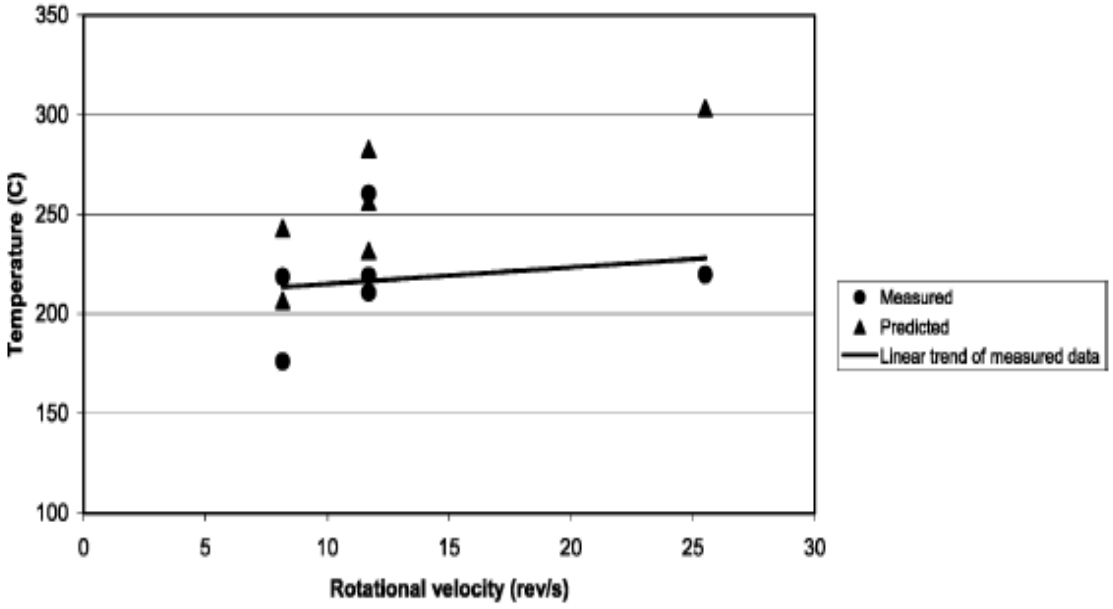

Figure 4: FSW temperatures as a function of tool rotational speed

While various temperature measurements were recorded, experimental measurements to validate the force predictions were not. Analytical predictions of axial (*Fz*) and shear forces on the pin are shown in Figure 4 and 5 as a function of translational speed and rotational speed respectively. It can be observed that increasing the welding speed, regardless of rotational speed, has the effect of increasing the axial force thrust and shear force on the pin. In addition, for a fixed welding speed, increasing the rotational speed has the effect of decreasing the forces. Quantification of this relation over a wide parametric range is the core topic of this dissertation.

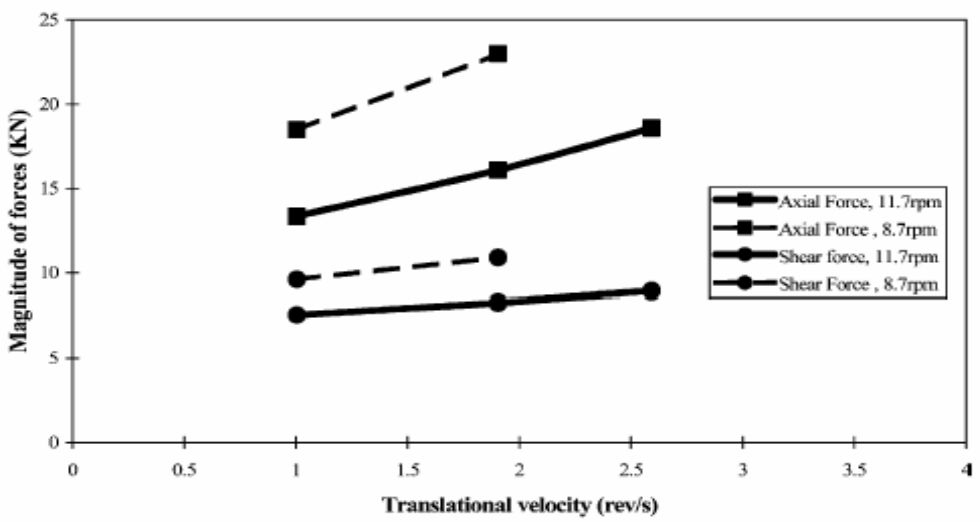

Figure 5: Axial (*Fz*) and shear forces on the pin shown as a function of translational speed. [23]

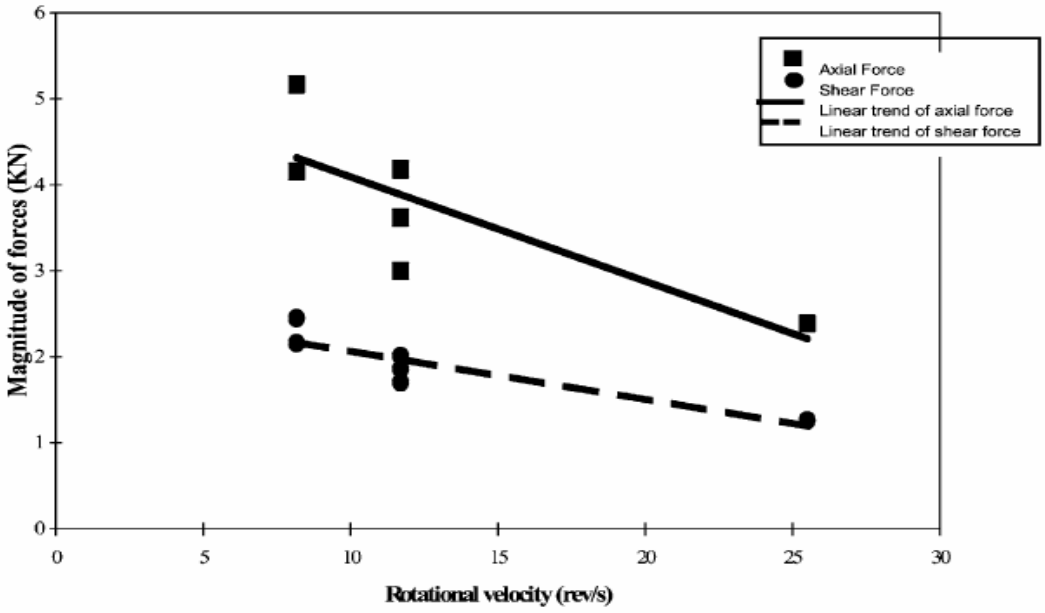

Figure 6: Axial and shear forces on pin as function of tool rotational speed. [23]

Reynolds et al. [25] introduced a two dimensional model based on fluid mechanics that modeled the solid state material transport during welding as a laminar

viscous flow of a non-Newtonian fluid past a cylinder. Only the tool pin was represented in the simulation. The temperature and strain rate dependent viscosity of AA6061 was based on the constitutive law of the flow stress of aluminum alloys using the Zener-Hollomon parameter (Z) (Eq. 1). Also, temperature dependent thermal conductivity and specific heat were used to calculate the heat transfer in the fluid. They concluded that the force against the welding direction at the pin increases with increasing translational speed at constant rotational speed and decreases with increasing rotational speed at constant travel speed.

Colegrove [26] used an advanced analytical estimation of the heat generation for tools with a threaded probe to estimate the heat generation distribution. The fraction of heat generated by the probe is estimated to be as high as 20%, which leads to the conclusion that the analytical estimated probe heat generation contribution is not negligible.

In parallel with the analytical model, Colegrove and Shercliff [26-27] developed a material flow model, which addressed the influence of threads on the material flow. An advanced viscous material model is introduced and the influence of different contact conditions are analyzed [27].

Schidmt et al. [28] sought to establish an analytical model for heat generation during friction stir welding based on different assumptions of the contact condition between the rotating tool surface and the weld piece. The material flow and heat generation are characterized by the contact conditions at the interface and are described as sliding, sticking or partial sliding/sticking. Different mechanisms of heat generation were found to be behind each contact condition. The analytical expression for the heat

generation in this work is a modification of previous analytical models known from the works by Colligan and Colegrove [29, 26]. In these works, both conical surfaces and different contact conditions were considered.

Chen et al. [30] introduced a three-dimensional model based on finite element analysis to study the thermal history and the thermo-mechanics in the butt-welding of aluminum alloy AA 6061-T6. The model incorporates the mechanical reaction of the tool and the thermo mechanics of the welded material. The heat source incorporated in the model involves the friction between the material and the pin and the shoulder. The dynamics of the FSW thermo-mechanical process, the thermal history and the evolution of longitudinal, lateral, and through-thickness stress in the friction stirred weld are simulated numerically. The X-ray diffraction (XRD) technique was used to measure the residual stress of the welded plate.

Chen et al. [30] suggested that the maximum temperature gradients in the longitudinal and lateral directions are located just beyond the shoulder edge, and that the longitudinal residual stress is greater than the lateral residual stress at the top surface of the weld. The prediction shows that the high stress is located in the region extending down from the crown to the mid-thickness of the weld. A higher traverse speed induces a larger high longitudinal stress zone and a narrower lateral stress zone in the weld.

Nunes et al. [31] modeled the tool torque to be totally due to the shear flow stress of the metal acting perpendicular to the direction of tool rotation and integrated over the surface. The welding power is equal to the torque multiplied by the RS and is given by

$$P = \omega_o M_z$$

$$M_z = \int_{R_p}^{R_s} 2\pi R_p \sigma dR_p + 2\pi R_p^2 t\sigma + \int_0^{R_p} 2\pi R_p^2 \sigma dR_p, \qquad (3)$$

where M_z is the welding torque, ω_o is the tool rotational speed, R_p is the pin radius, R_s is the shoulder radius, σ is the shear flow stress, and t is the pin depth. Figure 7 shows a comparison of the Mitchell et al. [32] experimental torques to torques computed from the Nunes et al. model [31].

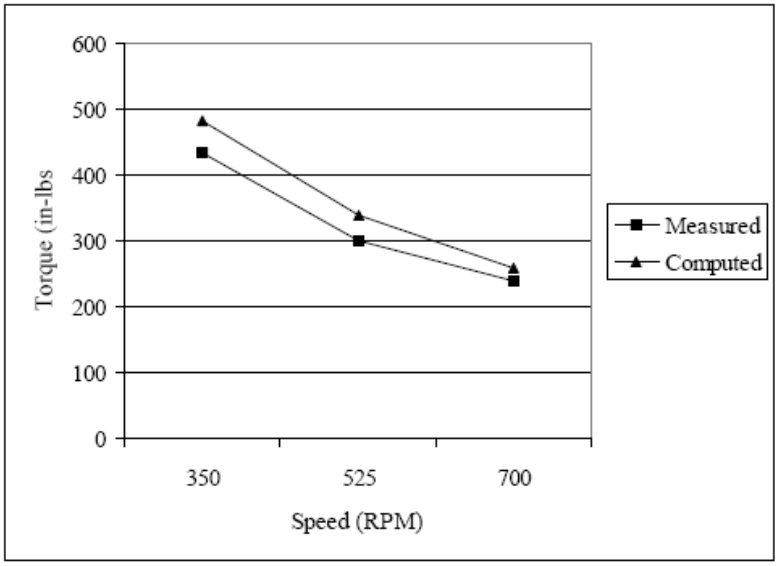

Figure 7: Comparison of experimental vs. rotating plug model computed torques [32].

Heurtier et al. [33] developed a three-dimensional thermo-mechanical model based on the velocity fields (momentum equations) used in classical fluid mechanics. By incorporating heat input from the tool shoulder and the plastic strain of the bulk material, the semi-analytical model can be used to obtain the strains, strain rates, and estimations of the temperatures and micro-hardness in the various weld zones. The calculated results were in good agreement with experimental measurements performed on an AA2024-T351 alloy friction stir welded joint.

Buffa et al. [34] developed a continuum based FEM model for friction stir welding. The model incorporated a 3D Lagrangian implicit, coupled, rigid-viscoplastic formulation and is calibrated by comparing the experimental results of force and temperature distribution. The model is used to investigate the distribution of temperature and strain in the heat affected zone and the weld nugget. The model correctly predicts the non-symmetric nature of the FSW process, and the relationships between the tool forces and the variation in the process parameters. Buffa et al. found that the effective strain distribution was non-symmetric about the weld line while the temperature profile was almost symmetric in the weld zone. They numerically modeled varying pin geometries (cylindrical and conical) and advancing speeds. The model used a thermo-mechanically coupled, rigid-viscoplastic, 3D FEM analysis to predict the process variables as well as the material flow pattern and the grain size in the weld joint [35]. The obtained results predict optimal tool geometry and advancing speed for improving nugget integrity of aluminum alloys.

Nandan et al. [36] solved the equations of conservation of mass, momentum, and energy in three dimensions using spatially variable thermo physical properties and non-Newtonian viscosity. The framework for the numerical solution of fluid flow and heat transfer was adapted from decades of previous work in fusion welding. Non-Newtonian viscosity for the metal flow was calculated considering strain rate, temperature, and temperature-dependent material properties. The computed profiles of strain rate and viscosity were examined in light of the existing literature on thermo-mechanical processing. The heat and mass flow during welding was found to be strongly three-dimensional. Significant asymmetry of heat and mass flow, which increased with

welding speed and rotational speed, was observed. Convective transport of heat was an important mechanism of heat transfer near the tool surface. The numerically simulated temperature fields, cooling rates, and the geometry of the thermo-mechanically affected zone agreed well with independently determined experimental values.

Flow Field Visualization

The visualization of material flow during friction stir welding is key to understanding the internal workings of the process and is critical to process modeling.

Nunes et al. [31] stated that the flow field around a standard threaded tool or tools with threadlike features is comprised of two parts. The primary flow of material is around the tool in the direction of rotation. There is a plug of metal that rotates with the pin, and the flow gradient goes from the velocity of the plug at the plug surface to zero some distance away. Also the plug radius occurs at a point that creates a minimum torque for a given shear flow stress. The plug hypothesis is supported by computational fluid dynamics work done by Reynolds's et al. [25], which predicted that a plug of metal rotates with the tool. The plug model can be seen below in Figure 8.

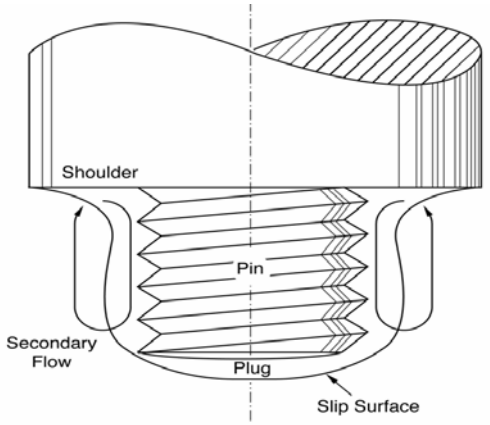

Figure 8: Secondary Flow Caused by Threads.

Ulysse [23] was able to extract useful information along the path line of a material particle traced in the welding region from the visco-plastic FSW model. The path line of a material particle located just underneath the pin tip was traced back to its original location in the shoulder recess. The temperature history of the particle along the path line is shown in Fig. 9. As seen in the figure, the particle was traced back in time from t = 2s (at the pin tip) to 0s (near the shoulder region).

For about 0.5 s, the particle rotates around the top of the pin with a relatively small downward or axial velocity *Uz*; and during this time, its temperature remains relatively uniform. After the initial 0.5 s, the particle follows the pin rotation and downward motion which sets up some periodicity in the temperature history.

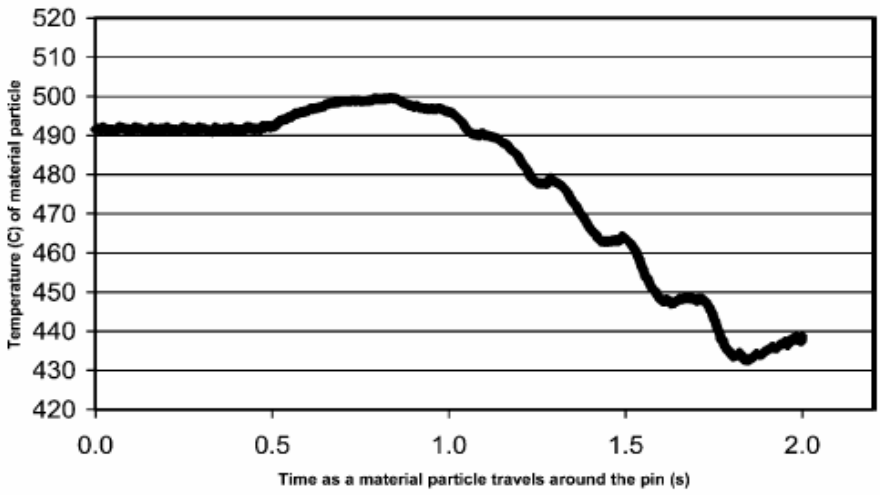

Figure 9: Temperature (°C) history of a material particle near the pin [23].

As the particle rotates, it crosses cold and hot regions located at the leading and trailing edges of the pin, respectively, which explains the peaks in Figure 9. The material particle is also pushed downward, toward the tip of the pin, where temperatures are relatively cold, which explains the decreasing trend in temperature.

Guerra et al. [37] investigated the flow of metal during FSW using a faying surface tracer and a pin frozen in place during welding. It was shown that the material is transported by a wiping of material from the advancing front side of the pin onto a zone of material that rotates and advances with the pin. The material undergoes a helical motion within the rotational zone that rotates, advances, and descends in the wash of the threads on the nib and rises on the outer part of the rotational zone. After one or more rotations, this material is sloughed off in the wake of the pin, primarily on the advancing side. The second process is an entrainment of material from the front retreating side of the nib that fills in between the sloughed off pieces from the advancing side.

Colligan et al. [29] followed material flow in AA 6061 and AA 7075 aluminum

by imbedding small steel balls as tracers into grooves cut into the work-piece parallel to the weld direction. Grooves were cut parallel to the weld direction but at various distances from the weld centerline and at various depths. After welding, the distribution of the steel balls was revealed by radiography in both the plane and the cross-sectional views. Results are displayed nicely in the original paper but, in general, the work showed that the material striking the pin on the advancing side of the weld would be displaced to the rear of the retreating side of the pin.

Zhao et al. [38] investigated material flow in friction stir welded AA 2014 alloy using a marker insert technique. Results of the flow visualization showed that the material flow is asymmetrical during the friction stir welding (FSW) process and there are also significant differences in the flow patterns observed on advancing and retreating sides. Combining the data from all the markers, three-dimensional (3D) flow visualization similar to the 3D image reconstruction technique was obtained. The 3D plot shows that there is a vertical and circular motion around the longitudinal axis of the weld. The influence of the pin geometry on material flow in FSW was studied. When the column and taper pin are used, there is a 'hole' defect in the vertical mixing plot. When the taper with screw thread pin is used, the vertical material flow is more obvious and there is no distinct 'hole'. Viewing from the advancing side, the pin geometry will affect the position where minimal transport distance against the welding direction occurs.

Schmidt et al. [39] suggested that properties of a work-piece joined by friction stir welding (FSW) are directly related to the material flow around the tool. The material flow was investigated by traditional metallography as well as X-ray and computer tomography. By introducing a thin copper strip in the work-piece and welding through it,

thus, the copper acted as a marker material, and detailed information about the flow field was gathered. The two and three-dimensional CT images were used in parallel with micrographs for visualization of the flow field. Two procedures for estimating the average velocities for material flowing through the shear layer were presented. The procedures depend on the configuration of marker material relative to the welding direction, i.e. longitudinal and transverse.

Both experimental and analytical results [22, 23] show that the axial force (and other forces) can be reduced by increasing the spindle speed. The full range over which this apparent relationship can be expected to hold true is not known. A full quantification of the relationships between spindle speed and other process parameters for friction stir welding are needed. These relationships are of fundamental importance to improved weld productivity with the friction stir welding process and are key to the widespread use of robots for FSW.

CHAPTER III

EXPERIMENTAL PROCEDURE

To study this relationship, experiments were performed at the Vanderbilt University Welding Automation Laboratory using a Milwaukee #2K Universal Milling Machine fitted with a Kearney and Trecker Heavy Duty Vertical Head Attachment modified to accommodate high spindle speeds. The weld sample, clamping fixture (or backing plate), tool design, instrumentation, and machine modifications are detailed below.

Sample Description

For this experiment, plates of AA 6061-T651 aluminum, nominally 0.250 inches thick were friction stir welded. The samples were 3 inches wide by 18 inches long. The tool depth was set to 0.145". To ensure precise setting of the tool depth, the tool was positioned along the weld line aft of the sample's leading edge. The sample is clamped via the scheme shown in Figure 11.

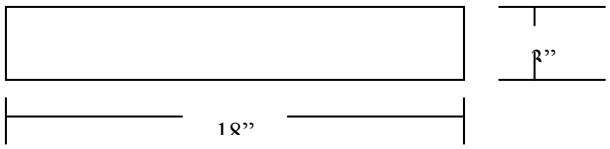

Figure 10: Schematic of AA 6061-T6 plates used in the experiments

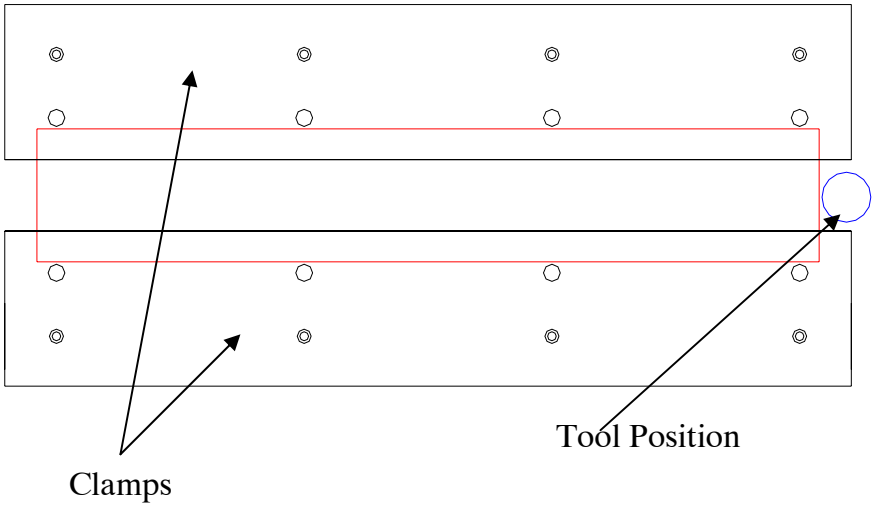

Figure 11: VU FSW sample and clamping scheme.

The clamping system allows for 30 inches of travel maximum and samples with 3” or 5” widths. With the horizontal system, the maximum travel distance was 12 inches and limited to 3” width samples.

Tool Design

For this experiment, the tool was made from H-13 tool steel heat treated to Rockwell c hardness 48-50. The shank diameter was 0.80". The tool shoulder was flat with a 0.50" diameter. The pin was 0.190" diameter with a 24 threads per inch left hand pattern. The pin length was 0.1425". Heat sinks were cut into the far end of the tool shank near the shoulder to facilitate heat dissipation during welding. The tool was rigidly mounted into the tool holder using a collet system. The tool lead angle was set to 2º. Figure 12 shows a detailed schematic of the tool.

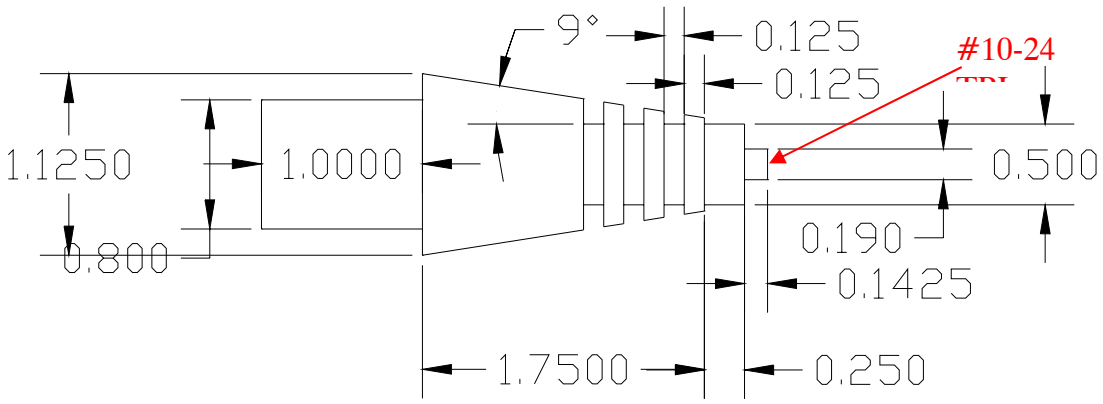

Figure 12: VU FSW tool with 0.5" shoulder and left hand 10-24 thread pattern.

Instrumentation

A Kistler rotating quartz 4-component dynamometer was used for measuring forces and torque on the rotating tool. The dynamometer (Figure 13) consists of a four component sensor fitted under high preload between a base plate and a top plate. The four components are measured without displacement. The four component sensor is ground-insulated; therefore ground loop problems are largely eliminated. The

dynamometer is rustproof and sealed against penetration of splash water and cooling agents. For each component a 2-range miniature charge amplifier is integrated in the dynamometer. The output voltages of the charge amplifiers are digitized and transmitted by telemetry to the stator and then acquired by a PC. The stator is rigidly mounted concentrically with the RCD with a 2 mm gap between them. A mount was fabricated and bolted to the face of the vertical head.

The Kistler data acquisition software DynoWare was used for data collection. DynoWare records the three forces and torque during welding and allows the data points to be exported to a tabularized text file. The data is then imported into Excel, where it is run through a linear smoothing filter and is plotted.

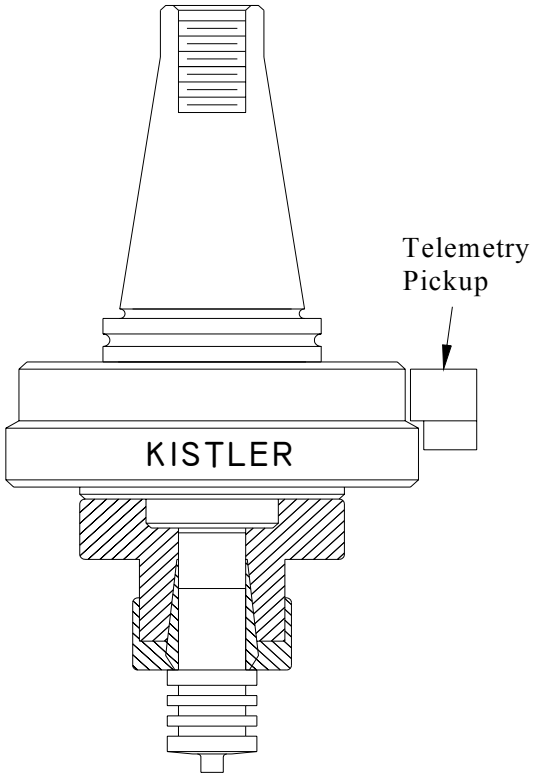

Figure 13: Kistler Rotating Cutting Force Dynamometer

The steady state temperature of the tool pin and shoulder is recorded using a Micron TS7300 infrared camera. An emissivity of 0.95 was used to calibrate the camera to the tool surface. The camera is fixed on a tripod an is angled to allow focusing directly onto the tool pin/material interface.

Machine Modifications

Welding was performed on a Milwaukee #2K Universal Milling Machine fitted with a Kearney and Trecker Heavy Duty Vertical Head Attachment modified to accommodate high spindle speeds. The vertical head clamps the vertical sliding surface of the milling machine. A Baldor VM2514, 20 HP, 3450 RPM, 3Phase 230 VAC motor is mounted to the shoulder of the head and drives the vertical spindle via a Poly-V belt drive system. The motor is controlled by a Cutler Hammer SVX-9000 20HP variable frequency drive.

To meet the operational speed requirements, a 1.79 over drive pulley ratio was used. The large pulley's diameter was 6.0" while the smaller pulley's diameter was 3.35". The maximum speed using the above configuration is 6180 rpm. The overdrive ratio was selected to prevent the possibility of over-speeding the RCD, whose max operational speed is 10,000 rpm. Over-speeding would require the RCD to be recalibrated. The maximum rotational speed at which data was collected for this study was 6000 rpm.

To reduce the inertial load of the vertical spindle, the gear train which coupled the head to the milling machine drive was removed. The gearing system total weight was

approximately 50 lbs. This reduction of loading allows for more torque to be available during welding.

The head was originally grease lubricated, and accommodated a maximum operational speed of 1500 rpm. To suit the higher operational speeds for the experiment, the lubricating grease was cleaned from the spindle's tapered roller bearings. A Bijur Fluid Flex Pressurized Lubricating System was used to lubricate the tapered roller bearings.

The Fluid Flex system dispenses a mixture of compressed air (125 psi maximum) and oil (DTE Lite ISO VG 32). The compressed air is filtered through an air filter/regulator (160 Psi maximum) with a ¼ NPT inlet. The air enters the Fluid Flex system and is reduced to a desired level and passed through a solenoid valve which synchronizes the system with the spindle. Low-pressure air enters the fluid reservoir and forces fluid from the reservoir. Separate lines carry an atomized mixture of air and oil through the distribution lines in the system to the Jet Tip assembly for discharge onto the tapered roller bearings (Timken #455 and #749) of the spindle. Figure 14 shows the VU FSW test bed. To attain the higher travel speeds necessary for this experiment, a Baldor HP variable frequency motor and drive system is used to drive the table traverse.

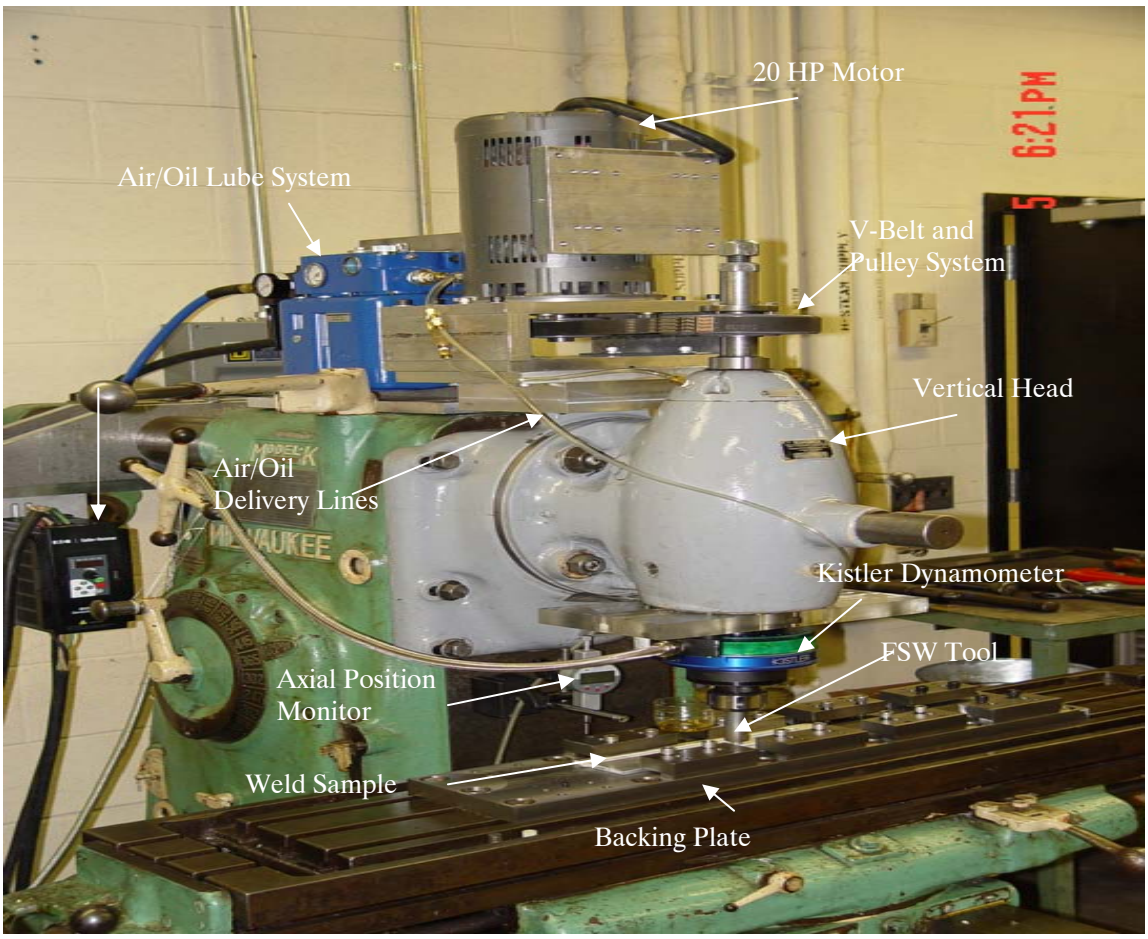

Figure 14: VU FSW test bed.

Table 2 shows the weld parameters used in this experiment. The parameter sets for which welding was not conducted are those where the rotational speed is too high (105 rev/in.) for the travel speed and creates a weld with a deformed surface as shown in Figure 15. The overheat phenomena often occurred at the preceding parameter set. At the low weld pitch regimes (35 rev/in and lower) welds are not run due to potential tool failure.

The experimental procedure is as follows:

1. Clamp sample, program the spindle speed.
2. Set the travel speed.
3. Set the tool depth.
4. Start the lubrication system.
5. Start the machine spindle.
6. Plunge the tool into the material.
7. Start the data acquisition.
8. Engage the table travel.
9. Travel 18".
10. Stop the spindle, travel motor, and lubricating system.

Using the procedure above, welds were made for the parameter set below.

Table 2: VU FSW Experimental Parameter matrix.

Travel Speed (ipm)

Rotational Speed	30	50	70	90	110	130
	w_p (rev / in.)	w_p (rev / in.)	w_p (rev / in.)	w_p (rev / in.)	w_p (rev / in.)	w_p (rev / in.)
1500	50					
2250	75	45				
3000	100	60	43			
3750		75	54	42	34	
4500		90	64	50	41	35
5250		105	75	58	48	40
6000			86	67	55	46

The parameter sets for which welding was not conducted have two possible

criteria. It was observed that for weld pitches less than 35 rev/in (rpi). and greater than 105 rev / in, defects were found to form within the weld [40]. For the low weld pitch range, defects known as worm holes were found to form. In the high weld pitch range, welds with a deformed surface as shown in Figure 15 were observed to form [40]. A discussion of the suggested optimum weld pitch, the ratio of rotational speed to travel speed, will be discussed in Chapter 5.

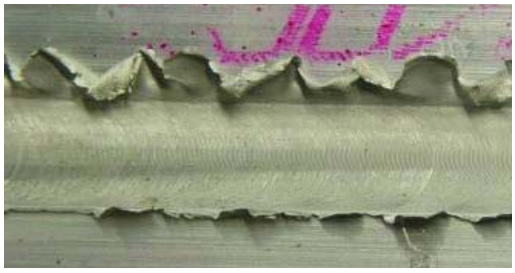

Figure 15: Typical weld deformation for overheat phenomena experienced during experimentation. (Parameter Set: 3750 rpm and 27.7 ipm.)

CHAPTER IV

THEORETICAL MODELING PROCEDURE

In FSW, a cylindrical, shouldered tool with a profiled probe is rotated and slowly plunged into the joint line between two pieces of sheet or plate material, which are butted together. Following tool penetration, the friction stir welding operation depends on continuous refurbishment of the visco-plastic layer surrounding the rotating tool. The term 'third body' has been used to describe the region containing the visco-plastic material produced during frictional welding and friction surfacing [41].

It is apparent that the development of a satisfactory 3-dimensional process model for FSW will depend on how well the ‘third body’ region is handled, in particular how the material properties in this region are determined. The details of the initial two dimensional modeling efforts by Crawford et al. [40] involved only the pin bottom and the sample.

Current FSW process models typically incorporate either a solid or fluid mechanics approach. Experimental results have been shown to correlate with models using either approach. Due to the moderately high temperatures associated with FSW (up to 480 °C) (Sato et al. [19]), and the relatively low melting point of AA 6061-T6 (652°C); it is clear the weld material in the third body region enters what is called a mushy zone [42].

A mushy zone is a region where the material is not a true solid or true liquid, though it has aspects of the behaviors of both. Understanding and accurately modeling

the third body region will lead to an improved 3-D model.

In this dissertation two numerical models are used; a smooth pin tool and a threaded pin tool model. The two models are compared to the experimental data presented by Crawford et al. [40].

FSW Modeling: A Fluid Mechanics Approach

Nandan, Roy, and Debroy et al. [36] showed that the temperature fields, cooling rates, the plastic flow fields, and geometry of the thermo-mechanically affected zone (TMAZ) can be adequately described by solving the equations of conservation of mass, momentum, and energy in three dimensions with appropriate boundary conditions. Understanding and accurately modeling this region will lead to a basic understanding of the FSW process. Based on these conclusions, and the moderate weld region temperature, it is concluded that a fluid mechanics approach to friction stir welding modeling is a valid formulation.

Mechanical Model 1: Visco-Plastic Model

Seidel, Ulysse, and Colegrove et al. [25, 23, 30-31] have successfully implemented the Visco-Plastic fluid flow model. The model relates the large plastic deformation involved in the friction stir welding process to the deviatoric stress tensor and the strain-rate tensor. However, in these papers, the experimental and simulation inputs of tool rotational (ω_o) and travel speed (v_o), were generally limited to a maximum of 500 rpm and 5.11 ipm. In this work, the rotational and travel speed input limitations are approximately a 12 and 26 fold parametric increase, respectively. Though this model has

been shown to correlate very well with experimental force data, it has not yet been shown that the model is valid for the parametric increases stated here.

With the Visco-Plastic fluid flow model, the weld region is assumed to be a rigid-visco-plastic material where the flow stress depends on the effective strain-rate ($\dot{\varepsilon}$) and temperature. The Visco Plastic model is represented by an inverse hyperbolic-sine relation as follows:

$$\sigma_e = \frac{1}{\alpha}\sinh^{-1}\left[\left(\frac{Z}{A}\right)^{\frac{1}{n}}\right] \qquad Z = \dot{\varepsilon}\exp\left(\frac{Q}{RT}\right) \tag{1}$$

where the material constants for AA 6061 T-6 are; $\alpha = 0.045\ (\text{Mpa})^{-1}$, $Q = 145\ \text{kJ mol}^{-1}$, $A = 8.8632\text{E}6\ \text{s}^{-1}$, $n = 3.55$, the universal gas constant $R = 8.314\ \text{mol}^{-1}\text{K}^{-1}$, T is the absolute temperature, and Z is the Zener-Hollomon parameter. The material constants were determined using standard compression tests. The material viscosity is approximated as,

$$\mu = \frac{\sigma_e}{3\dot{\varepsilon}} \tag{4}$$

Equation (4) is implemented below into FLUENT as a user defined function.

Mechanical Model 2: Couette Flow Model

North et al. experimentally correlated the material viscosity during friction stir welding with the Couette fluid flow model [41]. The Couette fluid flow model is a mechanistic representation of the material viscosity of material flow between concentric rotating cylinders. The material viscosity is approximated as

$$\mu = \frac{\left(r_1^2 - r_0^2\right)M}{4\pi r_1^2 r_0^2 \left(\omega_1 - \omega_0\right)} \tag{5}$$

where the inner cylinder has radius r_o, angular velocity ω_o while the outer cylinder has r_1, and ω_1 respectively, and M is the torque per unit depth of the cylinder.

To apply this relationship to FSW, material flow stability must first be taken into account. Couette flow will be unstable if it satisfies the Rayleigh criterion for flow instability. The criterion states that Couette flow will be unstable if

$$\frac{d}{dr_0}\left|r_o^2 \omega_o\right| < 0 \tag{6}$$

To apply this relationship to FSW, r_o is the radius of the tool pin, and ω_o equals the tool rotational speed. The outer cylinder radius r_1 is taken to be the radius of the tool pin plus the width of the third body region (δ) to a point in space where the material is solid and does not rotate, therefore $\omega_1 = 0$. M is the experimentally measured steady state welding torque per unit depth of the tool. Regardless of rotational direction, equation (6) simplifies to $\omega_o r_o$, which is always greater than zero for friction stir welding.

The width of the weld region surrounding the tool pin is approximated using the model suggested by Arbegast et al. [43], which defines the weld region as the weld extrusion zone. A detailed analysis description of approximating the width of the weld region using the Arbegast model is presented in Crawford et al. [40]. Figure 16 shows a detailed schematic of the Couette fluid flow model.

Figure 17 shows the viscosity calculated using the Couette fluid flow model for the welding parameters in Crawford et al. [40].

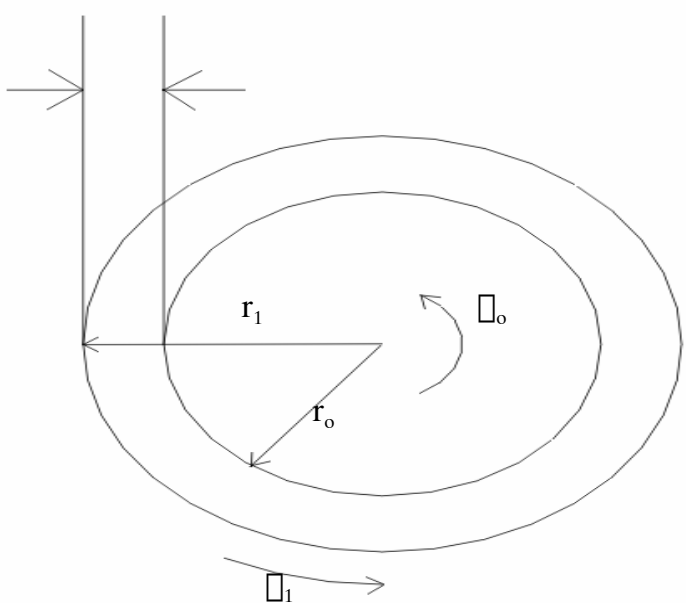

Figure 16: Schematic of the Couette flow model.

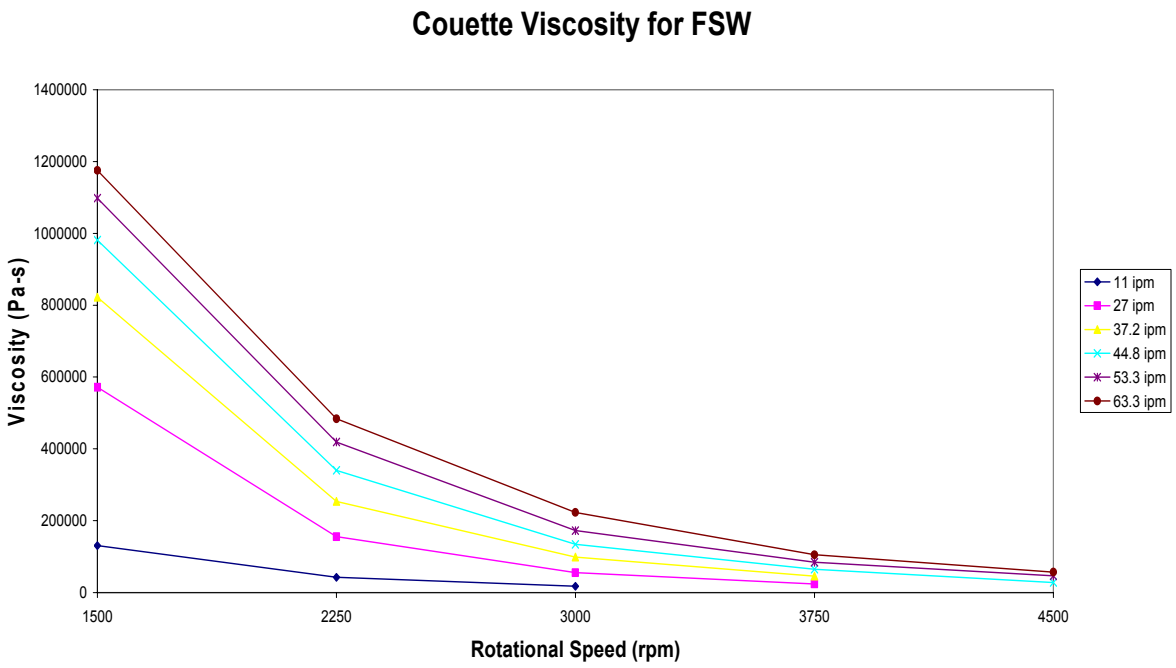

Figure 17: Couette Flow Viscosity for FSW.

Temperature Specification

During friction stir welding, the increase in temperature is caused by heat generated from the contact between the welding tool and the weld material. The rotational speed is assumed to be the primary contributor to heat generation during friction welding, and contribution due to forward traverse is considered to be negligible. Schmidt et al. [44] observed this behavior and developed an analytical heat generation model that takes this assumption into account.

For these simulations, a no-slip condition is assumed. This assumption implies that all tool rotational velocity is transmitted to the weld material at the tool/weld material interface. A no-slip interface can be related to the sticking contact condition suggested by Schmidt et al. rather than the frictional interface, or sliding condition, where the tool surface and weld material are sliding against each other [44]. The sticking model is a function of the contact stress whereas the sliding or frictional interface model is a function of the coefficient of friction.

To determine the steady state welding temperature, a Micron TS7300 infrared camera was used to record the steady state temperature of the tool pin and shoulder for the parameter sets shown in Table 2. These values are input into FLUENT as the tool pin temperature during welding (Chapter 8).

Numerical Model 1: Smooth Pin Tool

In the studies be presented in Chapters V and VI, the smooth pin was used for simulation of partial penetration friction stir welding of AA 6061-T6. The sample/plate material is 3” long, 2” wide, and 0.250” thick. The heat transfer to the support table is

ignored. The sample/weld material model consists of 22497 tetrahedron brick elements with 5152 nodes.

The tool was assumed to be H-13 tool steel with constant density, specific heat, and thermal conductivity and rotates clockwise. The tool tilt angle was 2º and the depth was set to .145". The tool shoulder is flat with a 0.50" diameter and is 0.250" tall. To account for heat conduction from the tool/material interface up the tool, aft of the tool shoulder, a 1" diameter and 0.50" tall shank is included.

The tool pin model is 0.1425" long and the diameter is 0.190". The tool consists of 14300 tetrahedron brick elements with 3185 nodes. The tool pin bottom, sides, shoulder, and shank are assigned a constant angular velocity equal to the tool rotational speed. Figure 18 shows the finite element mesh of the welding tool utilizing the smooth pin.

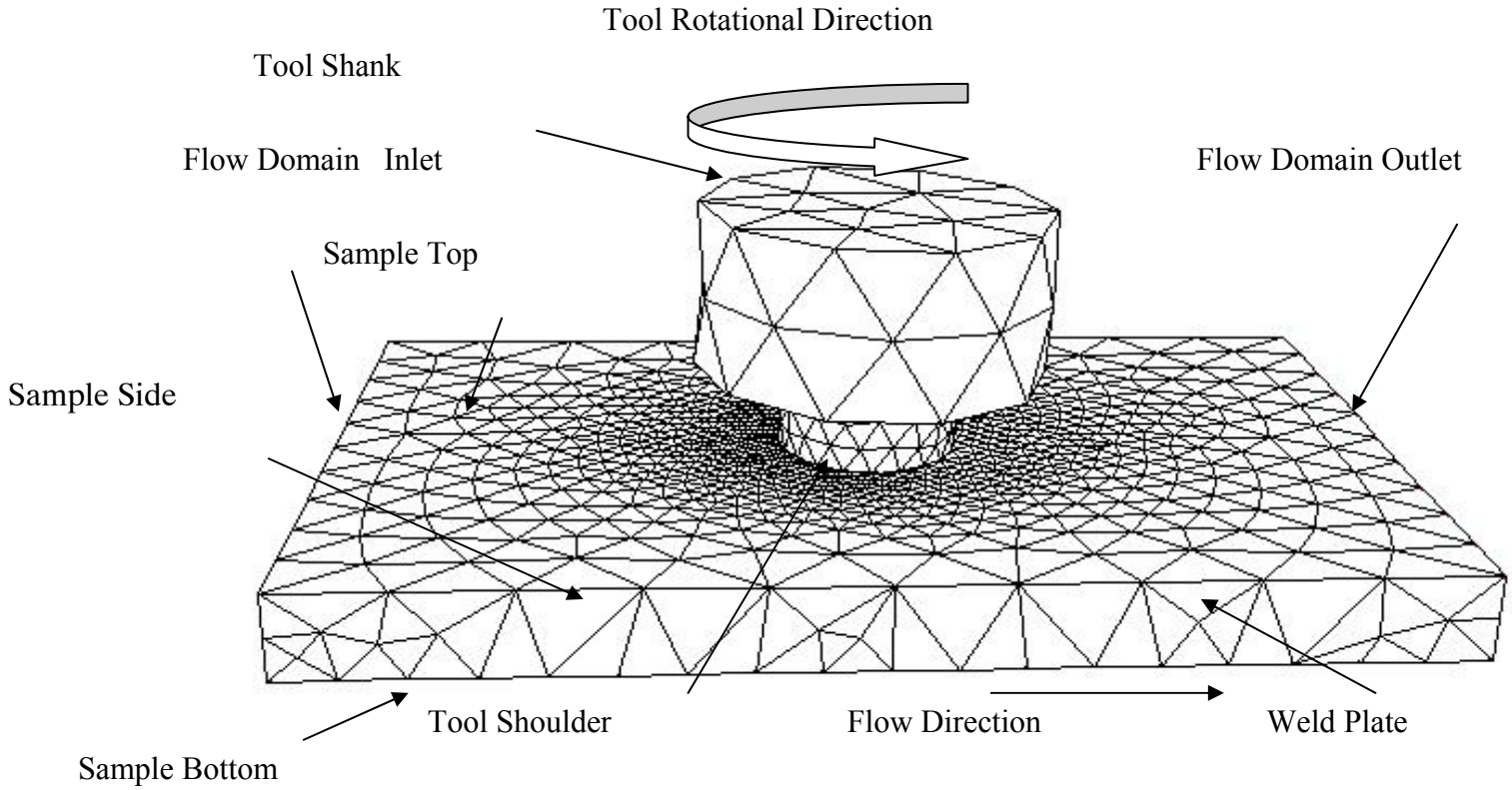

Figure 18: FE mesh of the welding model with a smooth tool pin

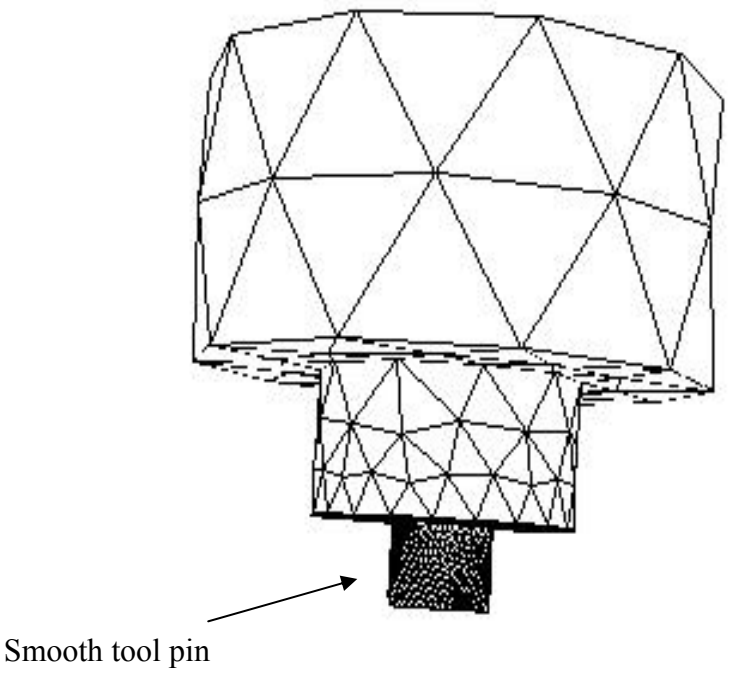

Figure 19: FE mesh of the welding tool model.

For convenience, the global reference frame is assigned coincidentally with the tip of the rotating tool. In other words, the tool rotates and the plate moves toward the tool. Therefore at the flow domain inlet, the material incoming velocity is assigned the weld travel speed and an initial temperature of 27ºC. The sample top, sides, and bottom walls of the plate are also assigned the weld travel speed and an initial temperature of 27ºC as well. The weld material exits through the flow domain outlet. The weld material, top, side, and bottom walls of the plate are assigned temperature dependent density, specific heat and thermal conductivity for AA 6061-T6 and are detailed by Mills et al. [42].

Numerical Model 2: Threaded Pin Tool

The results in Chapters 6 and 8 use the threaded tool pin model. The tool is assigned the constant density, specific heat, and thermal conductivity properties of H-13 tool steel. The tool rotates clockwise, is tilted at 2º, and has a plunge depth of .145". The tool shoulder is flat with a 0.50" diameter. The tool model consists of 37051 tetrahedron brick elements with 8324 nodes. Figure 20 shows the 3-D tool geometry and mesh. Because the pin and shoulder are the interfaces between the tool and the weld material, visual inspection of these surfaces shows that the mesh becomes significantly more dense as you move down the tool. The meshed welding tool can be seen in Figure 20.

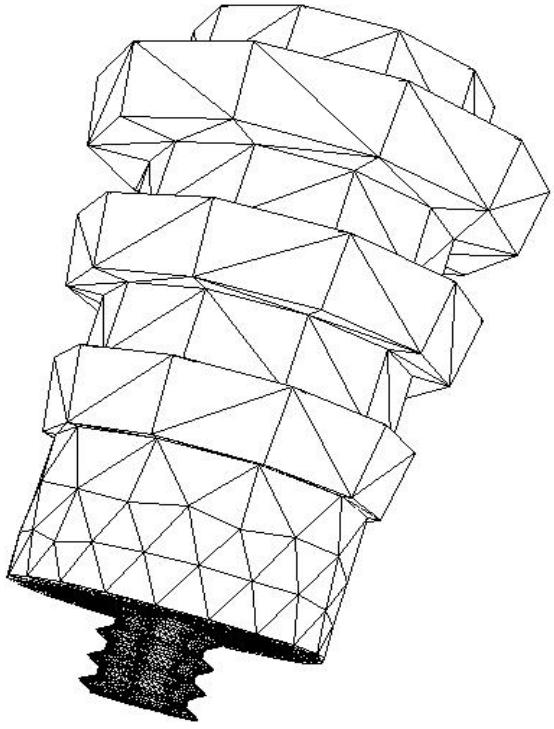

Figure 20: FE mesh of the welding tool model.

The pin is .1425 in. long with a UNC 10-24 left hand thread pattern. A Close up view of the threaded tool pin can be seen in Figure 21.

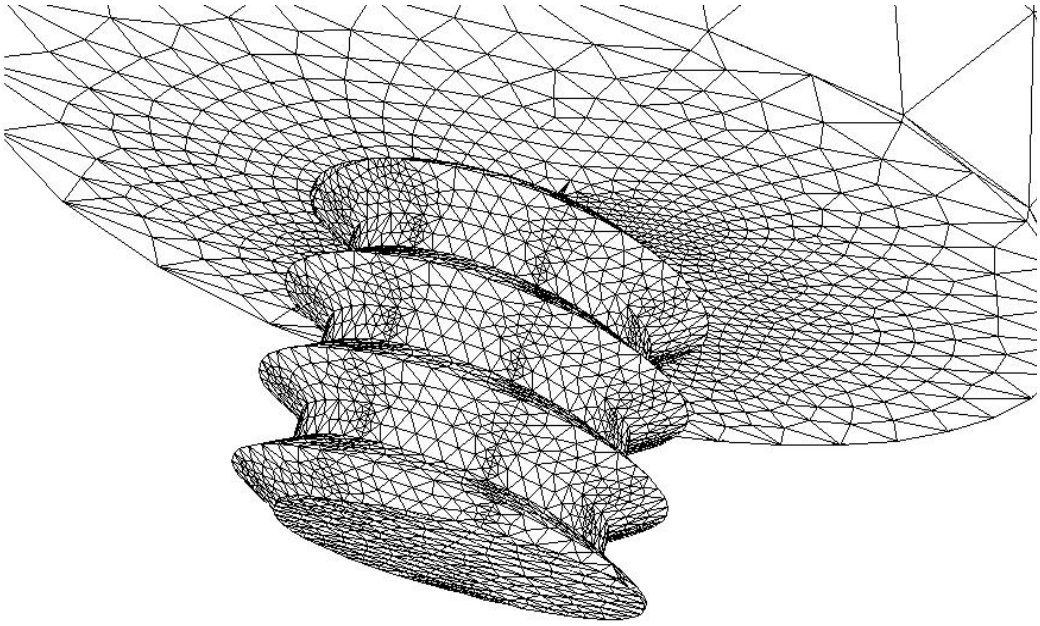

Figure 21: FE mesh of the threaded tool pin and shoulder.

In this model, partial penetration friction stir welding of AA 6061-T6 was considered. The weld material is modeled as a 3" long, 1.75" wide, and 0.25" thick flow domain which consists of 92018 tetrahedron brick elements with 20672 nodes. To simulate heat loss to the backing plate, a 3" long, 1.75" wide, and 0.25" thick plate is connected to the bottom of the flow domain. The backing plate model consists of 42200 quadrilateral brick elements with 24024 nodes. Figure 22 shows the FE mesh of the model.

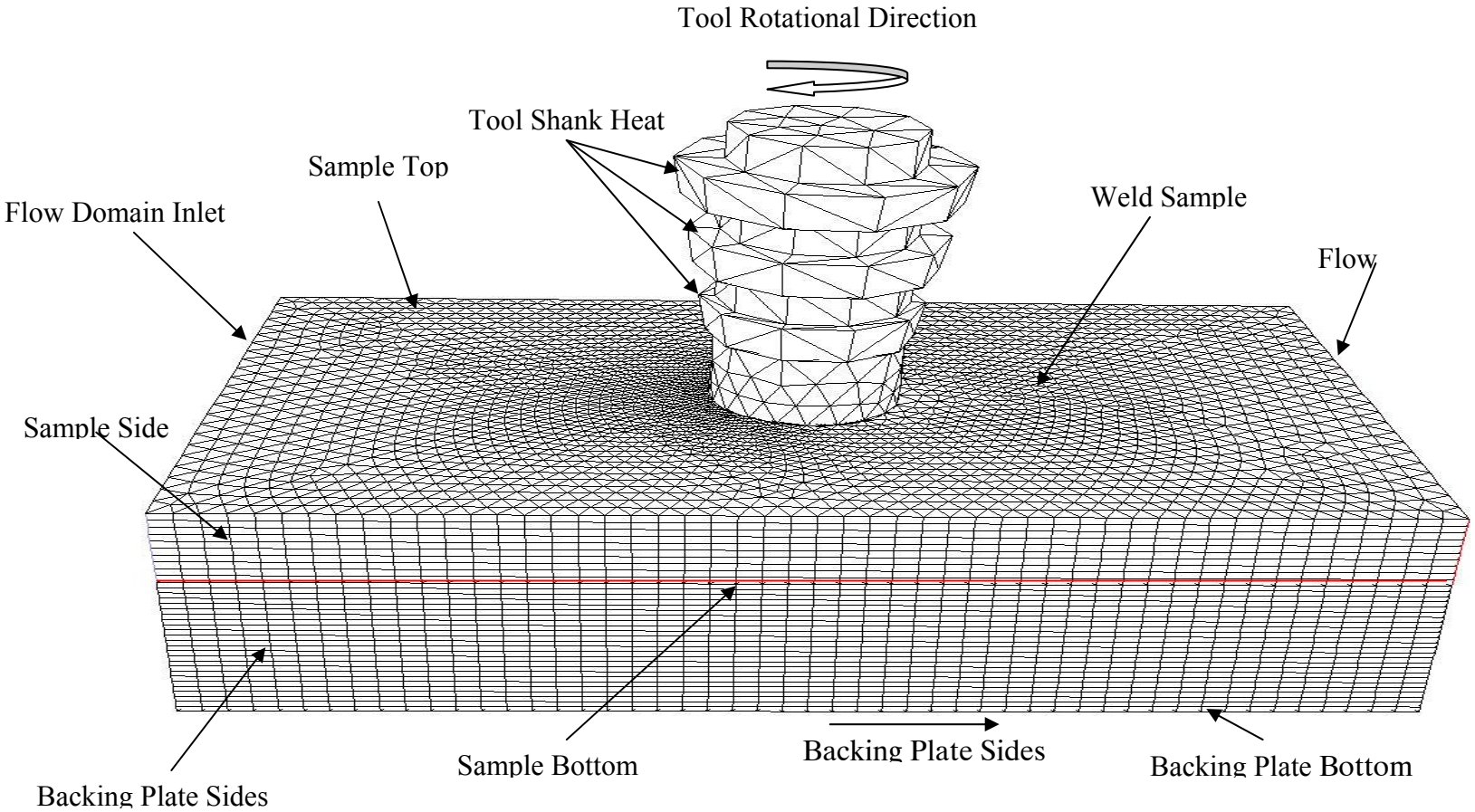

Figure 22: FE mesh of the threaded tool pin and shoulder.

For convenience, the global reference frame is assigned coincidentally with the tip of the rotating tool. In other words, the tool rotates and the plate moves toward the tool. Therefore at the flow domain inlet, the material incoming velocity is assigned the weld travel speed and an initial temperature of 27ºC. The sample top, sides, and bottom walls bound the flow domain and are assigned the temperature dependent properties of AA6061-T6. The sample top, sides, and bottom walls assigned the weld travel speed and zero heat flux. The weld material exits through the flow domain outlet

The tool pin bottom, sides, shoulder, and shank are assigned a constant angular velocity equal to the tool rotational speed.

Governing Equations

The solver controls for the simulations were set to 3-D, segregated, laminar, implicit, and steady incompressible flow. FLUENT uses this configuration to solve the conservation of mass, momentum (Navier-Stokes equations), and energy equations. Gravitational and body forces are neglected as well as changes in potential energy. Heat transfer is assumed to obey Fourier's law of heat conduction.

Material Properties

The material properties used as input variables for FLUENT are detailed below. Table 3 lists the constant properties for H-13 tool steel while Tables 4 and 5 list the temperature dependent properties for the weld material (AA 6061-T6).

Table 3: FSW Tool Properties

Material Property	Density (ρ)	Thermal Conductivity (k)	Specific Heat (Cp)
H-13	7805 (kg/m3)	28 W/(m-K)	416 (J/kg-K)

Table 4: Temperature Dependent Yield Strength of AA 6061-T6

T (K)	σ_y (MPa)
311	241
339	238
366	232
394	223
422	189
450	138
477	92
533	34
589	19
644	12

Table 5: Temperature Dependent Thermal Conductivity and Specific Heat for AA 6061-T6

T (K)	K [W / (m-K)]	Cp [J / (kg-K)]
293	195	870
373	195	950
473	203	980
573	211	1020
673	212	1060
773	225	1150
873	200	1160
915	90	1170
973	91	1170
1073	92	1170

In the following chapters, results are presented that show which mechanical model and numerical model is optimal for mechanistically characterizing the friction stir welding process.

CHAPTER V

MECHANICAL MODEL COMPARISON

This chapter explores and compares the two mechanical models presented in Chapter 4. The smooth pin tool 3-D numerical model is used to simulate the friction stir welding process using the computational fluid dynamics package FLUENT. The two mechanical models; the Couette and the Visco-Plastic fluid flow model for AA-6061-T6 were simulated. The simulation results are compared to experimental data for AA 6061-T6 welded at high rotational (1500-4500 rpm) and travel speeds ranging from 11-63 ipm (4.66-26.7 mm/s) [40]. This chapter examines the forces and torques associated with the FSW process with respect to considerations necessary for robotic implementation. It is shown that force control is an important requirement of robotic FSW.

Axial Force

From Figures 23-25, it can be seen that during these experiments, the machine used for FSW may be called upon to deliver and consistently maintain an axial force of 1-12 kN depending on the tool dimensions and welding parameters.

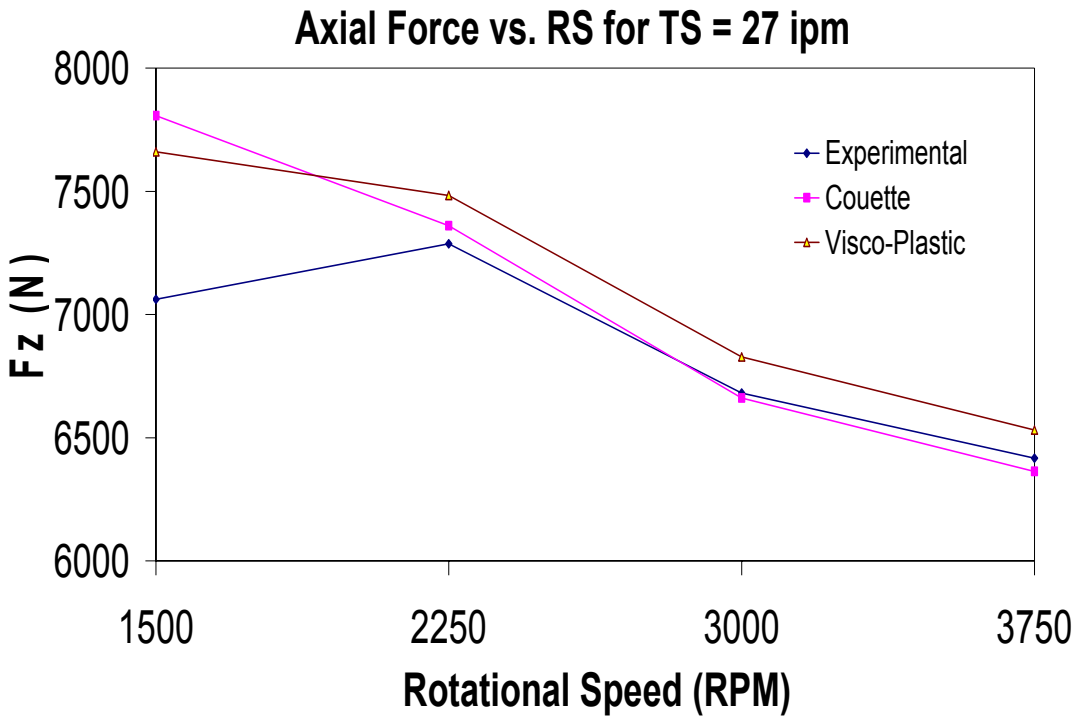

Figure 23: Axial Force for experimental and simulations for TS = 27ipm.

From Figure 23-25, we can see that both mechanical models correlate well with the experimentally measured axial force. Also evident is the trend of the axial force to decrease as the rotational speed is increased for a constant travel speed.

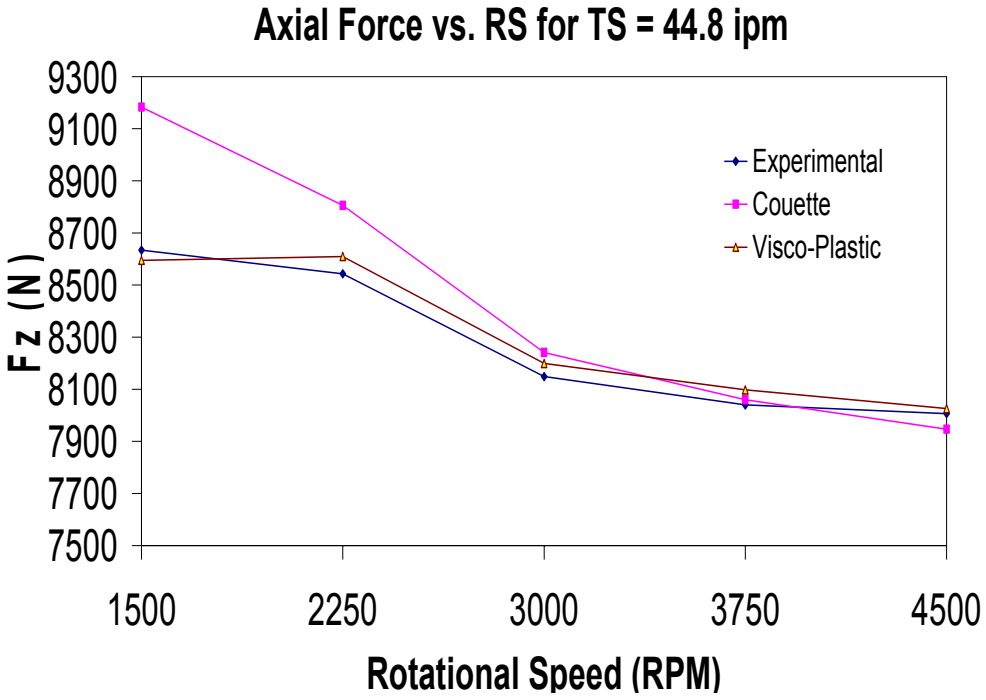

Figure 24: Axial Force for experimental and simulations for TS = 44.8 ipm.

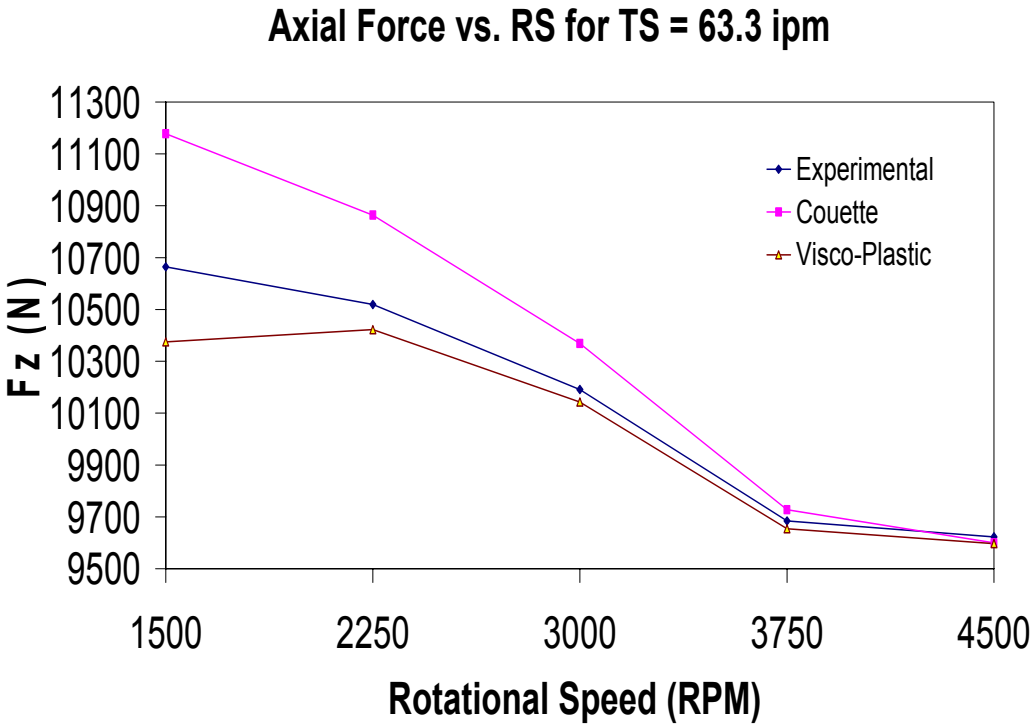

Figure 25: Axial Force for experimental and simulations for TS = 63.3ipm.

By inspection of Figures 23-25, it can be seen that as the weld pitch increases, the simulation data for both models begin to converge with the experimental data.

Figure 26 shows that for a constant rotational speed, as the travel speed is increased the axial force increases. The extent to which the increased rotational speed /decreased axial force and increased travel speed/increased axial force relationship holds true is not yet known. Understanding of this relationship is key to widespread implementation of FSW capable robots.

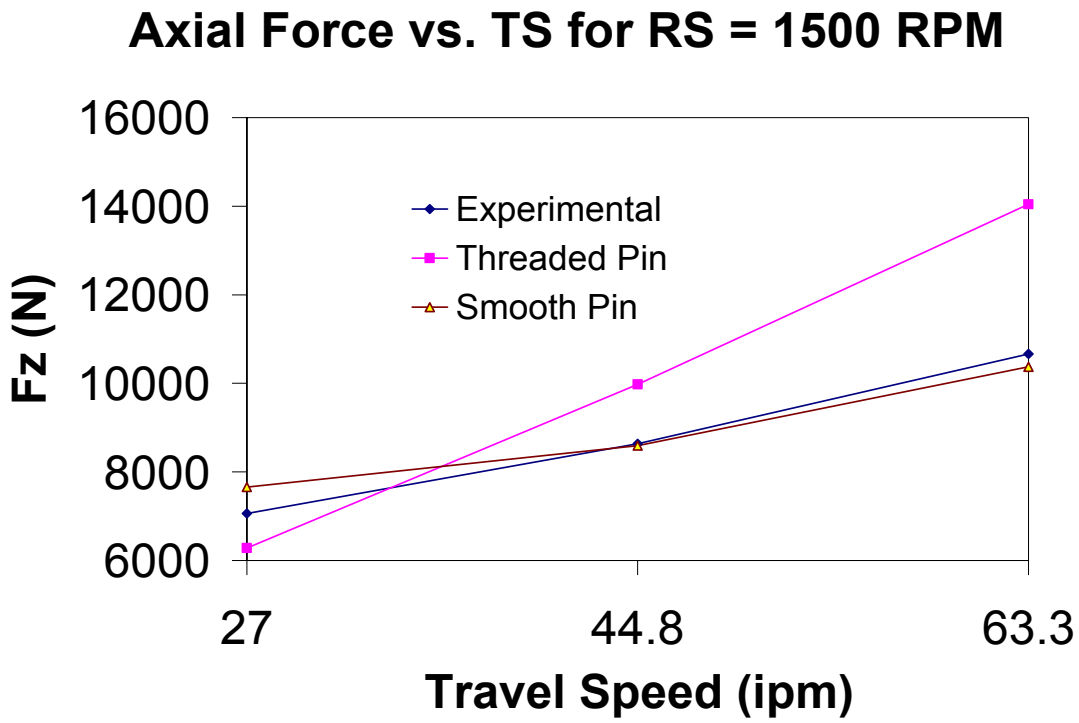

Figure 26: Axial Force for experimental and simulations for RS =1500 RPM.

From Figures 23-25, it is clear the optimum operating parameters for robotic FSW will require high rotational speeds and low travels speeds. However, as the quite

substantial axial force present during FSW is applied to the weld material, which becomes substantially more malleable the higher the rotational speed (or heat input rate) for a given travel speed, the weld material can be easily expelled from under the tool shoulder. There are two possible solutions that would allow a FSW capable robot to exploit the increased rotational speed/decreased force relationship and avoid the pitfalls of surface deformation caused by weld overheating. They are; 1) force feedback control [45] and 2) a non-rotating shoulder FSW tool or floating shoulder tool as suggested by Talia et al. [46]. The floating shoulder tool has its practical applications, however it offers a mechanical solution and is not a "controls based solution", and will not be discussed here.

Force Feedback Control

Force feedback control would allow a FSW robot to adjust for cases where there is insufficient downward force caused by structural compliance of the robotic manipulator and also for high weld pitch parametric regimes where tool excess pressure will cause surface deformation in the form of excess flash. A force control scheme that has been successfully used for this application is shown in Figure 27 [45].

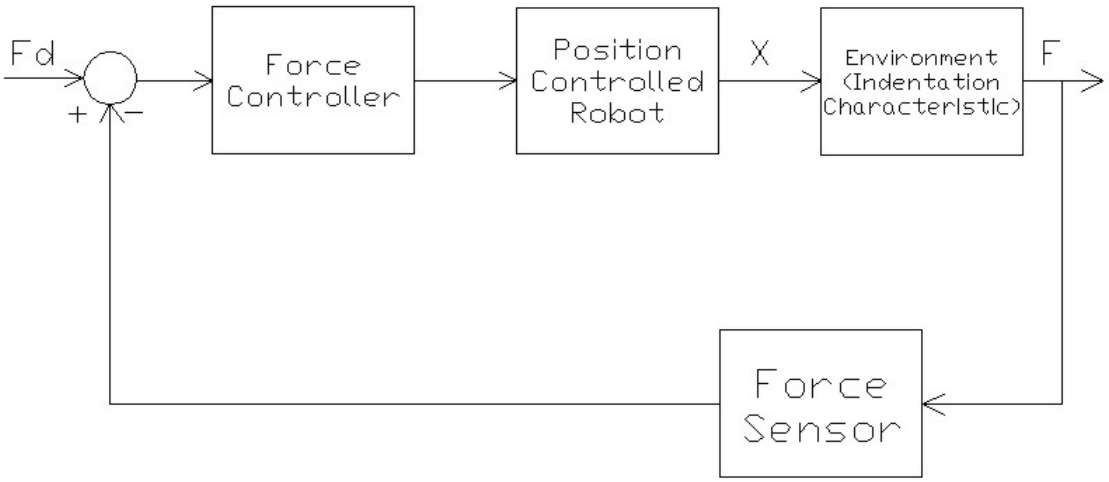

Figure 27: Force feedback control implemented as an outer force control loop around the ordinary position control system of a robot manipulator [45].

.

An "outer" force control loop is closed around the " inner" position control loop of the robot manipulator as suggested by De Schutter and Van Brussel et al. [47]. The programmed *z*-axis position (with respect to the wrist frame) of the robot is modified as required to maintain the desired axial force set by the outer control loop. This approach is attractive because it does not require access to the basic position control loop of the robot. Stability of this scheme will depend largely on the indentation characteristic of the rotating tool as it acts against the plasticized weld zone material [45].

Most force control schemes assume a linear elastic environment. However, in FSW the tool/work piece environment is non-linear, non-elastic, and a function of the welding parameters, e.g. tool rotation speed and travel speed. This has not been found to be a major problem, provided that the force control loop is made inactive during the start and stop portions of the weld. This is significant because the plunge force at weld start, for example, may rise initially to three to five times the weld value [45].

Welding Torque

From Figures 28-30, it can be seen that during these experiments, the machine used for FSW may be called upon to deliver and consistently maintain a torque of about 60 N-m, which depends greatly on the tool dimensions and welding parameters.

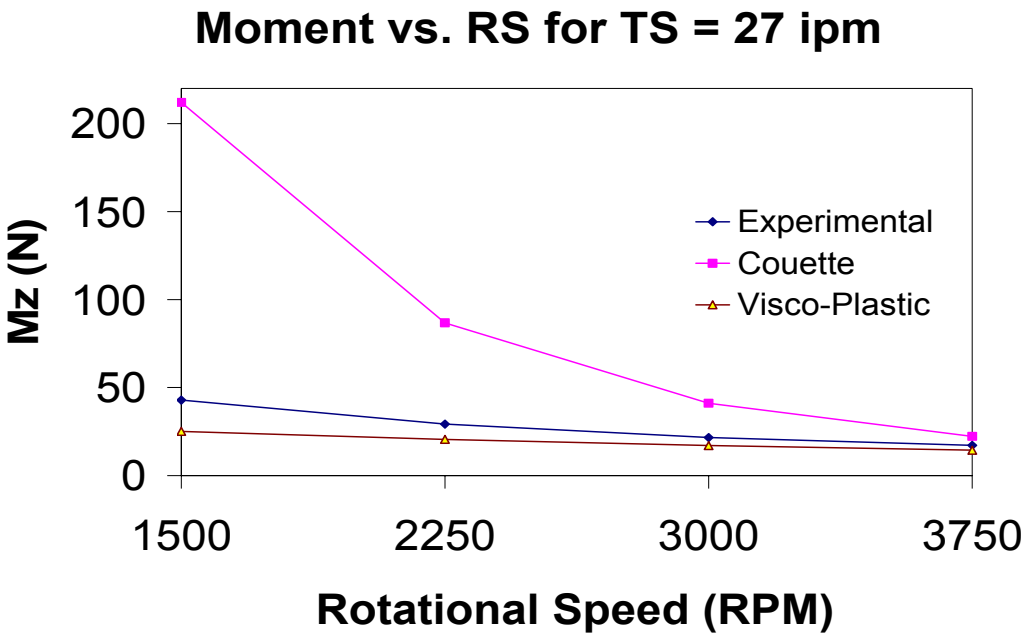

Figure 28: Welding Torque for experimental and simulations for TS =27ipm.

By inspection of Figures 28-30, it can be seen that as the weld pitch increases, the simulation data for both models begin to converge with the experimental data. At low weld pitches however, the Couette flow model torque tends to deviate by a factor of 5 for low weld pitch, but dramatically converges as weld pitch is increased.

One possible reason for this behavior is that as the weld pitch increases, the weld material surrounding the tool experiences an increase in temperature which leads to a

decrease in yield strength of the weld material, thus allowing the weld material to be more easily "stirred". It should be noted that though the Couette flow model is for non-Newtonian fluids, it does not factor temperature into the determination of the material viscosity as the Visco-Plastic flow model does.

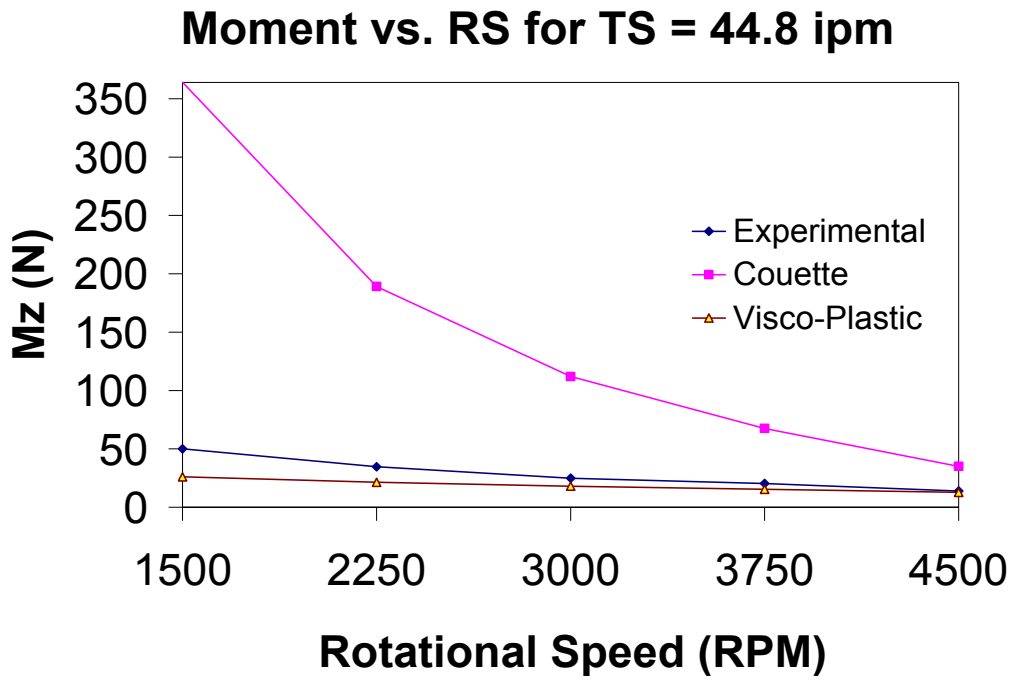

Figure 29: Welding Torque for experimental and simulations for TS =44.8 ipm.

In general the torque follows the same trend as the axial force, where an increase in weld pitch has a corresponding decrease in torque. Likewise, a decrease in weld pitch has a corresponding increase in welding torque.

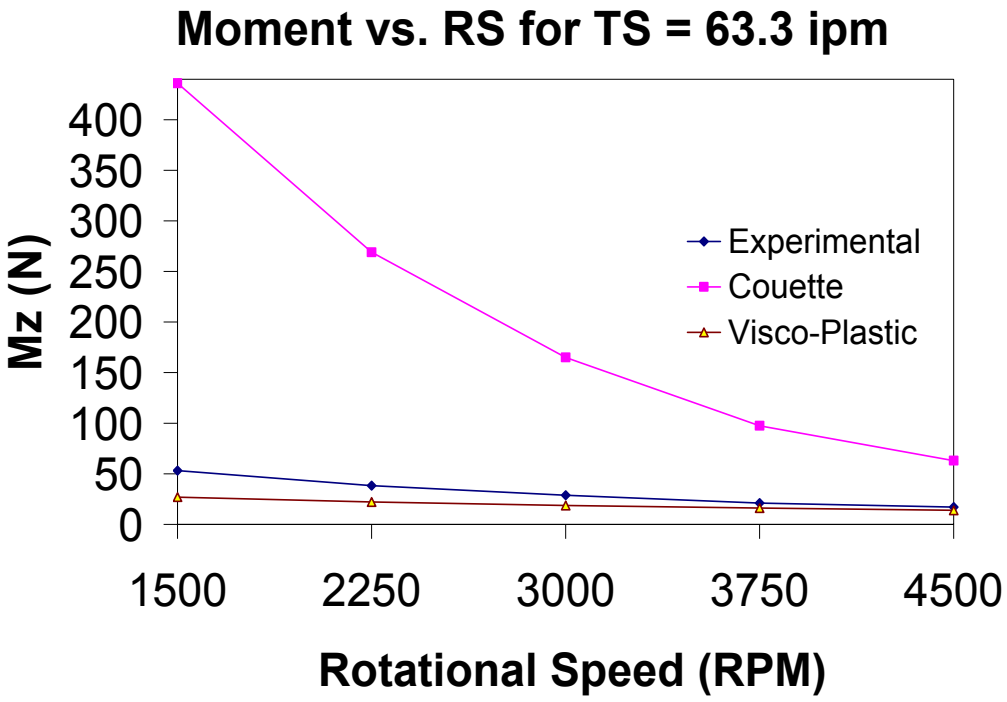

Figure 30: Welding Torque for experimental and simulations for TS =63.3 ipm

Study Conclusions

The experimental and numerical simulation data show that the increased rotational speed/decreased force relationship exists for rotational speeds ranging from 1500 rpm to 4500 rpm, and for travel speeds from 11.4 to 63.3 ipm.

At low weld pitches, the Couette flow model did not correlate as well with the experimental results as the Visco-Plastic flow model. As the weld pitch increased, the experimental results and the Couette Flow model began to converge. This implies that the Couette Flow model is more predictive for very high weld pitches. Overall, the Visco-Plastic flow model was more accurate than the Couette Flow model over the range of weld pitches. The Visco-Plastic Flow model also converged with the experimental

results as the weld pitch was increased.

It was also observed that the present limitation to fully exploiting the increased rotational speed/decreased force relationship is the overheating and subsequent surface deformation of the weld material observed at high weld pitches. A possible solution to this barrier is the implementation of a force feedback control scheme.

Force feedback control would allow an FSW capable robot to adjust for cases where there is insufficient downward force cause by structural compliance of the robotic manipulator and also for high weld pitch parametric regimes where tool excess pressure will cause surface deformation in the form of excess flash.

The continued decrease of axial force and torque with increased rotational speed showed that the upper bound for which the increased weld pitch decreased force and torque relationship holds true was not reached in this experiment [40]. This implies that even higher rotational speeds may achieve a further decrease in axial force and torque during friction stir welding and is the basis for the results in Chapter VII. Based on the conclusions of this Chapter, only the visco-plastic mechanical model will be used in the simulations presented in Chapter VI and VIII.

CHAPTER VI

NUMERICAL MODEL COMPARISON

This chapter compares the two 3-D numerical models presented in chapter 4, and investigates the parametric relationship of the forces, torque, and mechanistic defect development for AA 6061-T6 friction stir welded at rotational and travel speeds ranging from 1500-4500 rpm and 11.4 -63.3 ipm

The first numerical model uses a smooth tool pin while the second model's tool pin is threaded. The numerical models are implemented using the computational fluids dynamics package FLUENT and employ the Visco-Plastic fluid flow model for the viscosity determination. The results are compared to experimental data for AA 6061-T6 friction stir welded at rotational and travel speeds ranging from 1500-4500 rpm and 11.4 -63.3 ipm.

Axial Force

The simulation axial force on the tool is computed by summing the dot product of the pressure and viscous forces on each face with the specified force vector. In addition to the actual pressure, viscous, and total forces, the associated force coefficients are also computed, using specified reference values. The force coefficient is defined as force divided by $1/2\rho vA$, where ρ, v, and A are the density, velocity, and area. To reduce round-off error, a reference pressure is used to normalize the cell pressure for computation of the pressure force. For example, the net pressure force vector is

computed as the vector sum of the individual force vectors for each face:

$$\vec{F}_p = -\sum_{i=1}^{n} pA\hat{n} + p_{ref}\sum_{i=1}^{n} A\hat{n} \tag{7}$$

where n is the number of faces, A is the area of the face, and $\hat{n}$ is the unit normal to the face [48]. This normalization has implications when computing total force coefficients for open domains. For closed domains, the additional term introduced by the reference pressure cancels, but for open domains the pressure normalization introduces a net force equivalent to the product of the projected area of the missing portion of the domain and the specified reference pressure [48]. Because there is no backing plate in the smooth pin model, and it is a open flow domain, a reference pressure equal to the experimental axial force for each parametric set, divided by the area of the tool pin bottom was input as the reference pressure. For the threaded pin model, no reference pressure was used because of the inclusion of the backing plate.

From Figures 31-33, it can be seen that during these experiments, the machine used for FSW may be called upon to deliver and consistently maintain an axial force of 1-12 kN depending on the tool dimensions and welding parameters.

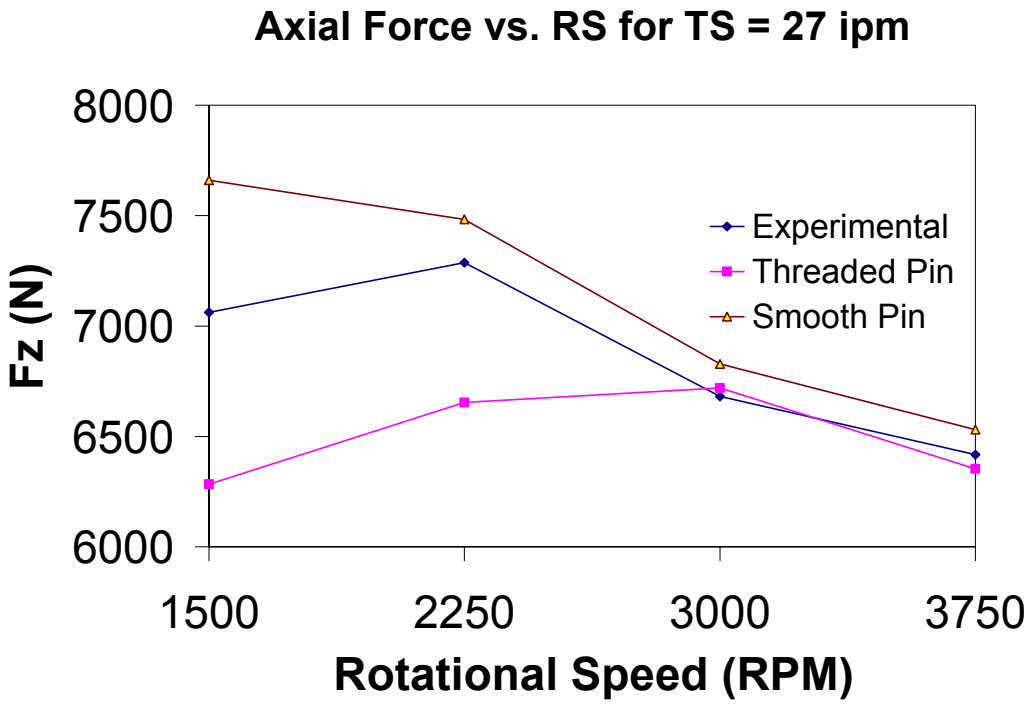

Figure 31: Axial Force for experimental and simulations for TS = 27 ipm.

From Figure 31-33, we can see that both numerical models correlate well with the experimentally measured axial force. Also evident is the trend of the axial force to decrease as the rotational speed is increased for a constant travel speed.

To achieve a viable solution, the solver was iterated until the conservation of momentum and energy equation was had converged to where the changed in the solution was less than 0.0001.

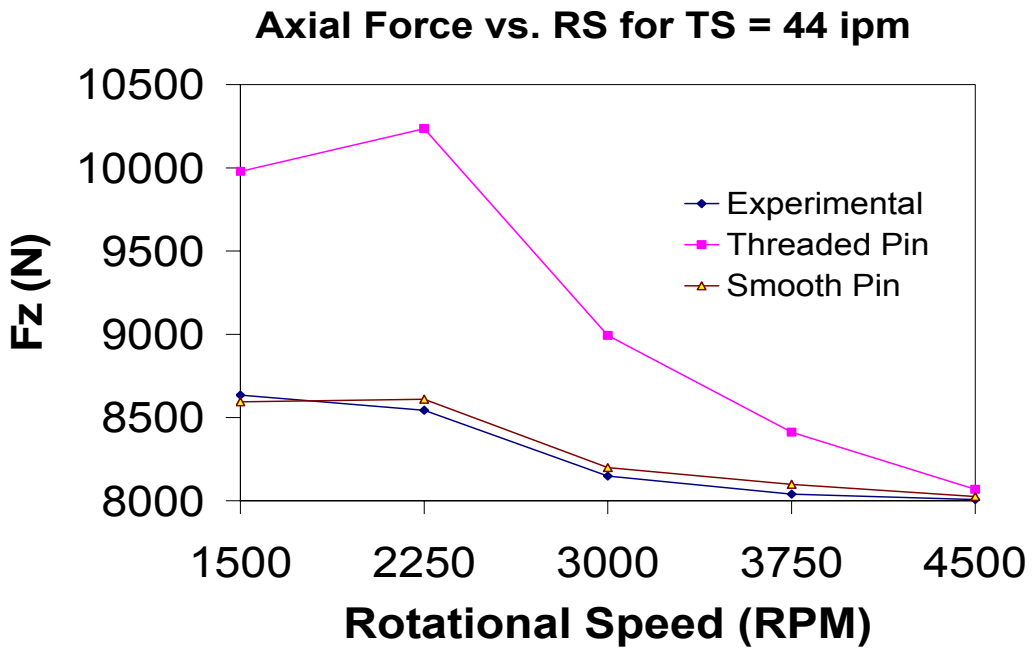

Figure 32: Axial Force for experimental and simulations for TS = 44.8 ipm.

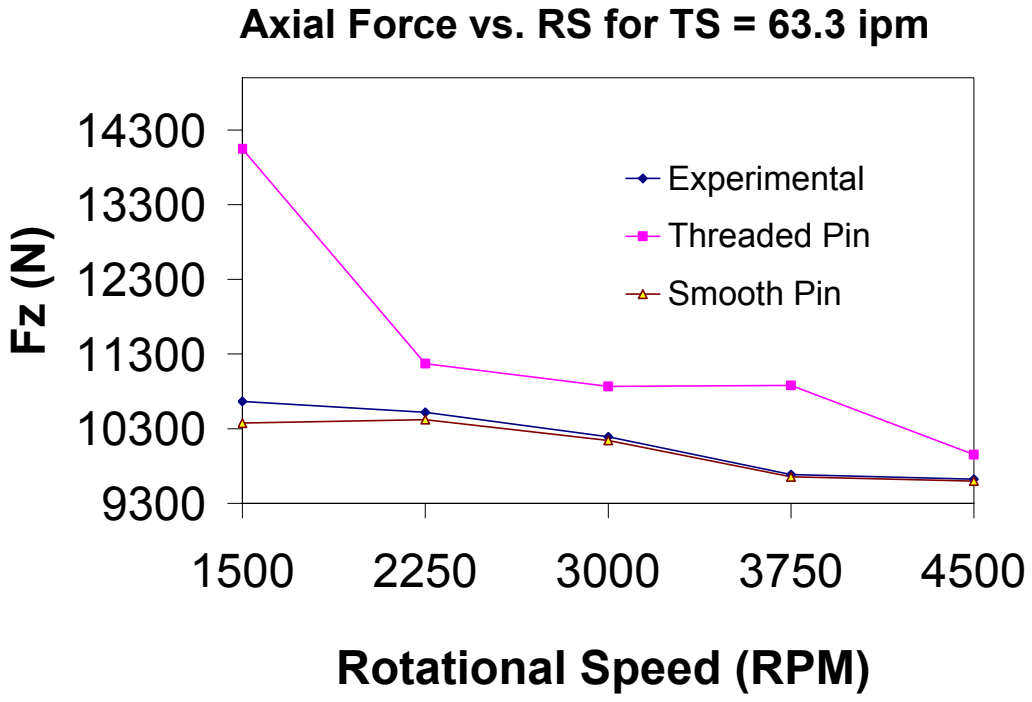

Figure 33: Axial Force for experimental and simulations for TS = 63.3 ipm.

By inspection of Figures 31-33, it can be seen that as the weld pitch increases, the simulation data for both models begin to converge with the experimental data.

Figure 34 shows that for a constant rotational speed, as the travel speed is increased the axial force increases.

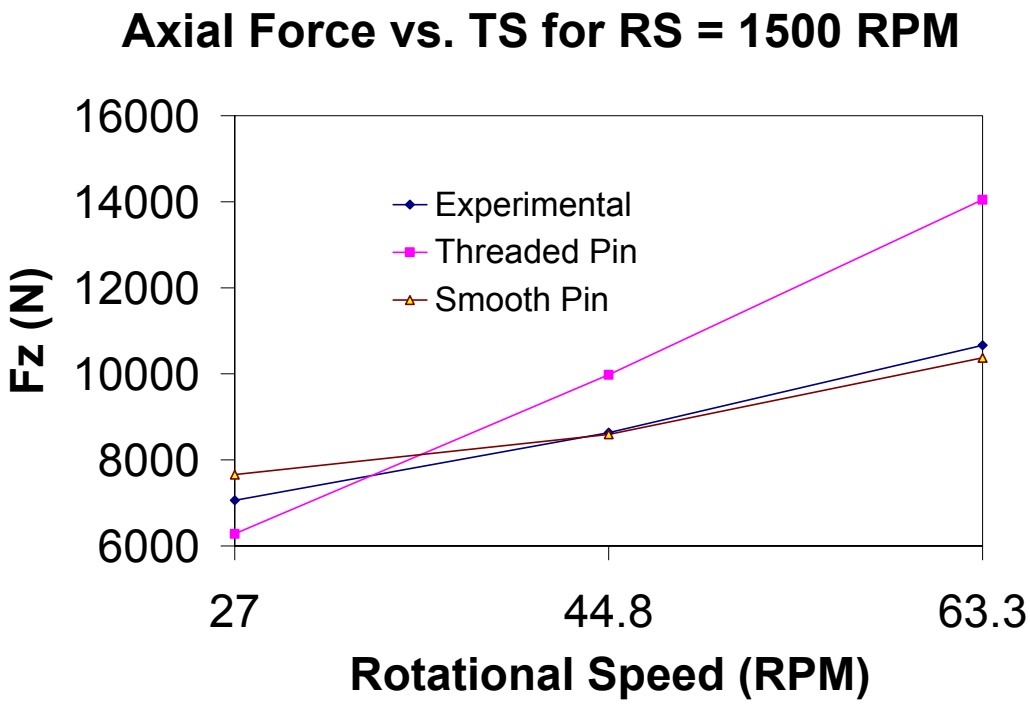

Figure 34: Axial Force vs. TS for the experimental and simulation data for RS = 1500 RPM.

From Figures 31-33, it is clear the optimum operating parameters for FSW will require high rotational speeds and low travels speeds. The smooth pin model may have been more predictive because of the contact condition used. In these simulations a no slip condition was used however some slippage is believed to occur. To fine tune the threaded pin model to correlate with the experimental data, a detailed study in simulation

can be used as a reverse manner to determine the experimental contact condition or appropriate coefficient of friction.

Welding Torque

From Figure 35-37, it can be seen that during these experiments, the machine used for FSW may be called upon to deliver and consistently maintain a torque of about 60 N-m, which depends greatly on the tool dimensions and welding parameters.

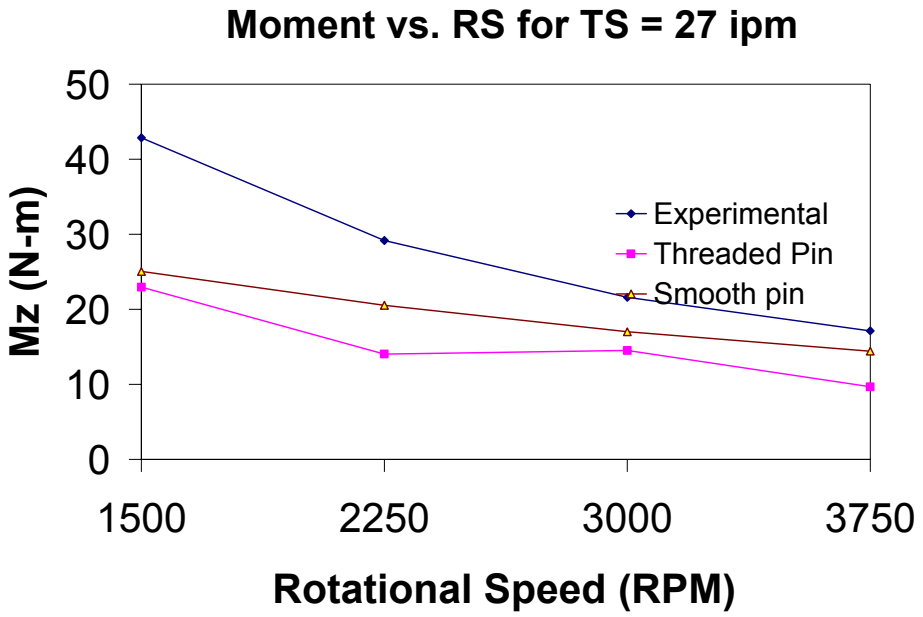

Figure 35: Welding Torque for experimental and simulations for TS = 27 ipm.

By inspection of Figures 35-37, it can be seen that as the weld pitch increases, the simulation data for both models begin to converge with the experimental data. At all weld pitches, the smooth pin model is slightly more precise than the threaded pin.

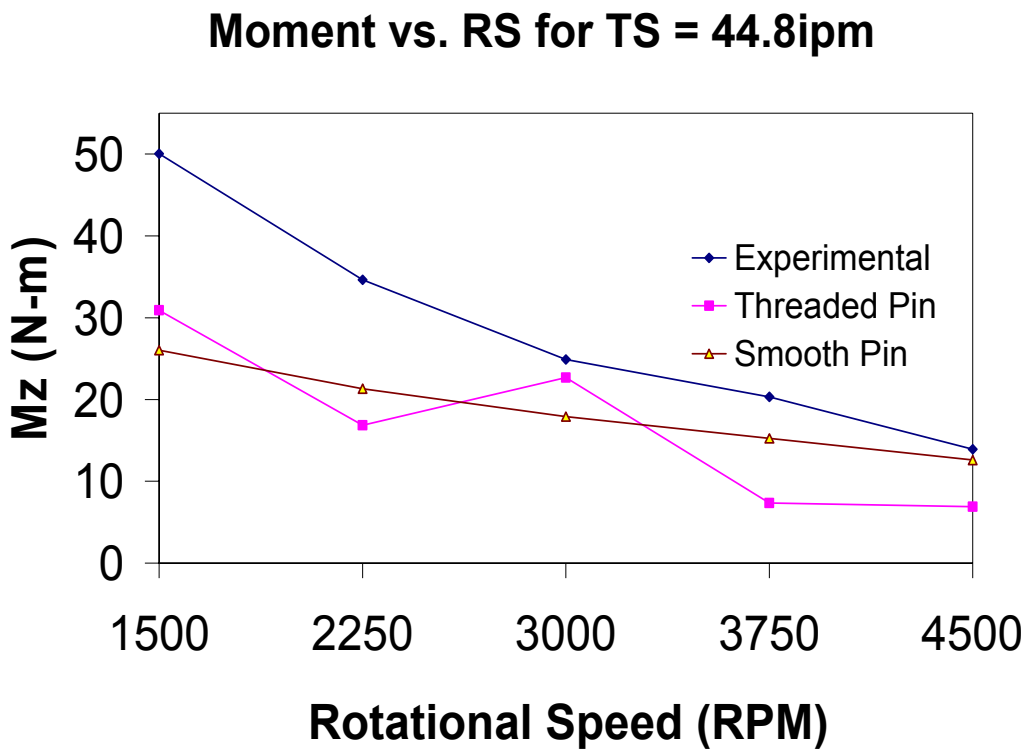

Figure 36: Welding Torque for experimental and simulations for TS = 44.8 ipm.

In general the torque follows the same trend as the axial force, where an increase in weld pitch has a corresponding decrease in torque. Likewise, a decrease in weld pitch has a corresponding increase in welding torque.

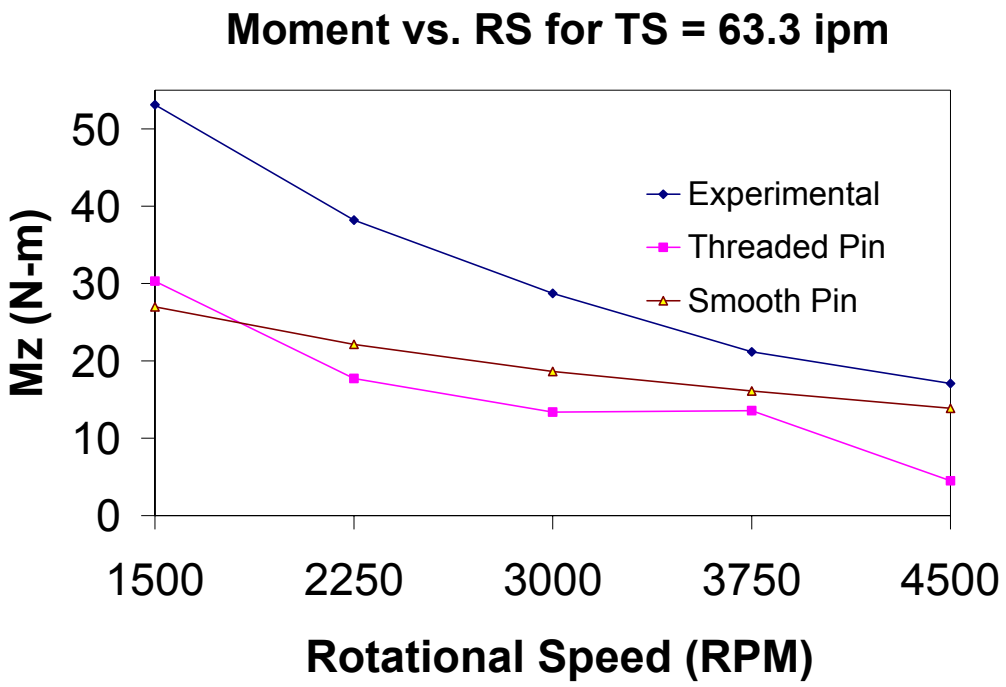

Figure 37: Welding Torque for experimental and simulations for TS = 63.3 ipm.

Weld Defects

Table 6 details the Crawford et al. [40] weld matrix.

Table 6: Crawford et al [40] Experimental parameters and the corresponding weld pitch.

TS (ipm)	**11.4**	**27**	**37.2**	**44.8**	**53.3**	**63.3**
RPM	rev in^{-1}	rev in^{-1}	rev in^{-1}	rev in^{-1}	rev in^{-1}	rev in^{-1}
1500	131	56	40	33	28	24
2250	197	83	60	50	42	36
3000	263	111	81	67	56	47
3750		138	101	84	70	59
4500				100	84	71

The blank parameter boxes are those where the parameter sets for which welding was not conducted. For these sets, the rotational speed is too high for the travel speed and creates a weld with a deformed surface as shown in Figure 38. The deformed surface occurred at the preceding parameter set. For example, for the 3000 rpm and 11.4 ipm parameter set, the weld experienced the extreme surface deformation.

As detailed in Chapter III, welding was not conducted on parametric sets where the rotational speed is too high for the travel speed and creates a weld with a deformed surface as shown in Figure 38. The deformed surface occurred at the preceding parameter set. For example, for the 3000 rpm and 11.4 ipm parameter set, the weld experienced the extreme surface deformation.

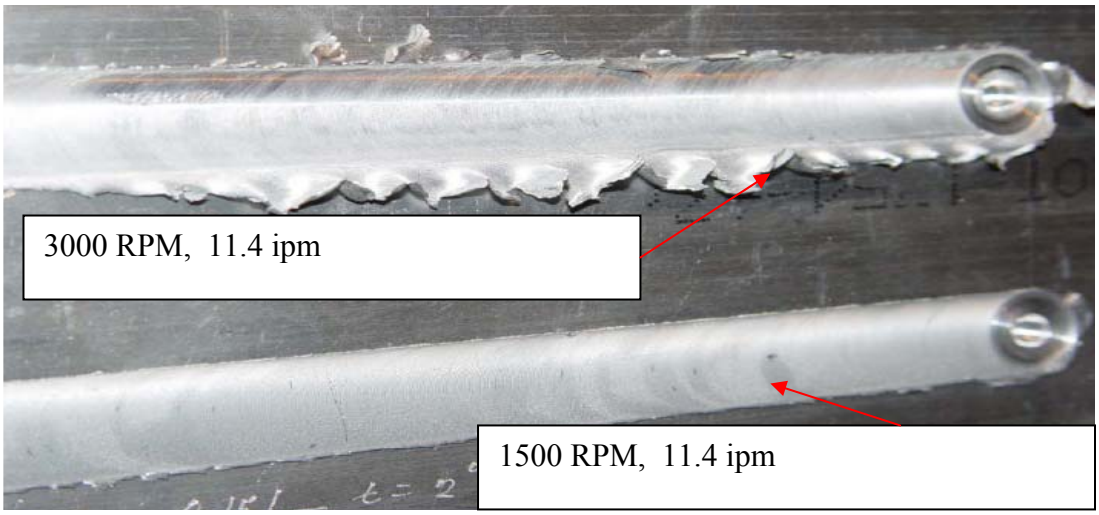

Figure 38: Weld defect due to surface deformation.

Therefore a weld for 3750 rpm and 11.4 ipm was not run because the surface deformation is assumed to only increase.

The experimental sequence was performed by holding the travel speed constant and increasing the rotational speed for each weld until the weld matrix was complete or the surface defect occurred.

Inspection of Figure 39 shows that for shows that for 27 ipm and rotational speed ranging from 1500 - 2250 rpm, there was minimal surface deformation. However for rotational speeds of 3000 to 3750 rpm, there was surface deformation. In Figure 39, it is observed that no worm holes formed.

In the weld matrix shown in Table 6, for the variable rotational speeds and a constant travel speed of 37.2 ipm, the results are similar to those in shown in Figure 39. For variable rotational speeds and a constant travel speed of 44.8 ipm, the surface defect formed at rotational speeds of 3750 and 4500 rpm. For variable rotational speeds and travel speeds of 53.3 and 63.3 ipm, no surface deformation formed.

The surface defect is observable through visual inspection of the weld. A second defect known as a worm hole was found to occur from weld pitch variation as well.

A worm hole is a type of FSW defect where a continuous hole forms inside the weld region along the length of the weld. The worm hole is detected by taking a lateral cross section of the weld, then polishing and etching the surface. Figure 39 shows the welds for various rotational speeds and 27 ipm.

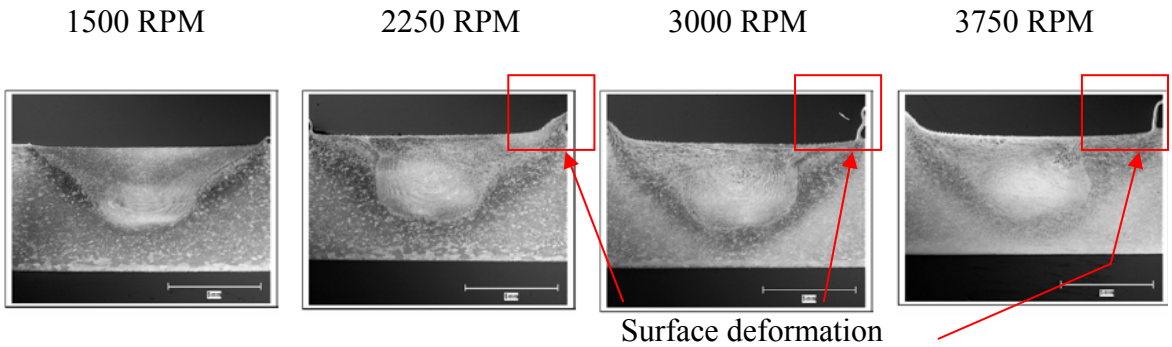

Figure 39: Weld cross sections for variable rotational speed and constant travel speed (TS = 27 ipm).

Figure 40 shows the cross sectional macrographs of the welds at 1500 rpm and various travel speeds for the weld matrix in Table 6.

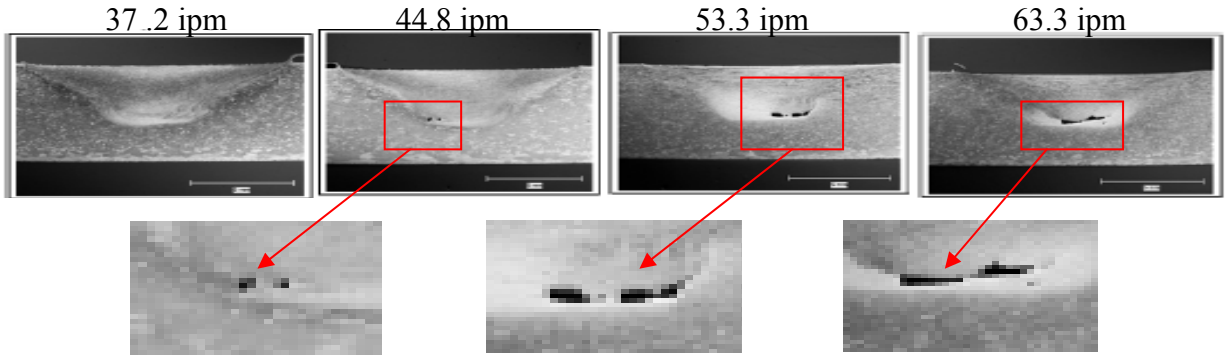

Figure 40: Weld cross sections for variable travel speeds and constant rotation speed (RS = 1500 RPM).

From Figure 40 it can be seen that for a constant rotational speed as the travel speed is increased the wormhole defect begins to form. Also, it is quite noticeable that not only does the wormhole form, but that the size of the defect increases as well. The wormhole typically developed in the bottom of the weld region. This suggests that the wormhole forms due to insufficient material flow to the bottom of the weld. Appendix B

compares the vertical velocity prediction of the smooth pin to the threaded pin model.

Translational Force Correlation with Surface Defect Development

The force data was recorded using a sampling rate of 250 Hz. This frequency was chosen because it offered an optimum number of data points for reaction force observation. Figures 41 and 42 show the raw data plots of the translational force versus time for variable rotational speeds and constant travel speed of 27 ipm and 44.8 ipm respectively.

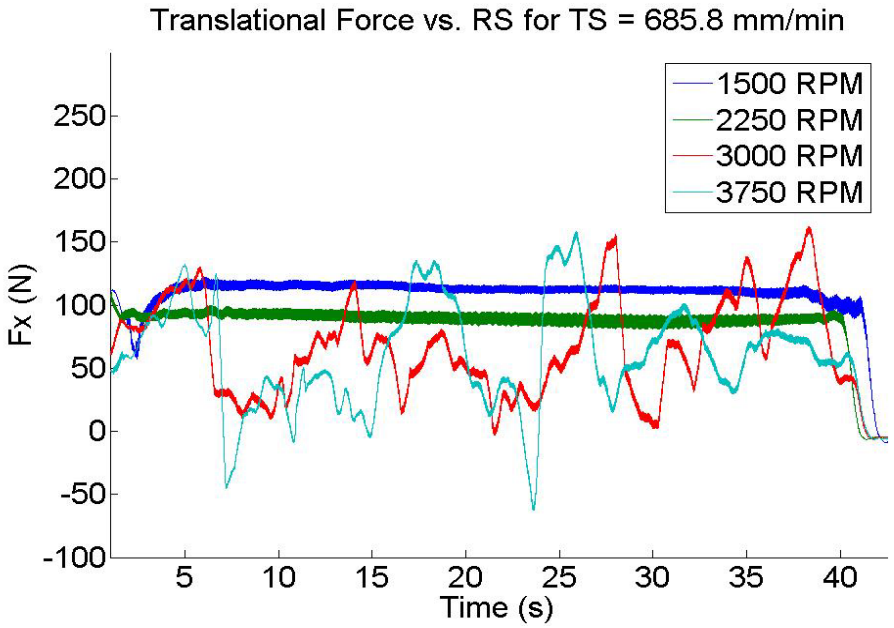

Figure 41: Translational force for variable rotational speeds and constant travel speed (TS = 27 ipm/685.8 mm min^{-1}).

Analyzing Figures 41 and 42, and then observing the type of defect that developed leads to a method for predicting their formation.

It will be helpful now to recall the weld quality observed for travel speeds of 27

ipm which was previously stated above. For the weld data presented in Figure 41, the welds at 1500 rpm and 2250 rpm had negligible deformation. However for the welds at 3000 rpm and 3750 rpm, there was significant surface deformation. Referring to Figure 41, for 3000 rpm and for 3750 rpm, the surface defect develops and it is observed that force curves are oscillatory. While for 1500 and 2250 rpm the force curves are flat and negligible surface deformation occurs.

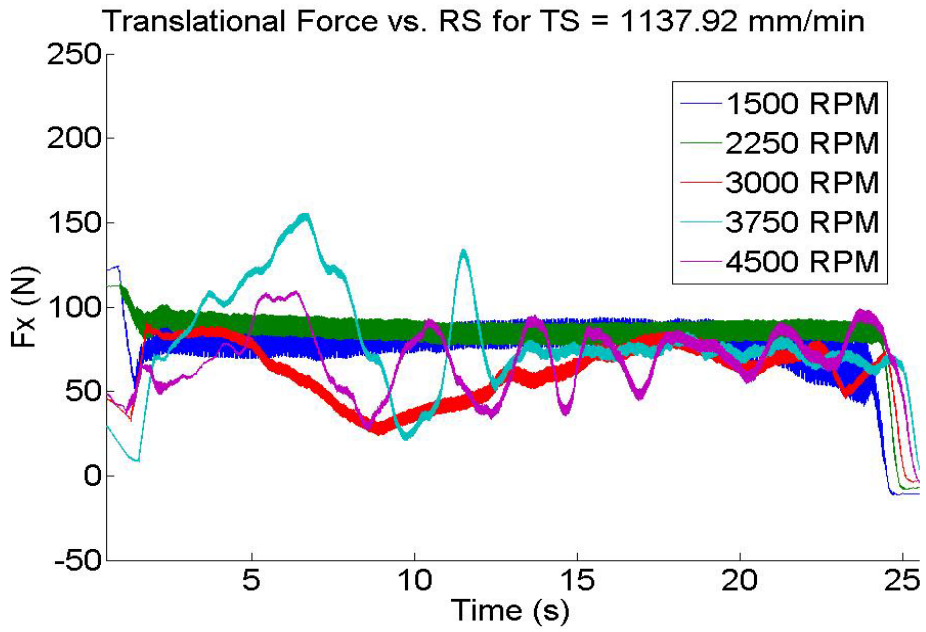

Figure 42: Translational force for variable rotational speeds and constant travel speed (TS = 44.8 ipm/1137.92 mm min^{-1}).

For the weld data presented in Figure 42, the welds at 1500, 2250, and 3000 rpm had negligible deformation while the welds at 3750 and 4500 rpm had significant surface deformation. Referring to Figure 42, for 3750 and 4500 rpm, the surface defect develops and it is observed that force curves are oscillatory. While for 1500, 2250, and 3000 the

force curves are generally flat and negligible surface deformation occurs.

These observations suggest that as the translational force curve fluxuates with more frequency, the surface defect is more likely to develop. Though it is not shown here, the translational force data for all experimental welds generally followed this type of observable behavior.

By analyzing Figures 41 and 42, it is clear that the translational force does not exceed 150 N. The transverse force, F_y, generally displays nearly the same magnitude and oscillatory behavior as the translational force. Compared to the axial force, which was as high as 12kN, the translational and transverse force is generally 70-80 times less than the axial force. The scale of this deviation often leads to the conclusion that the translational and transverse force is negligible. However, as observed here these forces, and their behavior, may prove to be good measures of weld quality.

Welding Temperature

The difference in simulated temperature for the Couette Flow and the Visco-Plastic flow model for both numerical models was less than 1% for the various weld pitches [40]. Therefore only the smooth tool pin numerical model results will be presented in this chapter. Figures 43-44 show that the welding temperature increases as the tool rotational speed is increased.

Figure 43 shows the temperature contour plot for 1500 rpm, and 27 ipm.

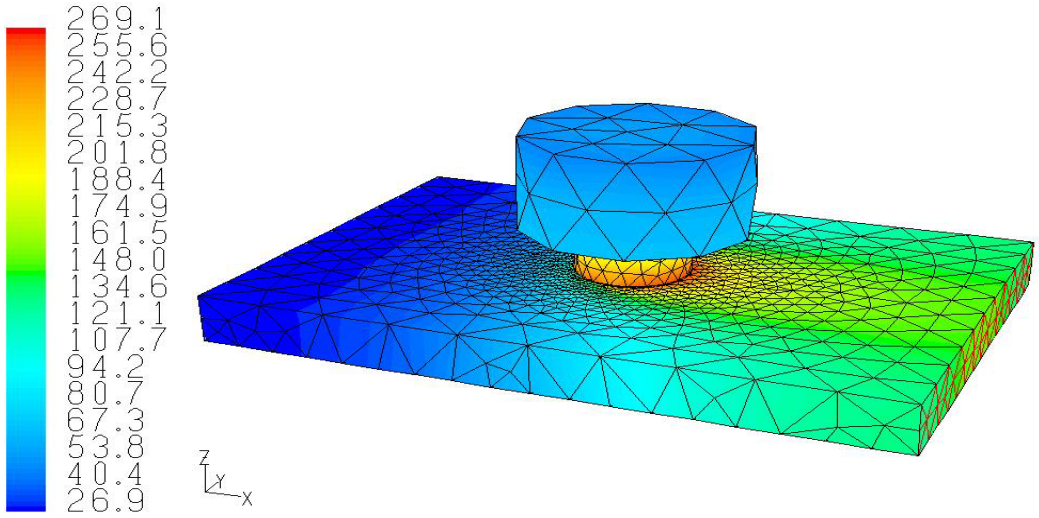

Figure 43: Sample temperature contour (in ºC) for 1500 rpm and 27 ipm.

The surface contour plots generally followed the same patterns of temperature distribution, however there is a significant increase in maximum temperature as shown in Figure 44.

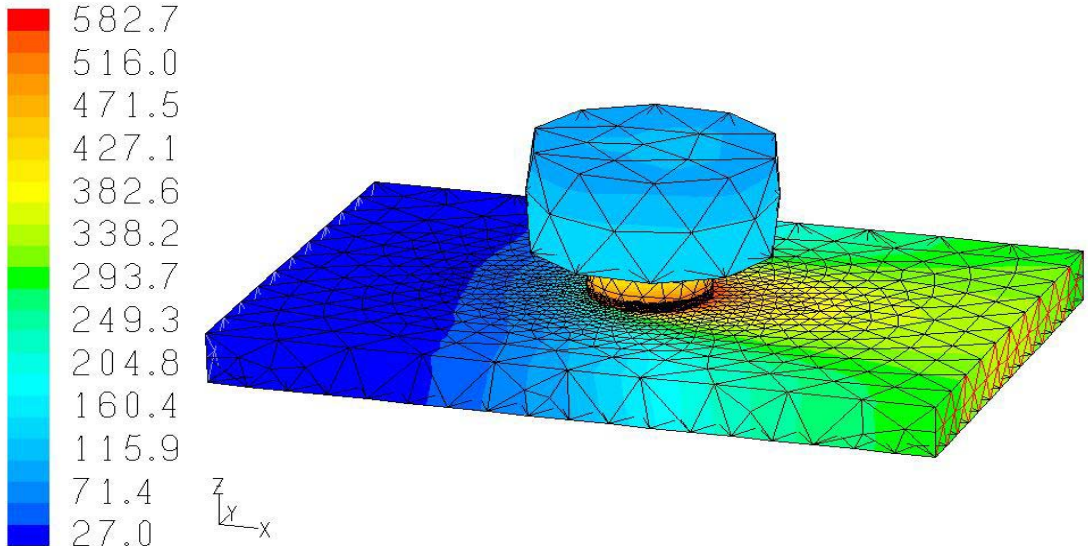

Figure 44: Sample temperature (in ºC) contour for 3750 rpm and 27 ipm.

Observing the temperature distribution at the tool pin and shoulder/weld material interface lend insight into how heat distribution may correlate to weld defect development. Figures 45-48 show the temperature contours at the tool pin material interface.

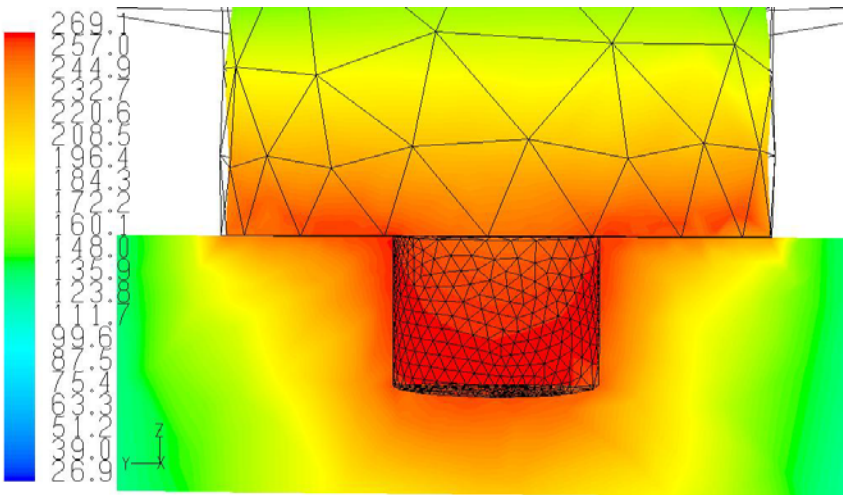

Figure 45: Tool/weld material interface temperature (in ºC) contour for 1500 rpm and 27 ipm.

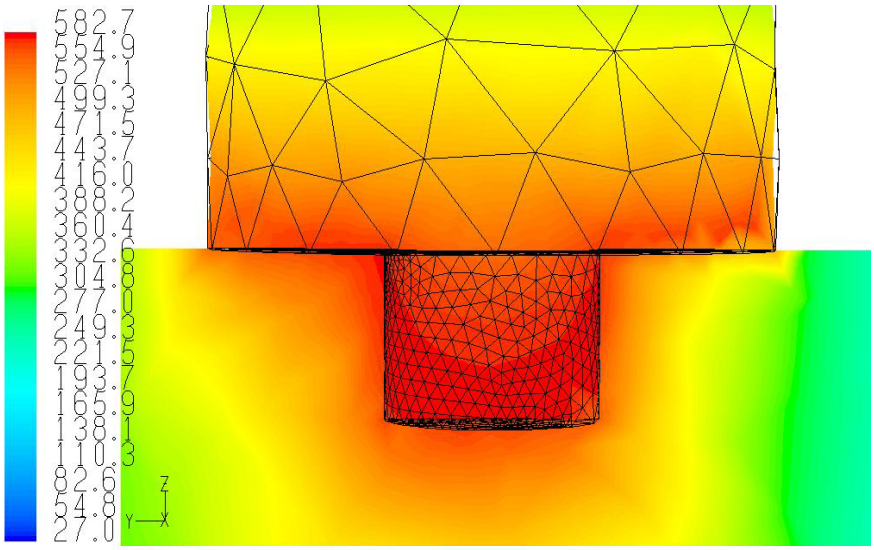

Figure 46 Tool/weld material interface temperature (in ºC) contour for 3750 rpm and 27 ipm.

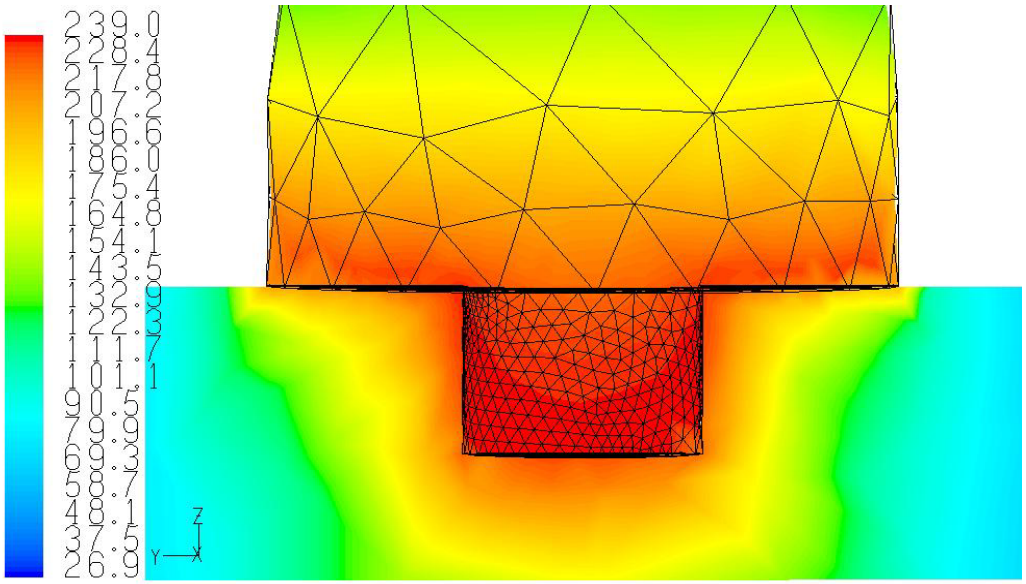

Figure 47: Tool/weld material interface temperature (in ºC) contour for 1500 rpm and 63.3 ipm.

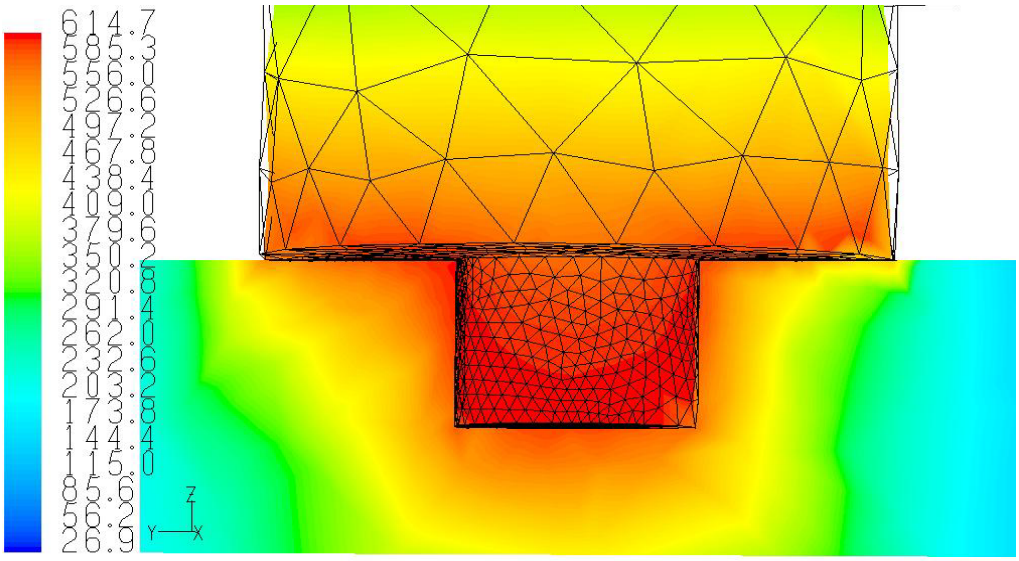

Figure 48: Tool/weld material interface temperature (in ºC) contour for 4500 rpm and 63.3 ipm.

Observing Figure 45 and 46, it can be seen that temperature distribution at the tool/material interface around the tool begins to spread asymmetrically towards the advancing side of the weld. It should be noted that the parametric set shown in Figure 45 had no defect, while the parametric set in Figure 46 experienced surface deformation due to possible weld overheating. This assumption is supported by the fact that the high temperature distribution in Figure 46 extends laterally well beyond the shoulder region.

Observing Figures 47 and 48, it is evident that the high temperature region begins to spread asymmetrically towards the advancing side of the weld by increasing the rotational speed. However, this high temperature region does not extend beyond the shoulder region as in Figure 46, however the maximum temperature was slightly higher. This can possibly be related to the greater weld pitch of Figure 46 to Figure 48, which has a difference in weld pitch by nearly a factor of 2.

A conclusion to the results of these simulations is that as the heat distribution begins to expand relative to the shoulder, flash material begins to develop.

With regards to wormhole defects, they are very likely to develop when using a smooth pin for welding. By profiling the probe, a downward material flow is induced when the tool is rotated opposite the thread pattern. Appendix B presents a detailed discussion of this behavior.

The heating of the weld material is believed to enhance the ability of the weld material to flow downward. So by viewing Figures 45-48, it is evident that Figure 47 has the shallowest high temperature contour of the figures. It should be noted that the parameters used in the simulation for Figure 47, 1500 rpm and 63.3 ipm, produced a wormhole during welding, whereas the other parametric sets did not.

Study Conclusions

The experimental and numerical simulation data show that the increased rotational speed/decreased force relationship exists for rotational speeds ranging from 1500 rpm to 4500 rpm, and for travel speeds from 11.4 to 63.3 ipm.

At all weld pitches, the smooth pin model was generally more predictive than the threaded pin model. However it is important to note that the threaded pin model more accurately reflects the experiments because of the pin profile and the inclusion of the backing plate.

The axial force and torque continued to decrease as rotational speed was increased. This showed that the upper bound for which the increased weld pitch decreased force and torque relationship holds true was not reached in this experiment

[40]. This implies that even higher rotational speeds may achieve a further decrease in axial force and torque during friction stir welding. This synopsis is the basis for the study results presented in Chapter 7.

CHAPTER VII

HIGH SPEED EXPERIMENTAL RESULTS

In this chapter, a comprehensive study of the friction stir welding process will be presented. Building on the results presented in Chapters 5-7, the experimental results for the weld matrix in Table 2 will be discussed. It will now be useful to identify the parameters which significantly affect the forces, torque and temperature during friction stir welding.

The rotational speed is the primary contributor to the heat input rate during FSW. Increasing rotational speed has been shown to decrease the axial force during FSW [40]. The axial force decreases because as the temperature of the weld material rises, the yield strength of the weld material decreases. For example, at 311 K (38 ºC) the yield strength of AA 6061-T6 is 241 MPa, while at 644 K (371 ºC) the yield strength decreases to 12 MPa (See Table 4). This temperature increase leads to a 95 % decrease in yield strength. This fact clearly illustrates that the rotational speed is a primary parameter for affecting the mechanistic characteristics during friction stir welding. The extent to which this relationship can be exploited will be explored in this chapter.

In concert with the rotational speed, the weld travel (or traverse) speed affects the heat generation during FSW in the following manner. By increasing the travel speed, the number of revolutions per distance of tool travel is decreased. Therefore increasing the tool travel speed is believed to have the general effect of decreasing temperature during welding and subsequently increasing the axial force. It is important to note that these

relationships are for a constant tool penetration depth and that there are parametric regimes in the following paragraphs which show where and how these relationships deteriorate.

As stated in Chapter 3, welds were made for the parameters shown in Table 2. The results will be discussed relative to weld pitch variation.

As stated in the introduction, a goal of this research is to establish guidelines for implementing FSW capable robots. A significant limiting factor when implementing FSW capable robots is the axial force requirement necessary when welding. In the experimental results to be presented here, the translational force, transverse force, axial force, and welding torque were measured for the parameter sets listed in Table 2. The raw data plots can be seen in Appendix A.

Axial Force (Fz)

The axial force was measured for the weld parameter sets shown in Table 2. The raw data plots can be seen in Appendix A. The steady state axial force is presented in the following figures as the average axial force during the welding. Each weld parameter set was run a minimum of two times in order to verify the precision of the force data. The steady state axial force was found by averaging the mean axial force of each run of a weld parameter. Figures 49-51 show the steady state axial force for variable rotational speed and travel speed, respectively.

From Figures 49-51, it can be seen that the axial force decreases as the rotational speed increases.

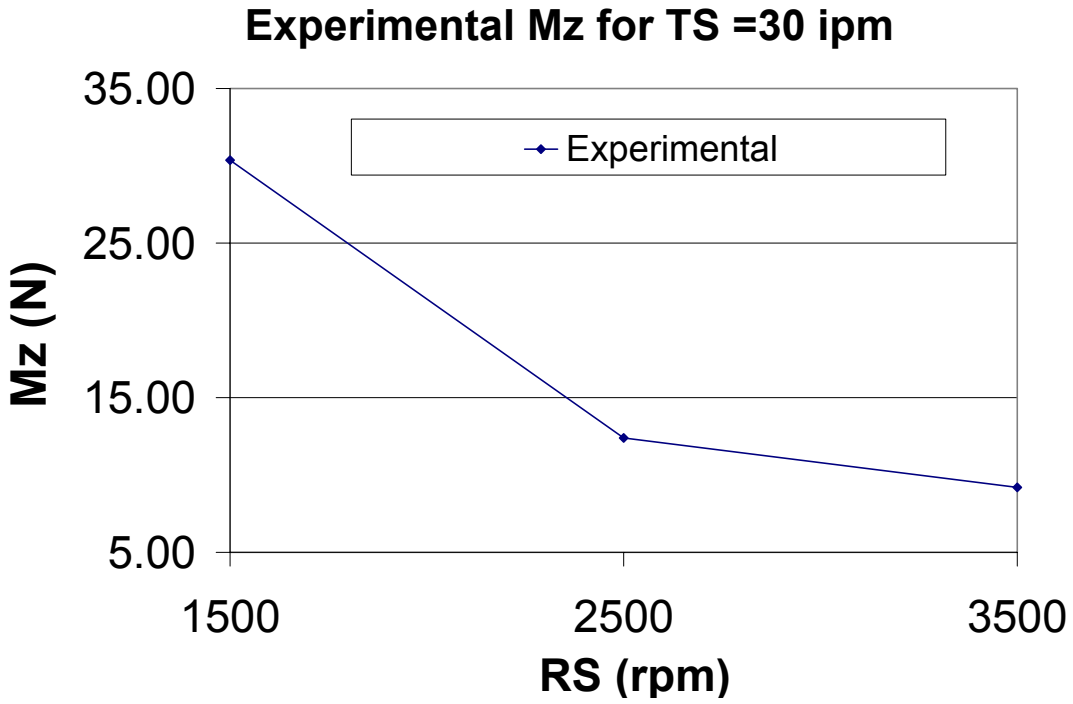

Figure 49: Axial Force vs. Rotational Speed for TS = 30 ipm.

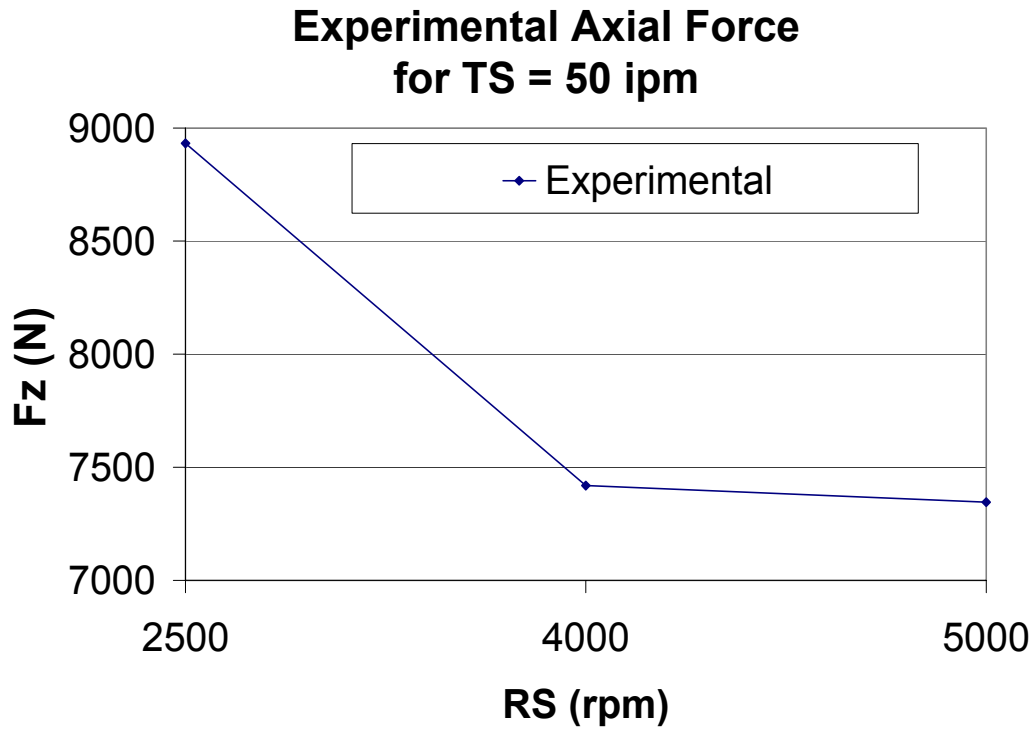

Figure 50: Axial Force vs. Rotational Speed for TS = 50 ipm.

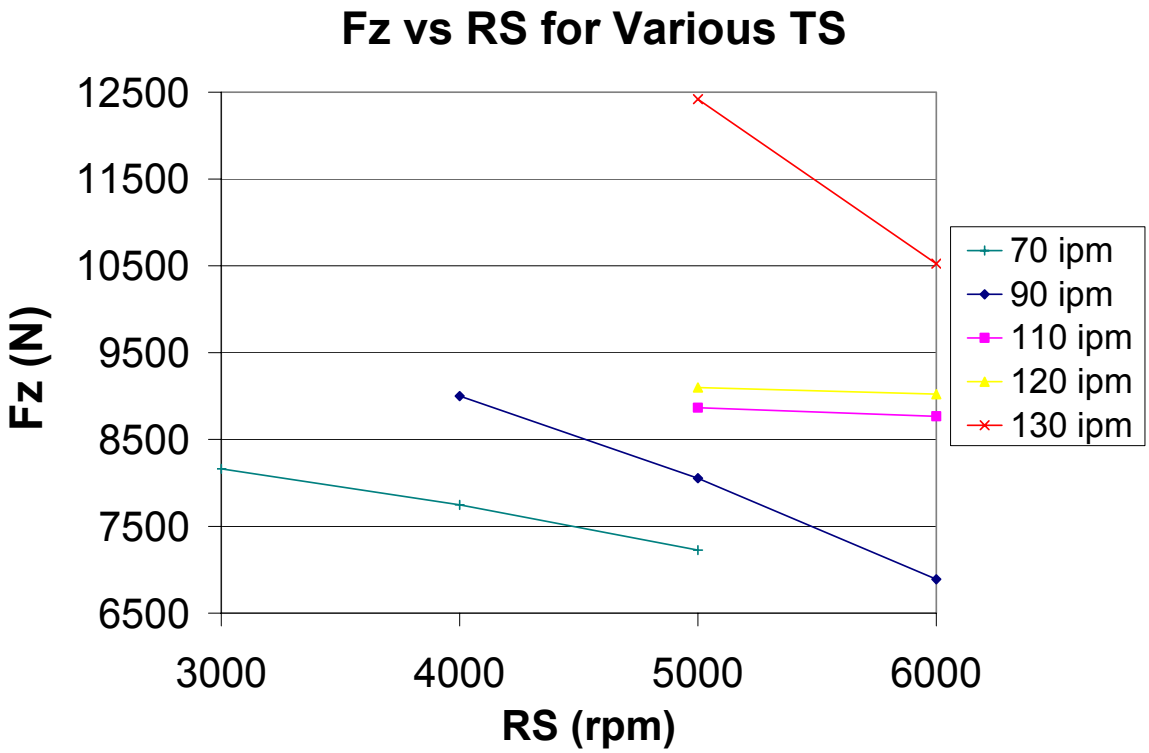

Figure 51: Axial Force vs. Rotational Speed for various TS.

The results of Figures 49-51 show that increasing the rotational speed and holding the travel speed constant leads to a decrease in axial force. Increasing the travel speed and holding the rotational speed constant leads to an increase in axial force.

Welding Torque

The effect of weld pitch variation on the welding torque is key to understanding the friction stir welding process and successfully implementing FSW capable robots. The torque was measured for the weld parameter sets shown in Table 2. The raw data plots can be seen in Appendix A.

The steady state torque is presented in Figures 52-54. The steady state welding torque is found by averaging the mean torque for each run of a weld parameter set. Figures 52-54 show the steady welding torque for variable rotational and travel speed respectively.

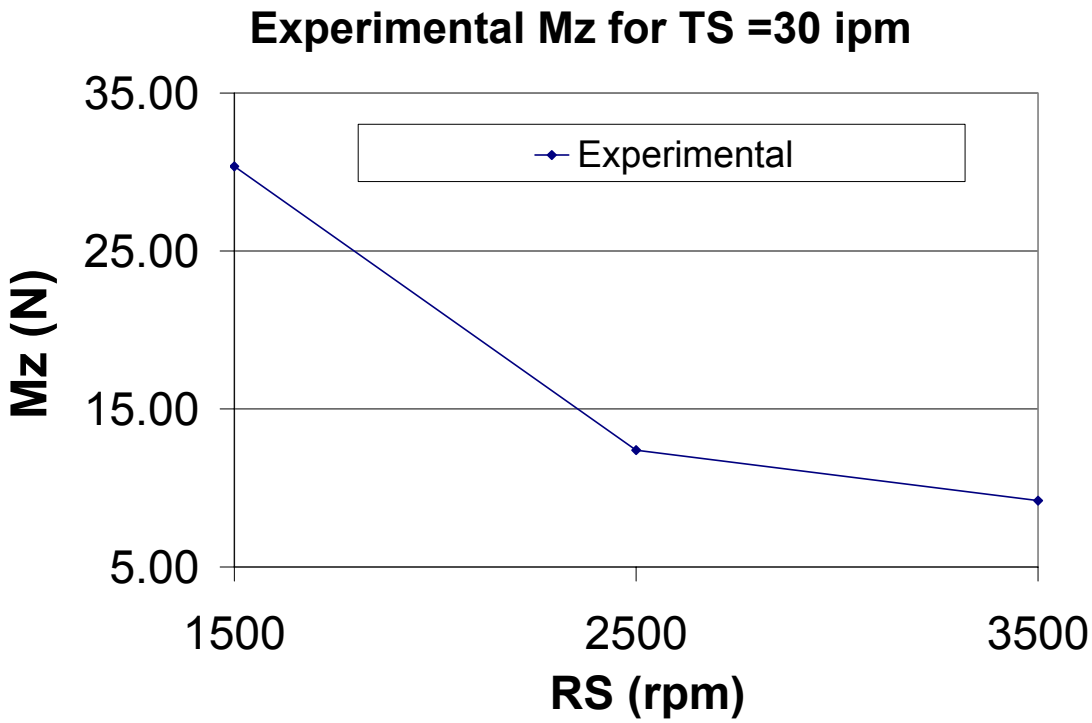

Figure 52: Welding Torque vs. RS for Ts = 30 ipm.

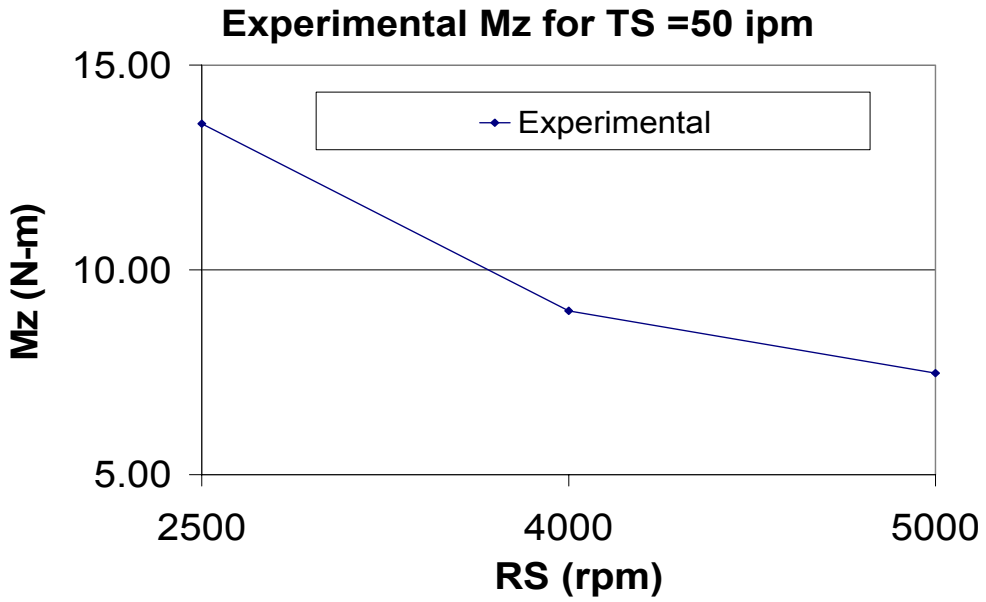

Figure 53: Welding Torque vs. RS for TS = 50 ipm.

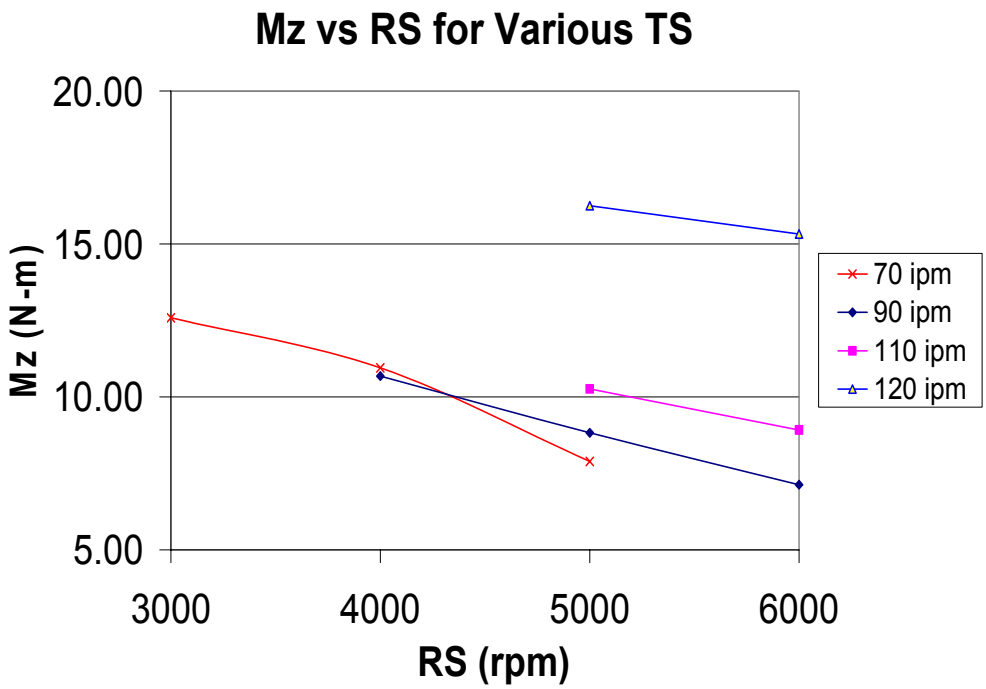

Figure 54: Welding Torque vs. Rotational Speed for various TS.

The results of Figures 52-54 show that increasing the rotational speed while holding the travel speed constant leads to a decrease in torque; while increasing the travel speed and holding the rotational speed constant leads to an increase in torque.

Translational and Transverse Force

The translational and transverse forces were measured for the weld parameter sets shown in Table 2. Each weld parameter set was run a minimum of two times in order to verify the precision of the force data. It was observed by Crawford et al. [40] that the translational and transverse forces have the general trend of decreasing with increased weld pitch, but not with the linear trend as the axial force and torque follow. It was also concluded that observing the translational and transverse force raw data plots provides insight into the contact condition of the weld material at higher rotational speeds. The difference in magnitude of the translation and transverse force during FSW is negligible. Therefore only the translational force plots will be shown here. Figures 55 to 61 show the raw data plots of the translational force for the parametric sets in Table 2.

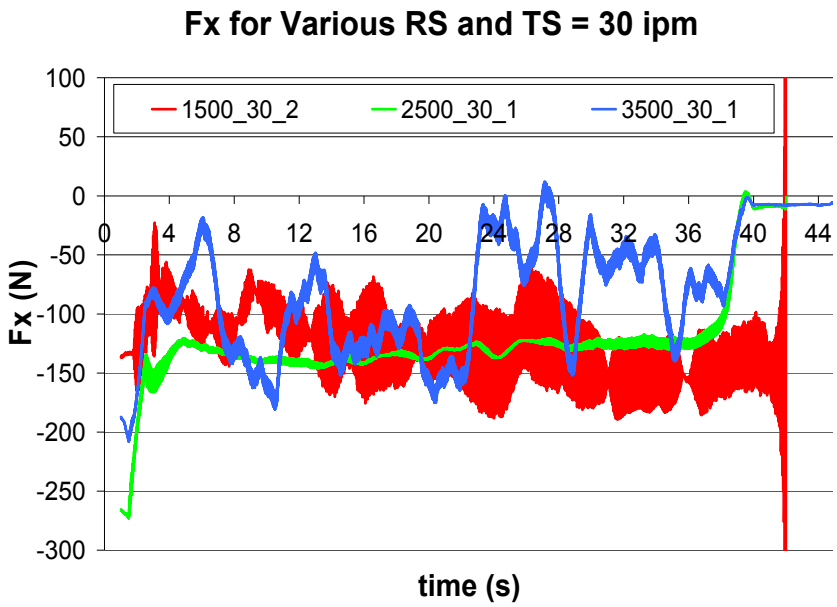

Figure 55: Translation Force for TS = 30 ipm.

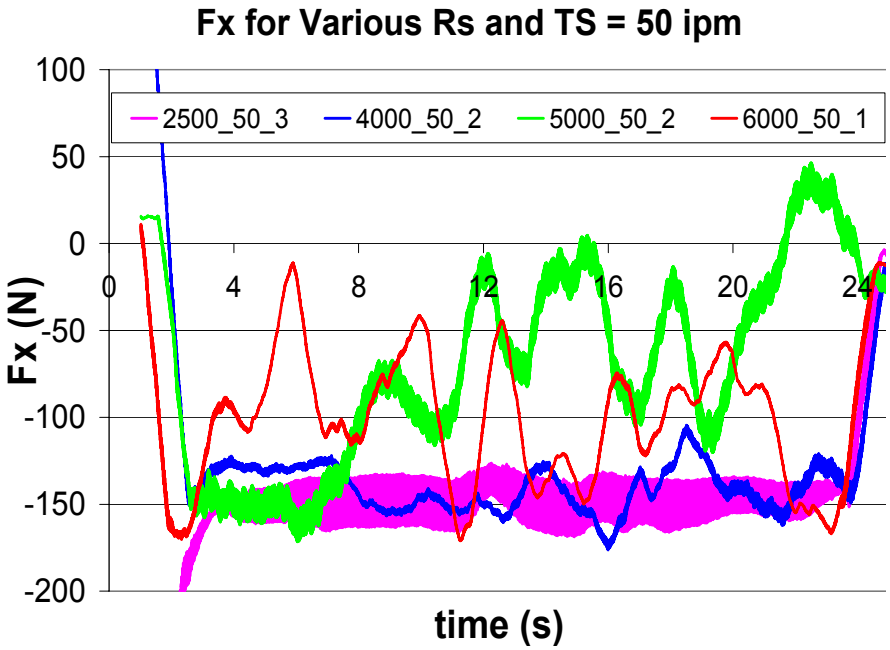

Figure 56: Translation Force for TS = 50 ipm

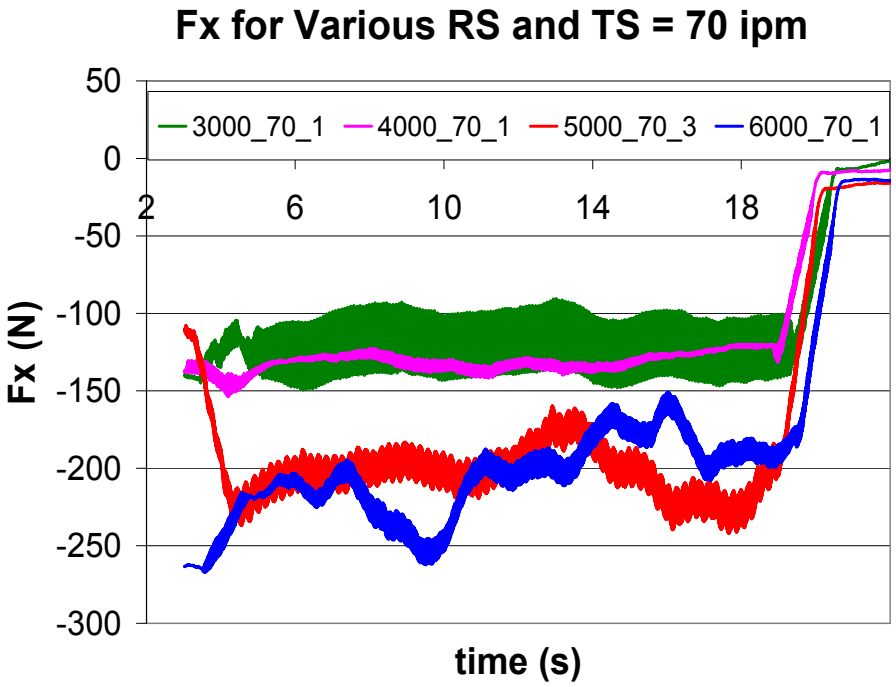

Figure 57: Translation Force for TS = 70 ipm

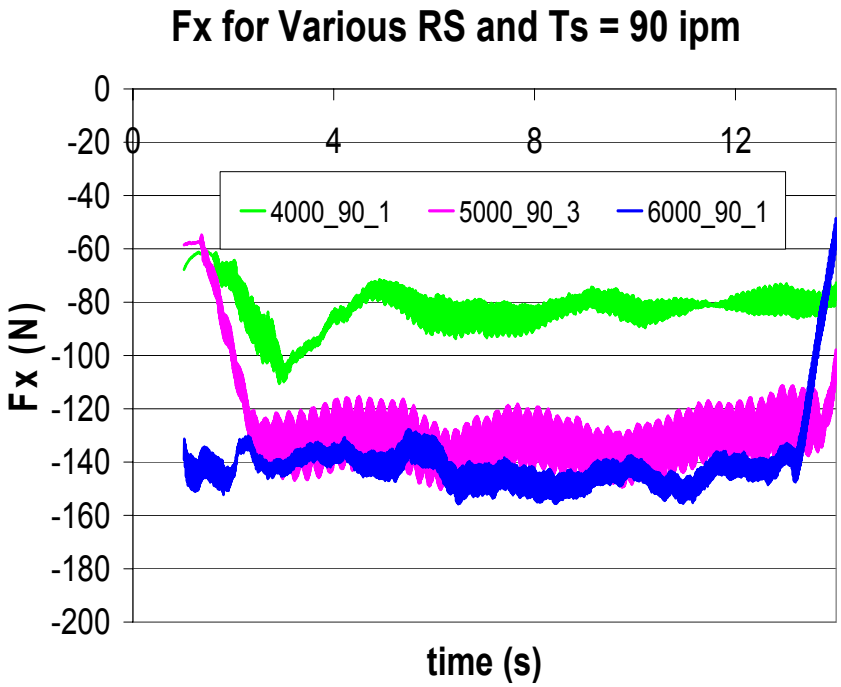

Figure 58: Translation Force for TS = 90 ipm

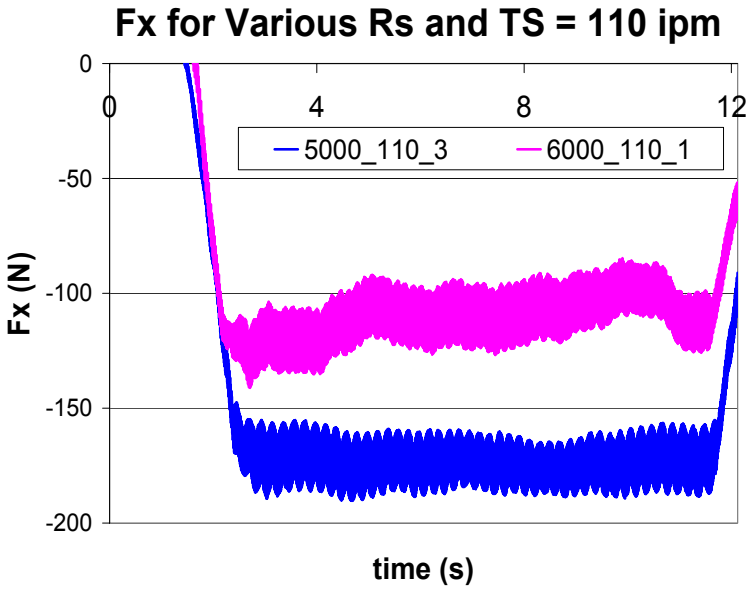

Figure 59: Translation Force for TS = 110 ipm

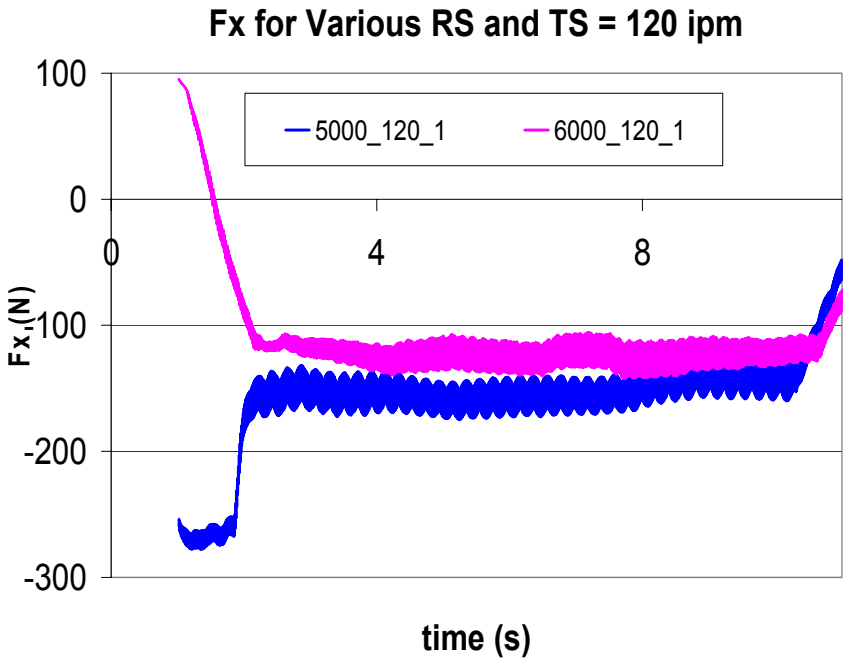

Figure 60: Translation Force for TS = 120 ipm

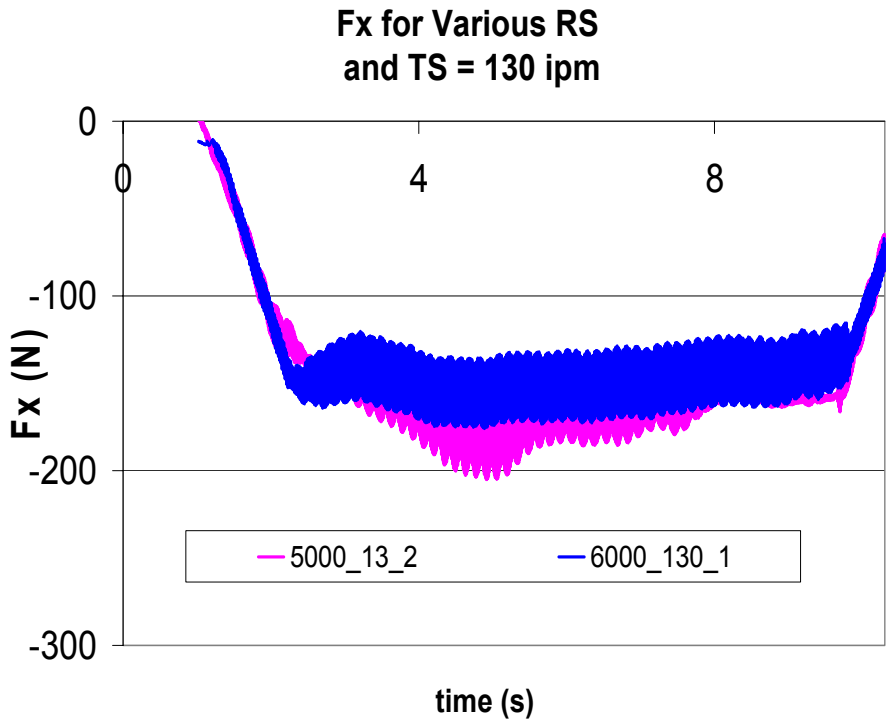

Figure 61: Translation Force for TS = 130 ipm

By observing Figures 55-61, it can be seen that increasing the rotational speed for a constant travel speed causes the translational force curve to fluxuate with more frequency. This fluxuation is perceived to be a varying contact condition at the tool pin/material interface as discussed in Chapter VI.

In Figures 55-61 the constant lines of force indicate a constant pressure at the tool pin/material interface. The fluxuation indicates that the material at the tool pin/material interface does not apply constant pressure but rather it sticks to the tool and drags along behind the tool as it rotates.

With the sticking contact condition, if the friction shear stress exceeds the yield shear stress, the weld material at the tool/material interface will stick to the moving tool

surface segment. In this case, the matrix segment will accelerate along the tool surface (finally receiving the tool velocity), until an equilibrium state is established between the contact shear stress and the internal matrix shear stress. At this point, the stationary full sticking condition is fulfilled [44].

For the sliding condition, if the contact shear stress is smaller than the internal matrix yield shear stress, the matrix segment volume shears slightly to a stationary elastic deformation, where the shear stress equals the 'dynamic' contact shear stress. This state is referred to as the sliding condition [44].

The partial sliding/sticking contact condition is a mixed state of the two contact conditions. In this case, the matrix segment accelerates to a velocity less than the tool surface velocity, where it stabilizes. The equilibrium occurs when the 'dynamic' contact shear stress equals the internal yield shear stress due to a quasi-stationary plastic deformation rate [44].

The variation of the contact condition can reasonably be assumed to be induced by increasing the rotational speed. Increasing the rotational speed causes a corresponding increase in welding temperature. The over-heat phenomena (discussed in Chapter 3 and 6) that occurred at certain welding parameter sets was always preceded by a sliding/sticking contact condition for the lower weld pitch parametric set (rotational speed and travel speed).

Understanding these conditions is key to optimizing a three dimensional model capable of predicting the forces and torques during FSW for various weld pitches and tool geometries. Chapter 8 compiles the results of the optimal mechanical and numerical models determined in Chapters 5 and 6, and simulation data are presented which correlate

the models to the experimental data presented in Chapter VII.

Welding Temperature

As stated in Chapter 3, the welding temperature was measured using a Micron TS7300 infrared camera. Figures 62 – 68 show the raw data plots of welding temperature versus rotational speed.

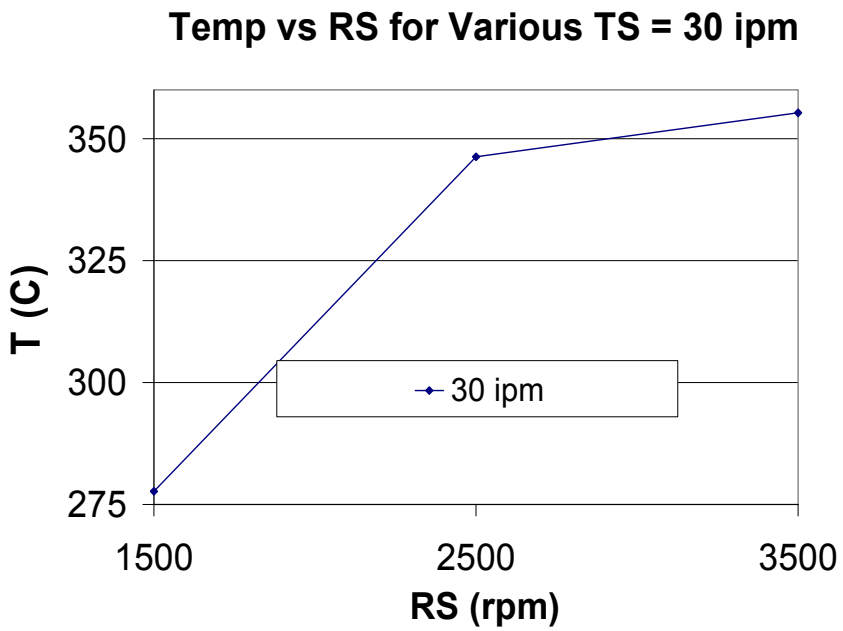

Figure 62: Welding Temperature for TS = 30 ipm.

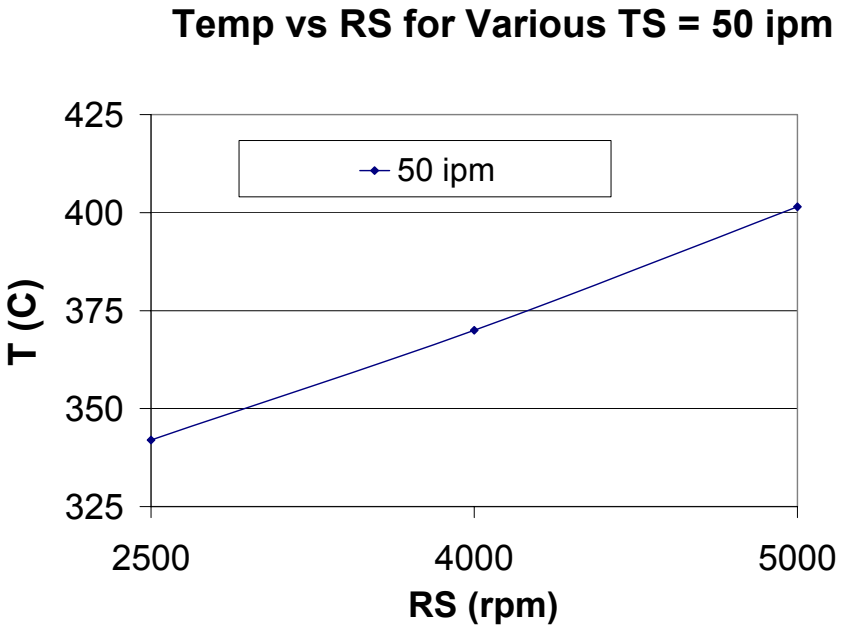

Figure 63: Welding Temperature for TS = 50 ipm.

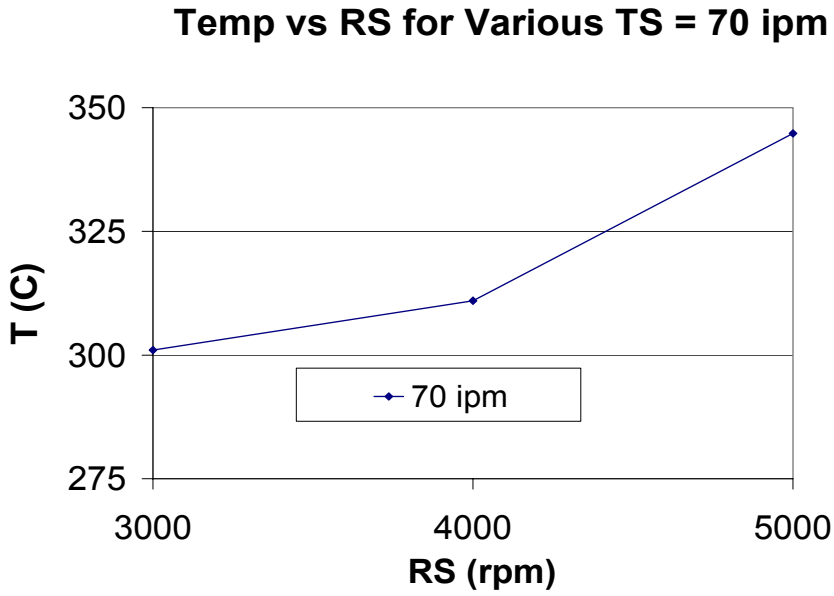

Figure 64: Welding Temperature for TS = 70 ipm.

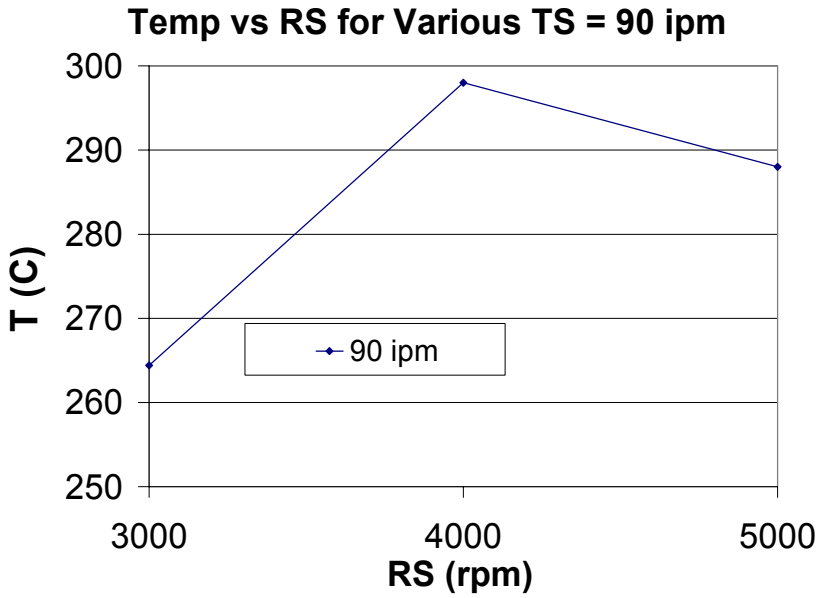

Figure 65: Welding Temperature for TS = 90 ipm

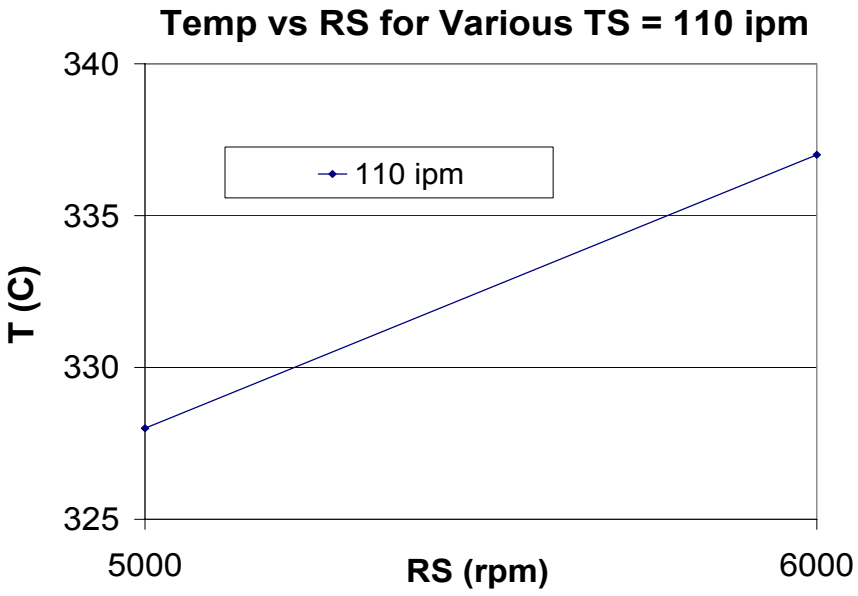

Figure 66: Welding Temperature for TS = 110 ipm

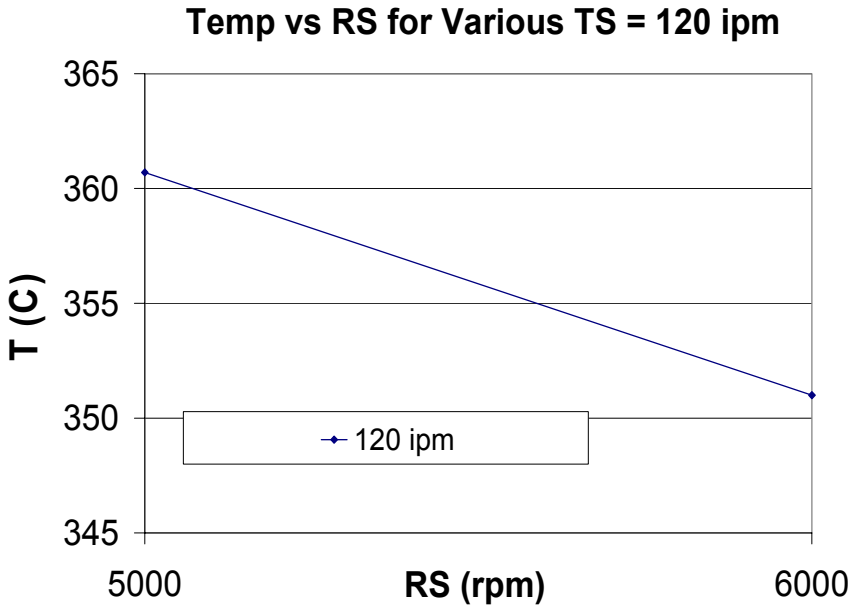

Figure 67: Welding Temperature for TS = 120 ipm.

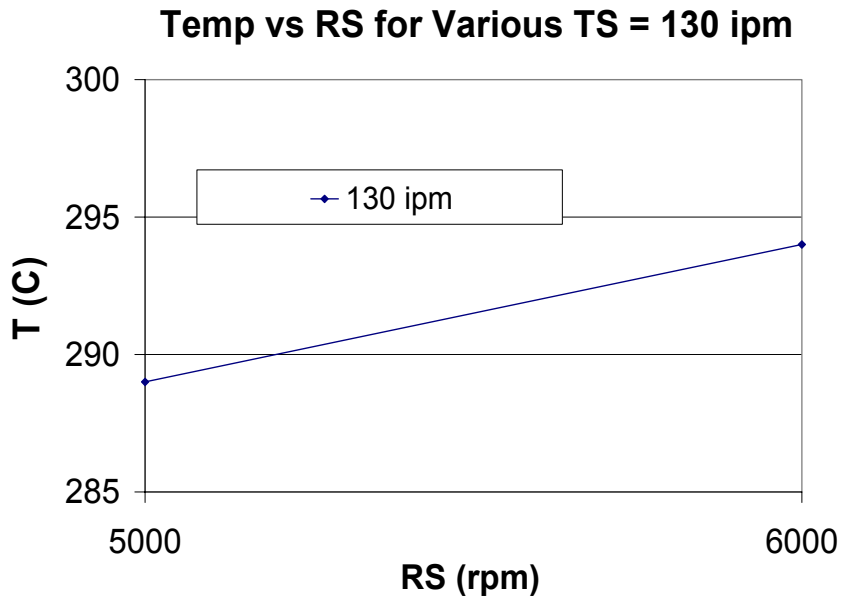

Figure 68: Welding Temperature for TS = 130 ipm.

The welding temperature followed the general trend of increasing with an increase in rotational speed. However, when the welding temperature for various travel

speeds are compared for constant rotational speeds, this relationship is not consistent. Observing Figure 65, it can be seen that a the temperature decreased as the rotation speed was increased from 5000 to 6000 rpm. Intuitively this would be questionable. However, observing the weld surface quality for the 6000 rpm and 90 ipm weld, the weld experienced a large flash buildup, seemingly gorging the weld material. It is important to note that in some runs, the flash would build and would sometimes shear off from contact with the tool shoulder as in Figure 74. This excessive flash buildup acts as a deterrent to temperature buildup. When the extreme flash build up (or gorging) occurs, the weld material is only in contact with the tool for a short time interval, therefore limiting the heat build up due to frictional contact. Figure 70 shows the weld temperature for various rotational speeds and travel speeds. Possible solutions to the excessive flash buildup will be discussed in Chapter IX.

Figure 69: Weld surface for 6000 rpm and 90ipm.

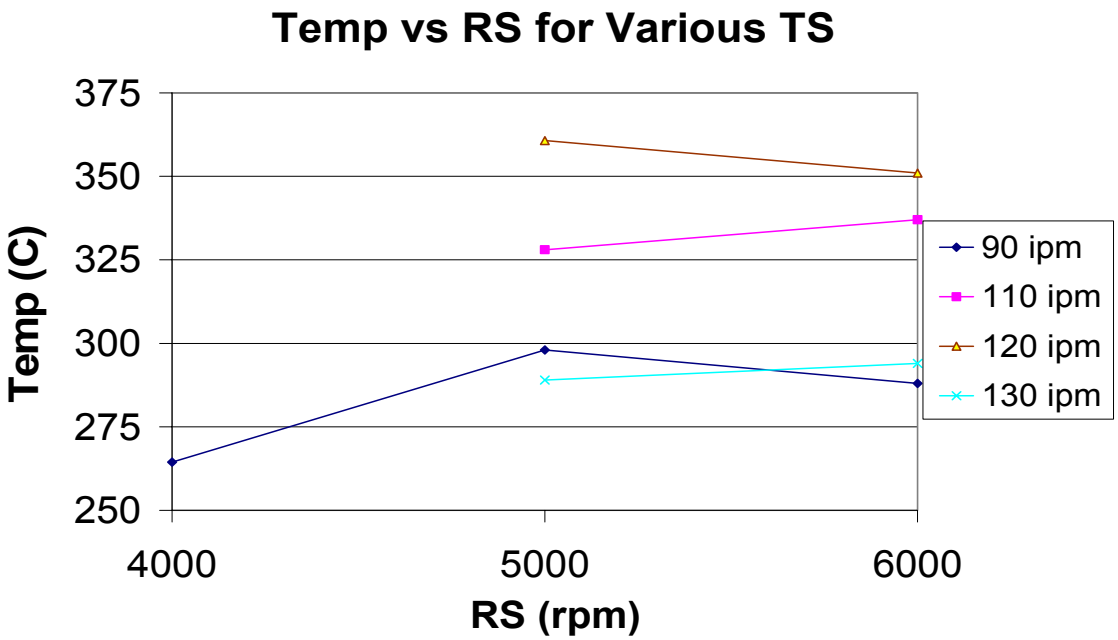

Figure 70: Welding Temperature for various RS and TS.

Weld Quality

Varying the weld pitch is central to optimizing or reducing weld surface quality. In Chapter 6, mechanistic defects were discussed for rotational and travel speeds ranging from 1500-4500 rpm and 11.4-63.3. Macrograph photos of the weld cross sections were presented in the analysis.

Macrographs are currently unavailable (weld matrix in Table 2) for presentation in this dissertation, therefore only the weld surface with defects will be presented here and the cross sections will be an area of follow on work to this dissertation. Figures 71 – 77 show the weld surfaces or welds which experienced moderate to extreme surface deformation.

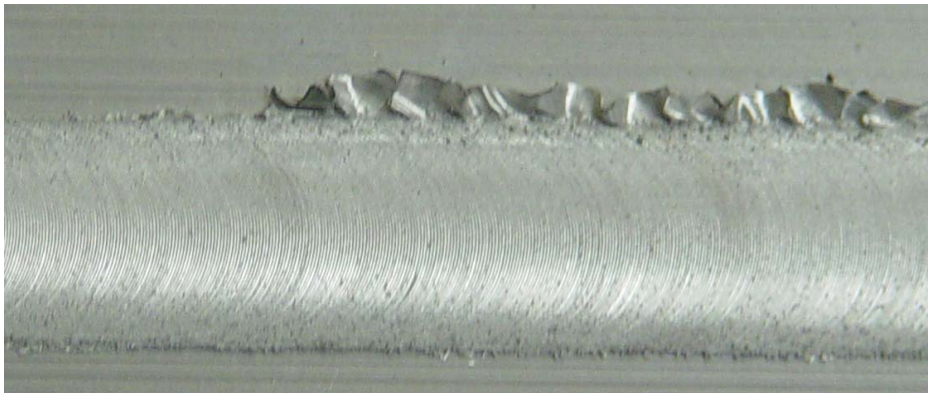

Figure 71: Weld Surface for 3500 rpm and 30 ipm.

Figure 72: Weld Surface for 5000 rpm and 50 ipm.

Figure 71 corresponds to a weld pitch of 116 rpi. This weld experienced moderate flash build up very similar to the results in Chapter 6 for 3750 rpm and 37 ipm. Observing Figures 72-74, it can be seen that the high weld pitch regimes not only gorged the weld, but also created a line of discontinuity running the length of the weld. Generally when the line of discontinuity developed [40], an increase in tool depth, subsequently increasing tool pressure, would eliminate the discontinuity. However, welds where this technique is most effective, do not have large flash build up.

Figure 73: Weld Surface for 6000 rpm and 50 ipm.

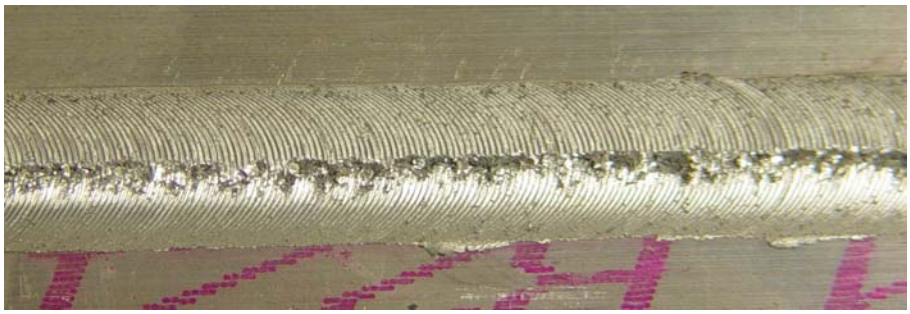

Figure 74: Weld Surface for 6000 rpm and 90 ipm.

Figure 74 and 75 show that for 6000 rpm, increasing the travel speed from 90 ipm to 110 ipm improved the weld surface quality. Though not shown in Figure 74-77, a layer of flash formed and was sheared of by the tool during welding. This shearing often occurs because of the extreme speed with which the tool is traversed along the weld line.

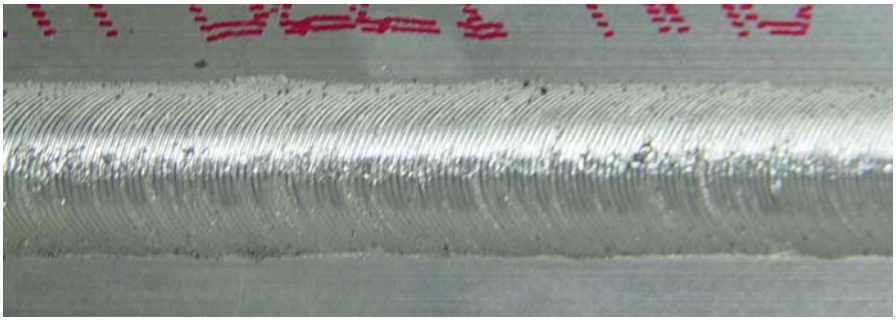

Figure 75: Weld Surface for 6000 rpm and 110 ipm.

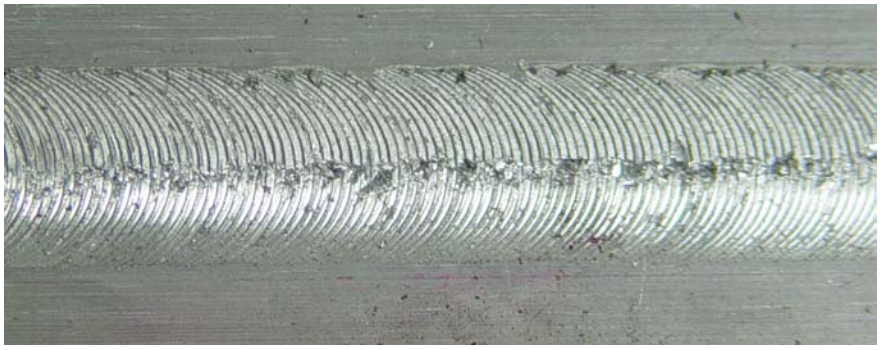

Figure 76: Weld Surface for 6000 rpm and 120 ipm.

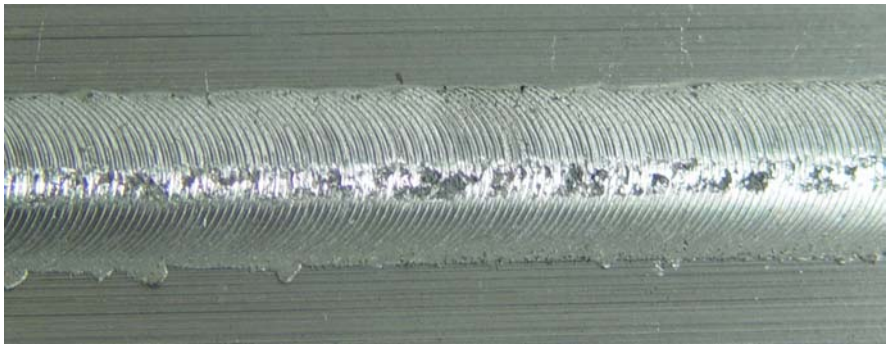

Figure 77: Weld Surface for 6000 rpm and 130 ipm.

Figures 76 and 77 show that the weld surface quality deteriorates with an increase in travel speed. Analyzing how the increase in travel speed affects the weld time interval lends insight into this phenomena.

At 90 and 110 ipm, the tool travels 1 inch in 0.67 and 0.54 seconds respectively. While at 30 and 50 ipm, the tool travels 1 inch in 2.0 and 1.20 seconds. The weld pitch at 6000 rpm, 90 ipm, and 110 ipm is 66 and 54 rpi respectively. For the corresponding weld pitch at 30 and 50 ipm, Crawford et al. [40] showed that these parametric regimes produced high quality welds both internally and at the weld surface.

The significant difference in time interval shows that at high travel speeds, the weld quality is not only a function of weld pitch, but also of a term we will call the weld consolidation time (wct).

During the weld consolidation time, time critical events must occur. First the material must be able to come into contact with the tool for a time interval long enough for there to be sufficient frictional heating of the weld material. Next, as the material is stirred to the rear edge of the tool, the time interval must allow the material to adequately cool and be consolidated under the back pressure of the tool in order to form the solid state bond which constitutes friction welding.

At low travel speed (11.4-70 ipm), the upper bound of the operational ceiling for the increased rotational speed/decreased force relationship and weld quality is limited by the weld pitch where the shoulder deforms the weld surface. While the lower bound is lowest weld pitch which leads to wormhole development and subsequent tool failure.

At high travel speed (70- 130 ipm), the upper bound of the operational ceiling for the increased rotational speed/decreased force relationship and weld quality is limited by

the high weld pitch where tool rotational speed moves material so rapidly that the rotational speed acts in concert with the reduced weld consolidation time in not allowing the solid phase bond which constitutes friction stir welding to form. The lower bound is similar to the lower bound for low travel speed, where low weld pitch leads to wormhole development and subsequent tool failure. For example, at 1500 rpm/50 ipm and 4000 rpm/120 ipm, the tool pin fractured. These parameters have a weld pitch of 30 and 33.3 rpi respectively.

Chapter 8 will present a compilation of the results of Chapters 5-7. The Visco-Plastic fluid flow model is used in conjunction with the threaded pin numerical model to simulate the welds in Table 2. The welding temperature presented in Chapter 7 (Figure 62-68, and 70) is used as the input temperature for the isothermal numerical model presented in Chapter 8.

CHAPTER VIII

HIGH SPEED NUMERICAL RESULTS

This chapter compares the experimental results of Chapter 7 with the 3-D threaded pin numerical model.

The numerical models are implemented using the computational fluids dynamics package FLUENT and employ the Visco-Plastic fluid flow model for the viscosity determination. The results are compared to experimental data for AA 6061-T6 friction stir welded at rotational and travel speeds ranging from 1500-6000 rpm and 30-130 ipm.

Axial Force

The simulation axial force on the tool is computed as defined in Chapter 6. For the threaded pin model, no reference pressure was used because of the inclusion of the backing plate. From Figures 78-84, it can be seen that during these experiments, the machine used for FSW may be called upon to deliver and consistently maintain an axial force of 1-14 kN depending on the tool dimensions and welding parameters.

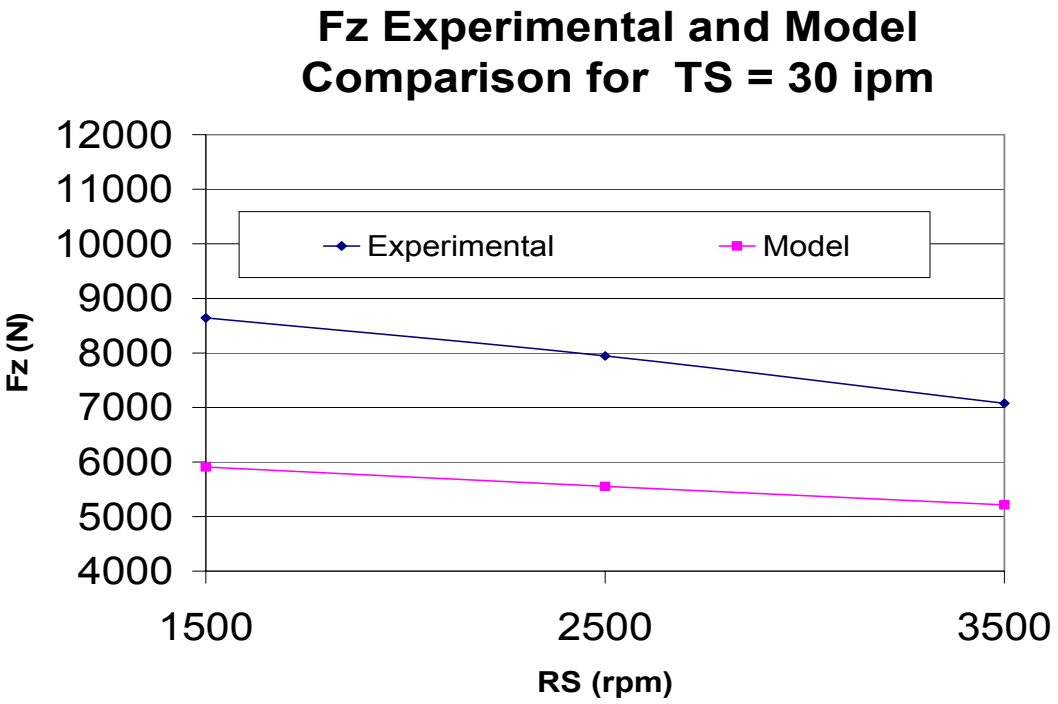

Figure 78: Axial Force for experimental and simulations for TS = 30 ipm.

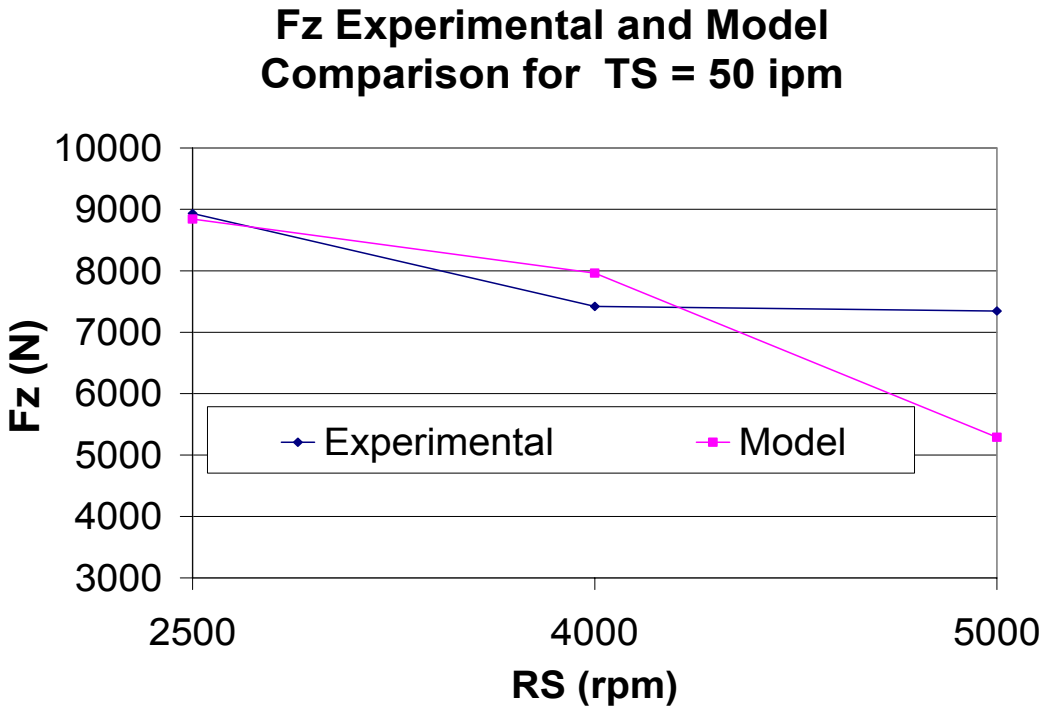

Figure 79: Axial Force for experimental and simulations for TS = 50 ipm.

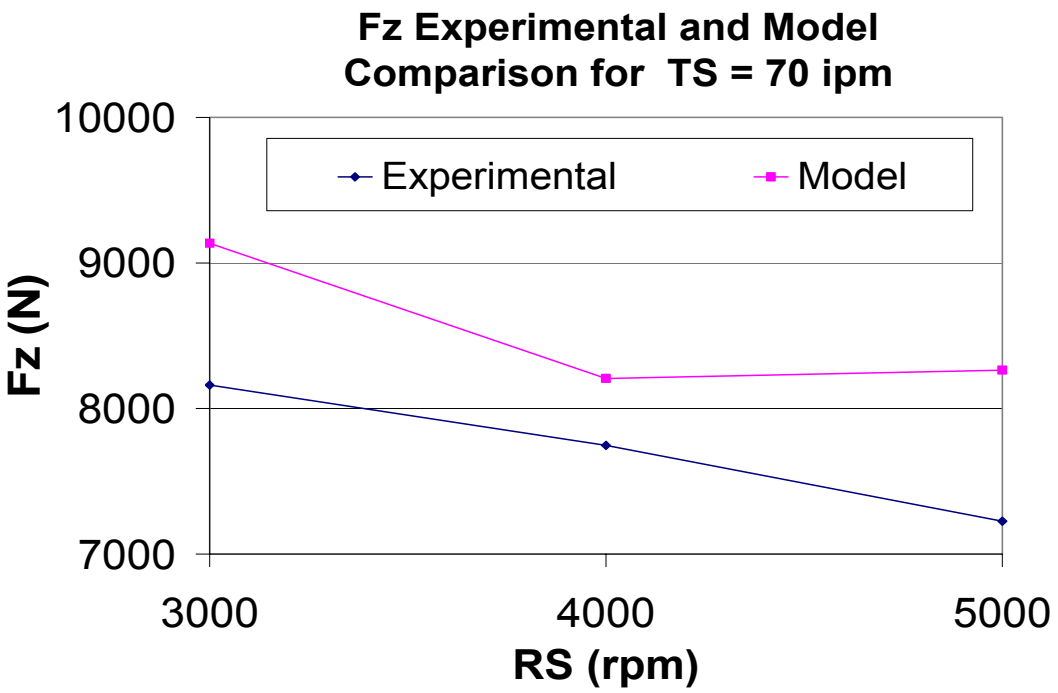

Figure 80: Axial Force for experimental and simulations for TS = 70 ipm.

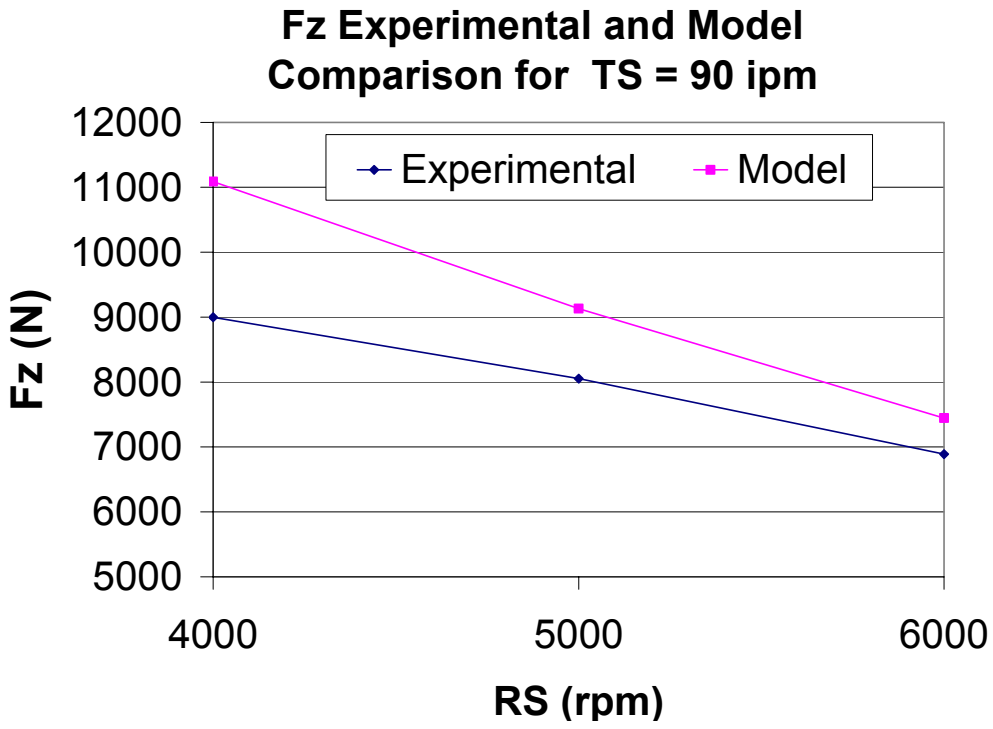

Figure 81: Axial Force for experimental and simulations for TS = 90 ipm.

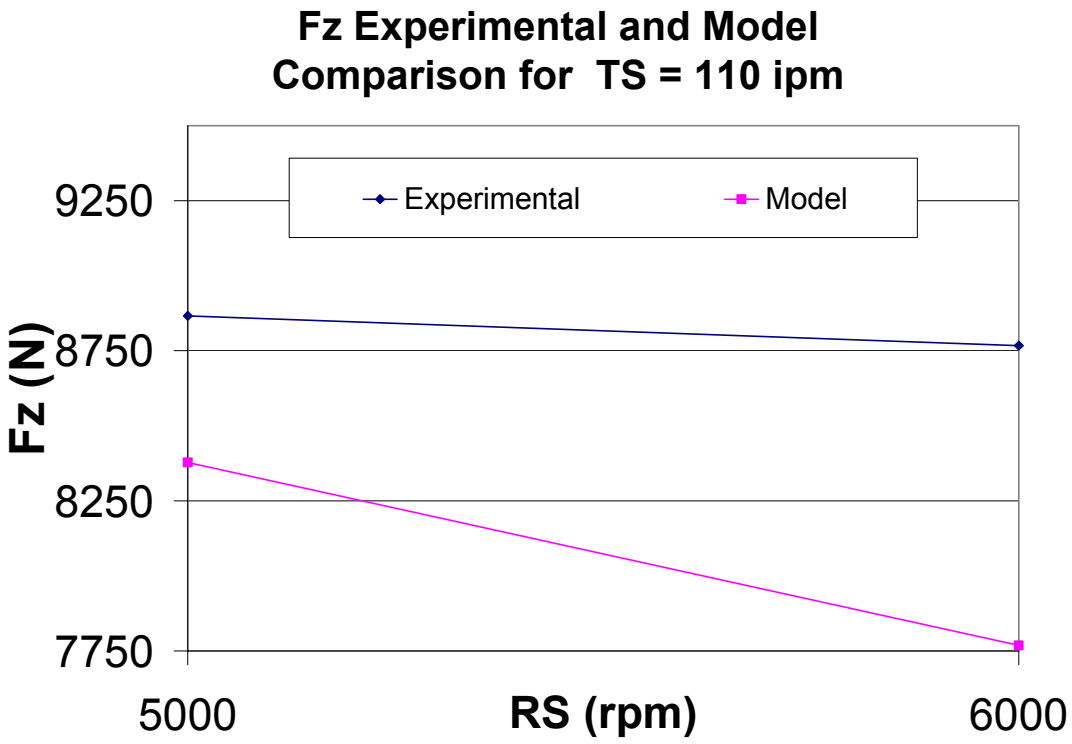

Figure 82: Axial Force for experimental and simulations for TS = 110 ipm.

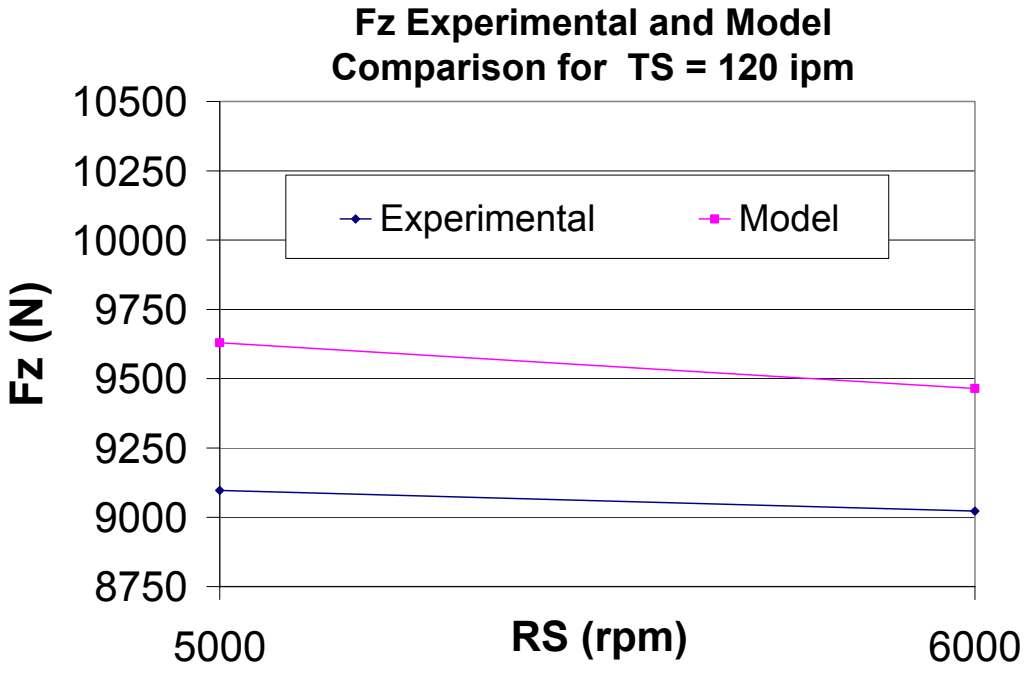

Figure 83: Axial Force for experimental and simulations for TS = 120 ipm.

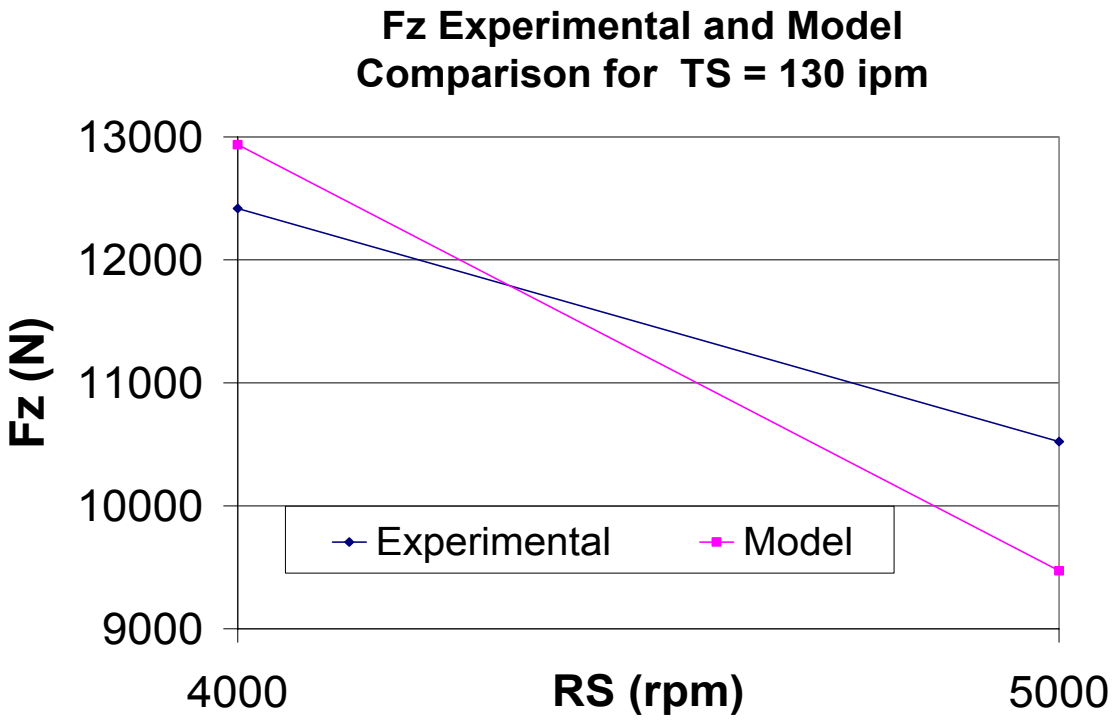

Figure 84: Axial Force for experimental and simulations for TS = 130 ipm.

From Figures 78-84, we can see that the model correlates well with the experimentally measured axial force. Also evident is the trend of the axial force to decrease as the rotational speed is increased for a constant travel speed. By inspection of Figures 78-84, it can be seen that as the weld pitch increases, the simulation data for the model begins to converge with the experimental data.

From Figures 78-84, it is clear the optimum operating parameters for robotic FSW will require high rotational speeds and low travels speeds.

Welding Torque

From Figure 85-90, it can be seen that during these experiments, the machine used for FSW may be called upon to deliver and consistently maintain a torque of about

50 N-m, which depends greatly on the tool dimensions and welding parameters.

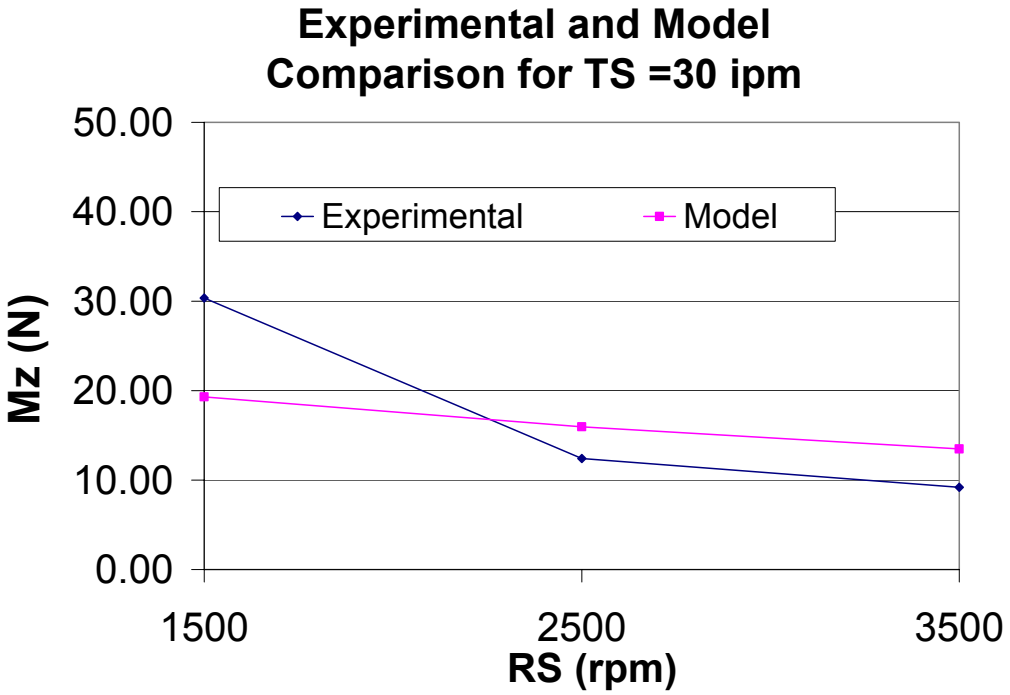

Figure 85: Welding Torque for experimental and simulations for TS = 30 ipm.

By inspection of Figures 85-90, it can be seen that as the weld pitch increases, the simulation data generally converges with the experimental data with only a small divergence at the very high weld pitch parametric sets. One possible reason for this behavior is the contact condition at the tool pin material interface. At the high weld pitch it is believed that the contact condition at the tool pin material interface is sliding/sticking. However a no-slip (or sticking contact condition) was used in the simulation. Therefore in the simulation more material is "stirred" at the tool pin/material interface where as in the experiment there is assumed to be some material slippage. This increase in contact material would result in more torque required to "stir" the weld

material.

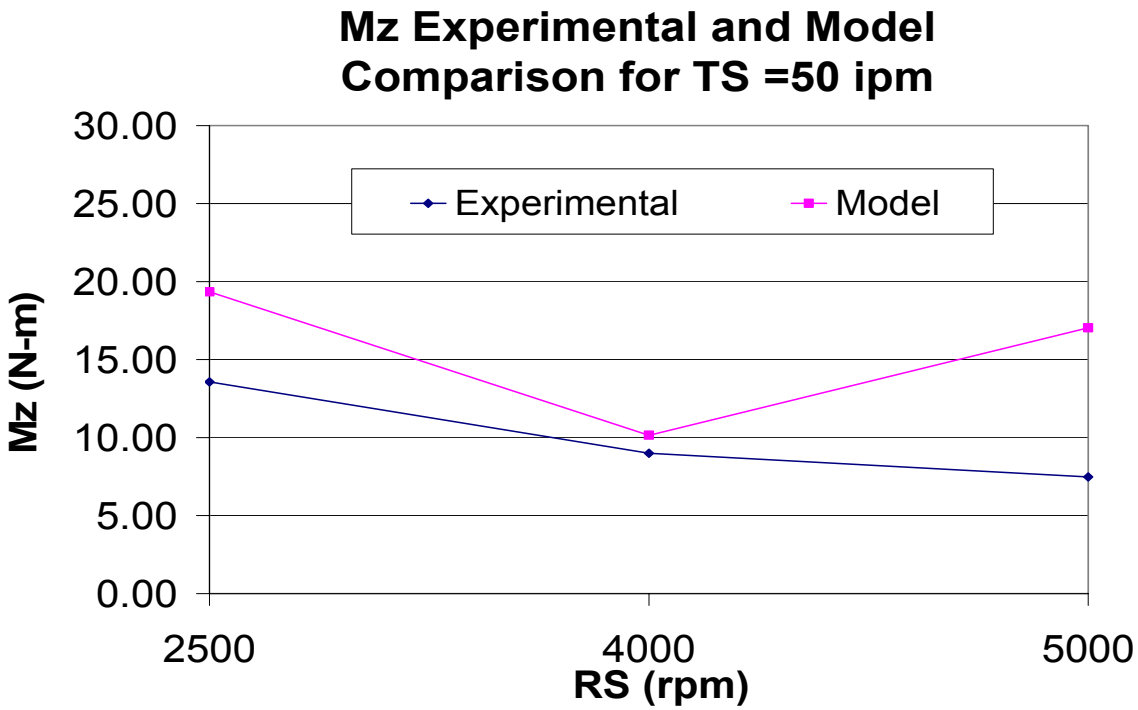

Figure 86: Welding Torque for experimental and simulations for TS = 50 ipm.

In general the torque follows the same trend as the axial force, where an increase in weld pitch has a corresponding decrease in torque. Likewise, a decrease in weld pitch has a corresponding increase in welding torque.

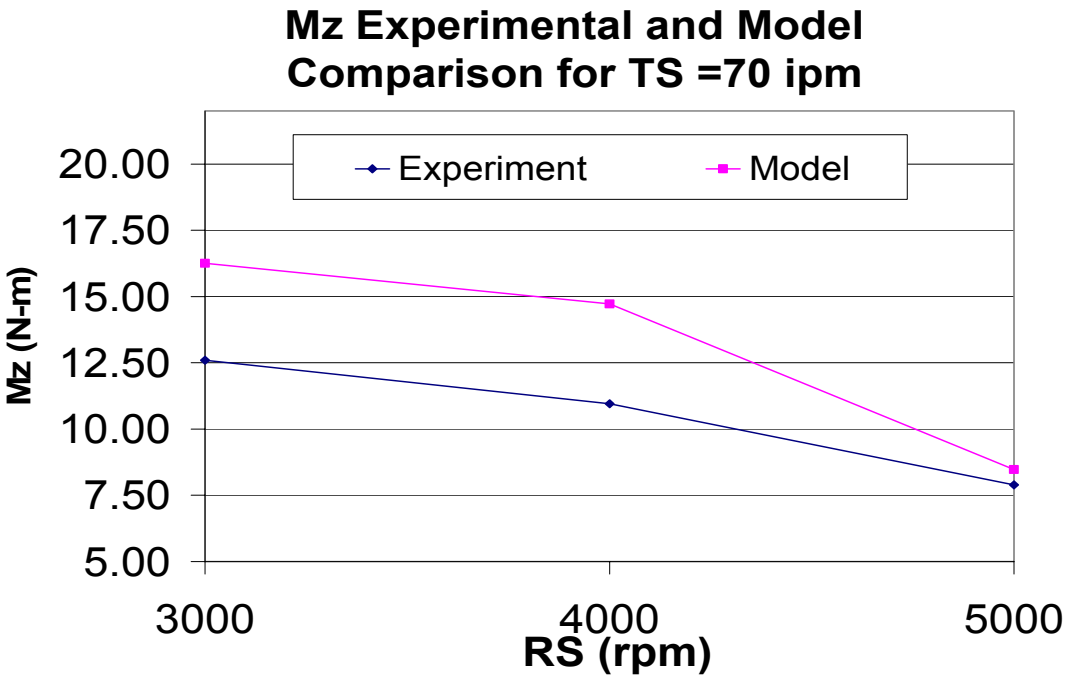

Figure 87: Welding Torque for experimental and simulations for TS = 70 ipm.

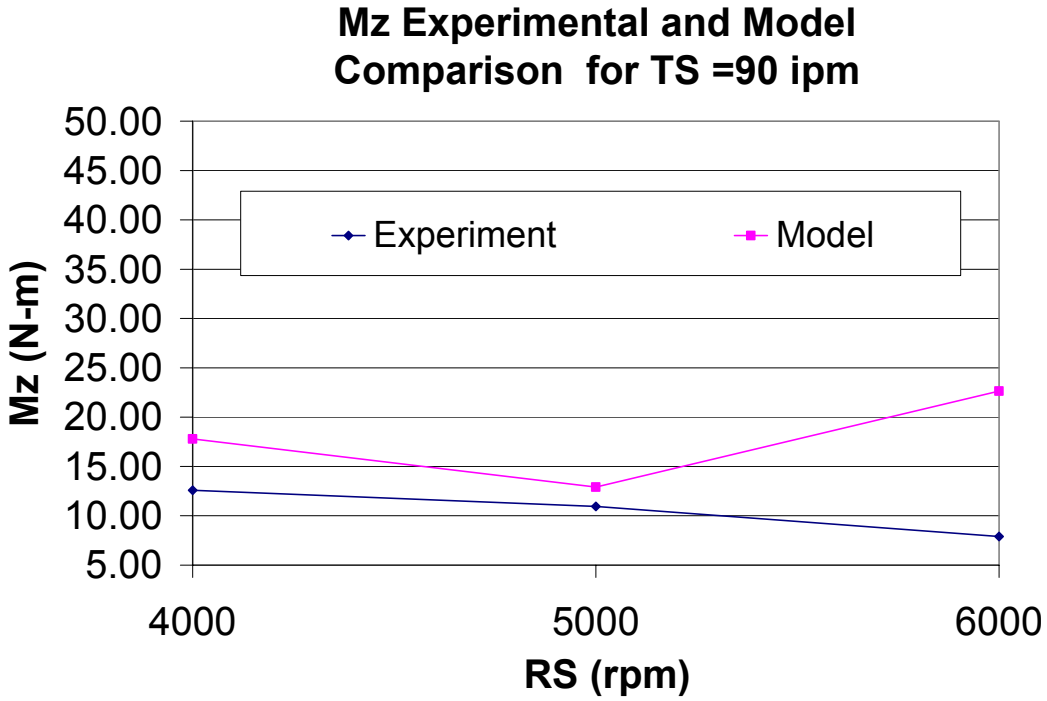

Figure 88: Welding Torque for experimental and simulations for TS = 90 ipm.

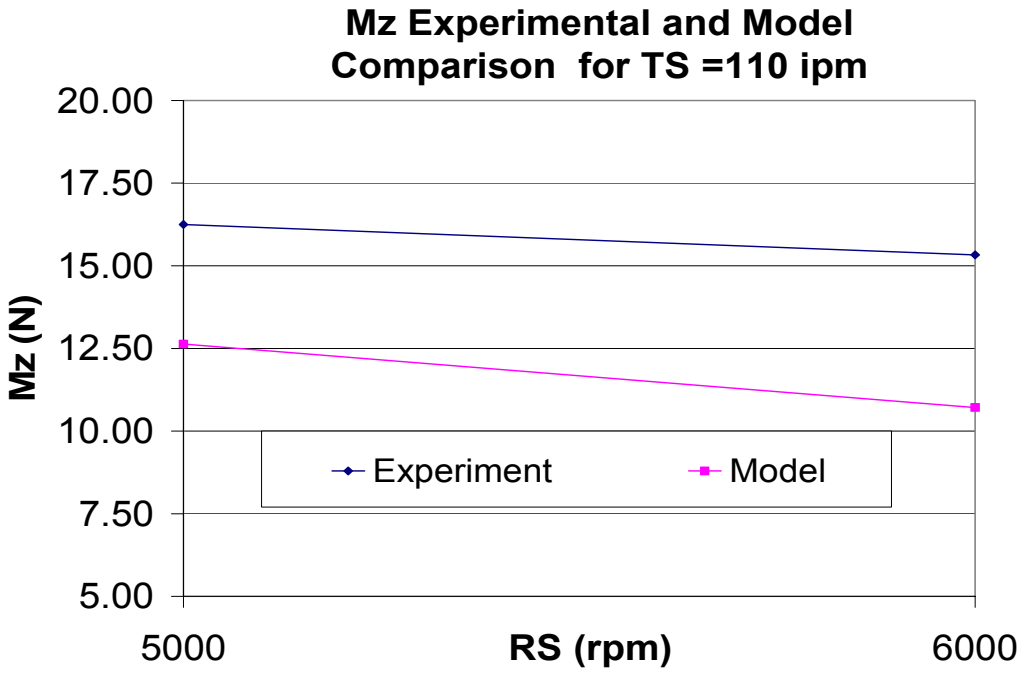

Figure 89: Welding Torque for experimental and simulations for TS = 110 ipm.

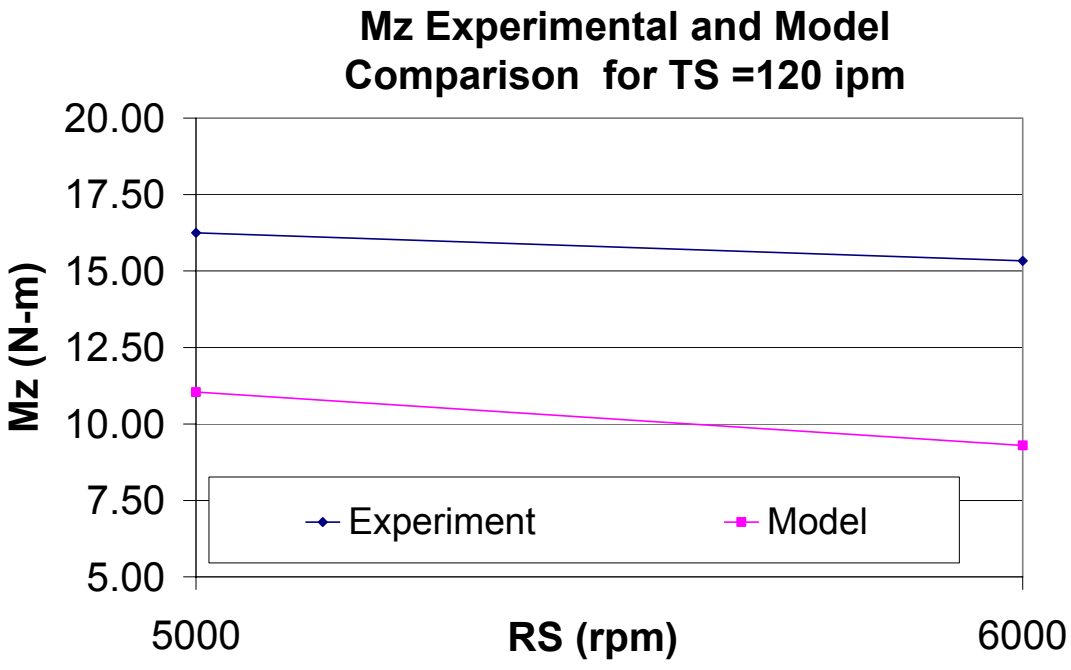

Figure 90: Welding Torque for experimental and simulations for TS = 120 ipm.

Welding Temperature

As stated in Chapter 4 -7, the simulations used isothermal temperature models. Meaning, to optimize the simulations to predict the steady state forces and torque, the steady state temperature (simulated for the results in Chapter 5 and 6 and measured for the results to be presented in this chapter) was an input parameter.

Figures 91 and 92 show a temperature contour plot for 1500 and 2500 rpm for a travel speed of 30 ipm.

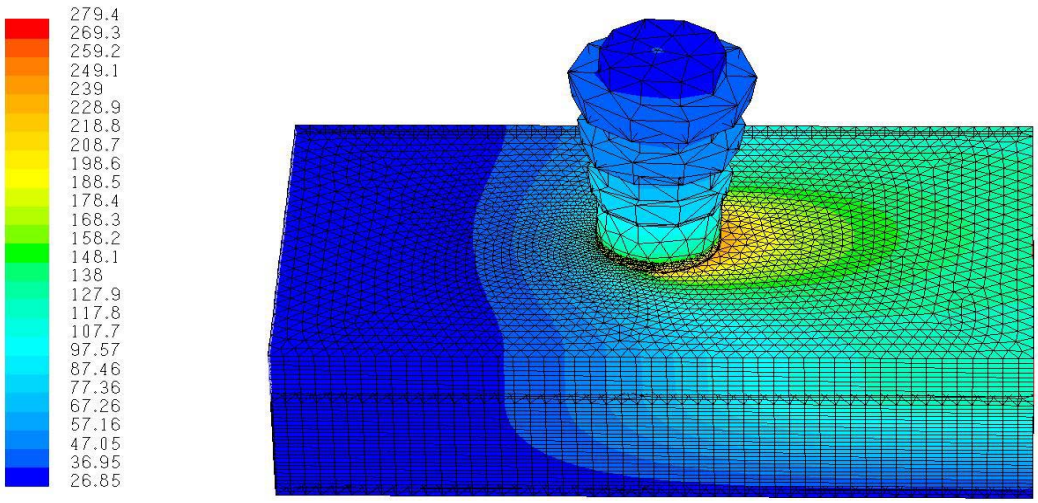

Figure 91: Sample temperature contour (in ºC) for 1500 rpm and 30 ipm.

The surface contour plots generally followed the same patterns of temperature distribution for each welding parameter set, however there is a significant increase in maximum temperature as shown in Figure 92.

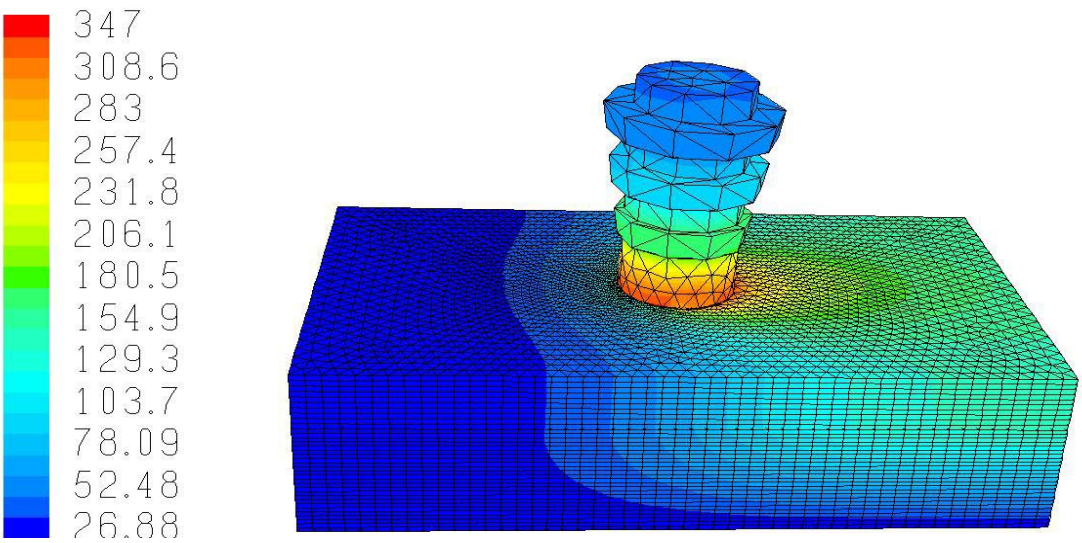

Figure 92: Sample temperature contour (in ºC) for 2500 rpm and 30 ipm.

Observing the temperature distribution at the tool pin and shoulder/weld material interface lend insight into how heat distribution may correlate to weld defect development. Figures 93 and 94 show lateral cross sectional views of the temperature contour at the tool pin material interface.

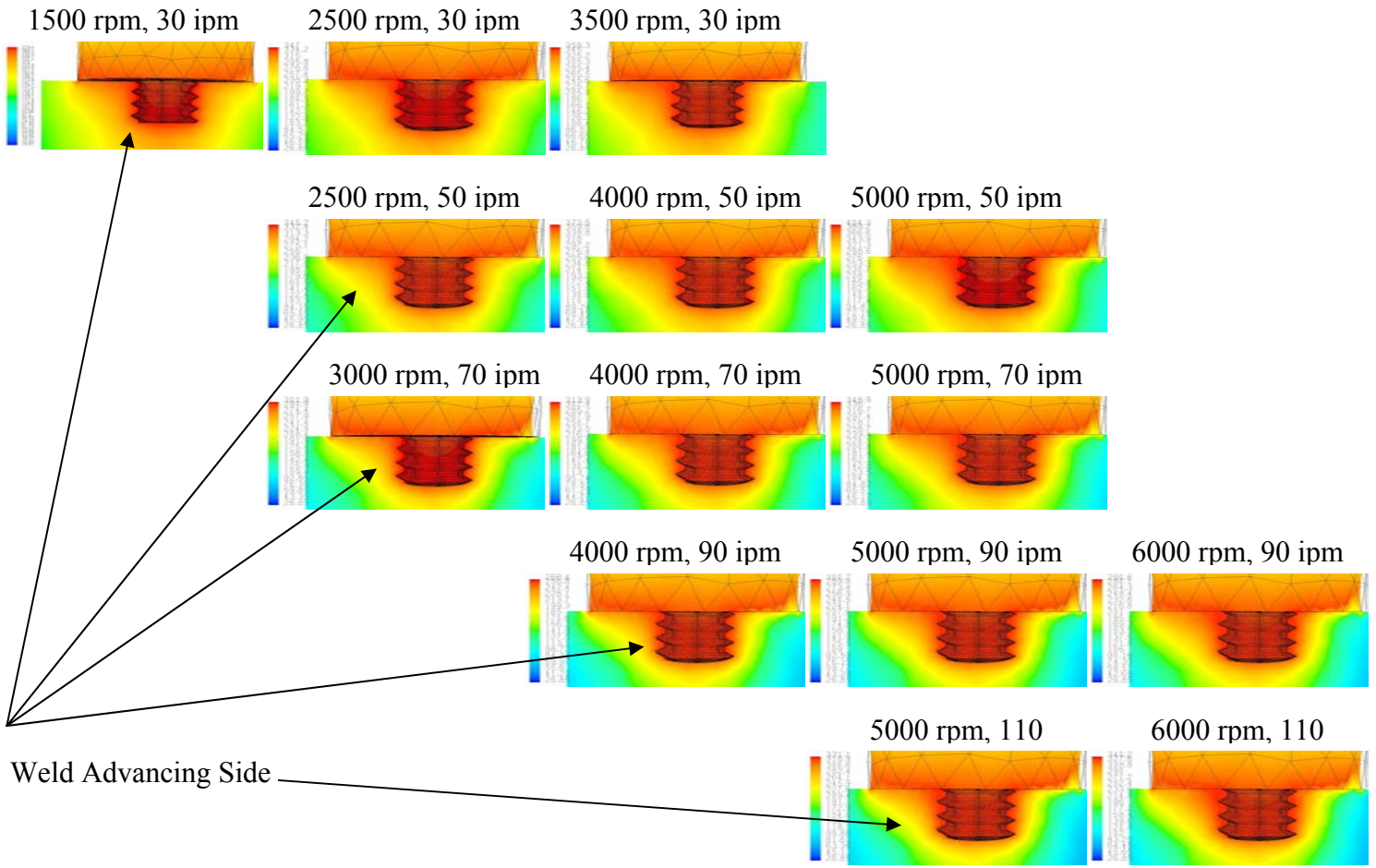

Figure 93: lateral cross section of tool pin temperature contour (in ºC) for various RS and TS = 30 10 110 ipm.

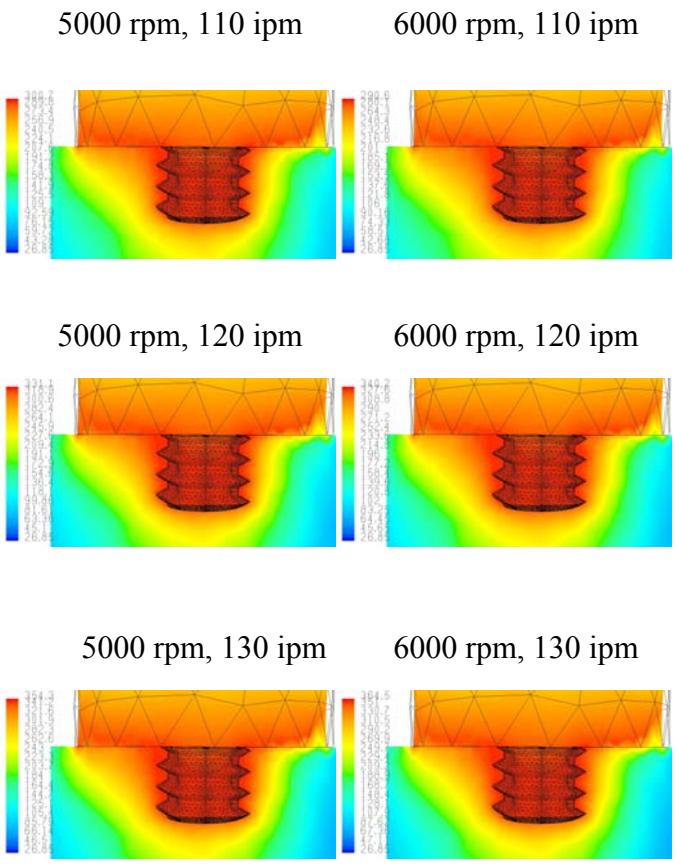

Figure 94: Lateral cross section of tool pin temperature contour (in ºC) for Various RS and TS = 110 to 130 ipm.

.

From Figures 93 and 94, it can be seen that for a constant travel speed, an increase in rotational speed causes the temperature distribution at the tool pin material interface to expand laterally towards the advancing side. These results correlate very well with the simulations presented in Chapter 6 and with the weld photos shown in Chapter 7.

Inspection of Figures 93 and 94 also show that for a constant rotational speed, increasing the travel speed cause the depth of vertical temperature distribution to decrease. The vertical temperature distribution is believed to increase the ability of the material to flow downward thus preventing the wormhole defect formation.

CHAPTER IX

CONCLUSIONS AND RECCOMMNEDATIONS

Experimental Results

The experimental data presented in this dissertation showed that the increased weld pitch/decreased force and torque relationship exists for rotational and travel speeds ranging from 1500-6000 rpm and 30-130 ipm respectively. Decreasing the travel speed was shown to be the most effective method for reducing the axial force and torque.

Two types of mechanistic defects were observed; worm holes and weld deformation due to surface overheating. Worm holes were found to develop due to a lack of downward material flow to the bottom of the weld. The lack of flow appeared to occur because of low weld pitch, or rather insufficient rotational speed for the weld travel speed. It is observed that for $w_p < 33$ rpi a wormhole is likely to develop as well as tool breakage. For example, at 1500 rpm/50 ipm and 4000 rpm/120 ipm, the tool pin broke. These parameters have a weld pitch of 30 and 33.3 rpi respectively.

For low travel speeds (30-70 ipm), the weld deformation due to surface overheating was found to occur at high weld pitches of high rotational speeds to low travel speeds. It is observed that for $w_p > 110$ rpi, surface defect in the form of excess flash is likely to develop.

The welding temperature followed the general trend of increasing with an increase in rotational speed. However, when the welding temperature for various travel speed are compared for constant rotational speeds, this relationship is not consistent.

Using the current tool, weld surface quality was shown to degrade at high weld

pitch regimes for high travel speeds (70-130 ipm). A new relationship became apparent. At 90 and 110 ipm, the tool travels 1 inch in 0.67 and 0.54 seconds respectively. While at 30 and 50 ipm, the tool travels 1 inch in 2.0 and 1.20 seconds. The weld pitch at 6000 rpm, 90 ipm, and 110 ipm is 66 and 54 rpi respectively. For the corresponding weld pitch at 30 and 50 ipm, Crawford et al. [40] showed that these parametric regimes produced high quality welds both internally and at the weld surface.

The significant difference in time interval shows that at high travel speeds, the weld quality is not only a function of weld pitch, but also of the weld consolidation time (wct). The weld consolidation time, can be defined as the time necessary for the solid state bond which constitutes friction welding to occur.

During the weld consolidation time, critical events must occur. First the material must be able to come into contact with the tool for a time interval long enough for there to be sufficient frictional heating of the weld material. Next, as the material is stirred to the rear edge of the tool, the time interval must allow the material to adequately cool and be consolidated under the back pressure of the tool in order to form the solid state bond which constitutes friction welding.

At low travel speed (11.4-70 ipm), the upper bound of the operational ceiling for the increased rotational speed/decreased force and torque relationship and weld quality is limited by the weld pitch where the shoulder deforms the weld surface. While the lower bound is lowest weld pitch which leads to wormhole development and subsequent tool failure.

Potential solutions for the weld deformation at low travels speeds are implementation of a force feedback control scheme [45] or the non-rotating tool should

[46]. The wormhole can be eliminated by simply increasing the rotational speed.

At high travel speed (70- 130 ipm), the upper bound of the operational ceiling for the increased rotational speed/decreased force relationship and weld quality is limited by the high weld pitch where tool rotational speed in acts concert with the reduced weld consolidation time in disallowing the solid phase bond which constitutes friction stir welding to form. The lower bound is similar to the lower bound for low travel speed, where low weld pitch leads to wormhole development and subsequent tool failure.

A potential solution to the upper bound at high travel speeds is to use a scaled rotational speed tool design. A scaled speed tool implies that the rotational speed of the tool shoulder is less than the tool pin by some experimentally determined factor.

For example, at 130 ipm, 5000 rpm produces a weld of satisfactory surface quality, while 6000 rpm deforms the weld surface and leaves a line of discontinuity. However the axial forces during the 6000 rpm are less than that of the 5000 rpm at 130 ipm. Rotating the shoulder at 5000 rpm, and the tool pin at 6000 rpm would theoretically allow for the exploitation of the increased weld pitch/decreased force relationship.

Modeling Results

At low weld pitches, the Couette flow model did not correlate as well with the experimental results as did the Visco-Plastic flow model. As the weld pitch increased, the experimental results and the Couette Flow model began to converge. This implies that the Couette Flow model is more predictive for very high weld pitches. Overall, the Visco-Plastic flow model was more accurate than the Couette Flow model over the range of weld pitches. The Visco-Plastic Flow model also converged with the experimental

results as the weld pitch was increased.

At all weld pitches, the smooth pin model was generally more predictive than the threaded pin model. However it is important to note that the threaded pin model more accurately reflects the experiments because of the pin profile and the inclusion of the backing plate. Also, the threaded pin model did not use a reference pressure as the smooth pin model does.

The threaded pin model can be used to correlate downward material flow to the development of worm holes while the smooth pin model cannot. Appendix B is attached in support of this conclusion.

The threaded pin model can be further improved by accurately determining the appropriate contact condition at the tool pin/material interface. Also, accurately measuring the tool pin sides, bottom, and shoulder temperature separately is believed to further enhance the model predictions.

APPENDIX A

RAW DATA PLOTS

30 ipm

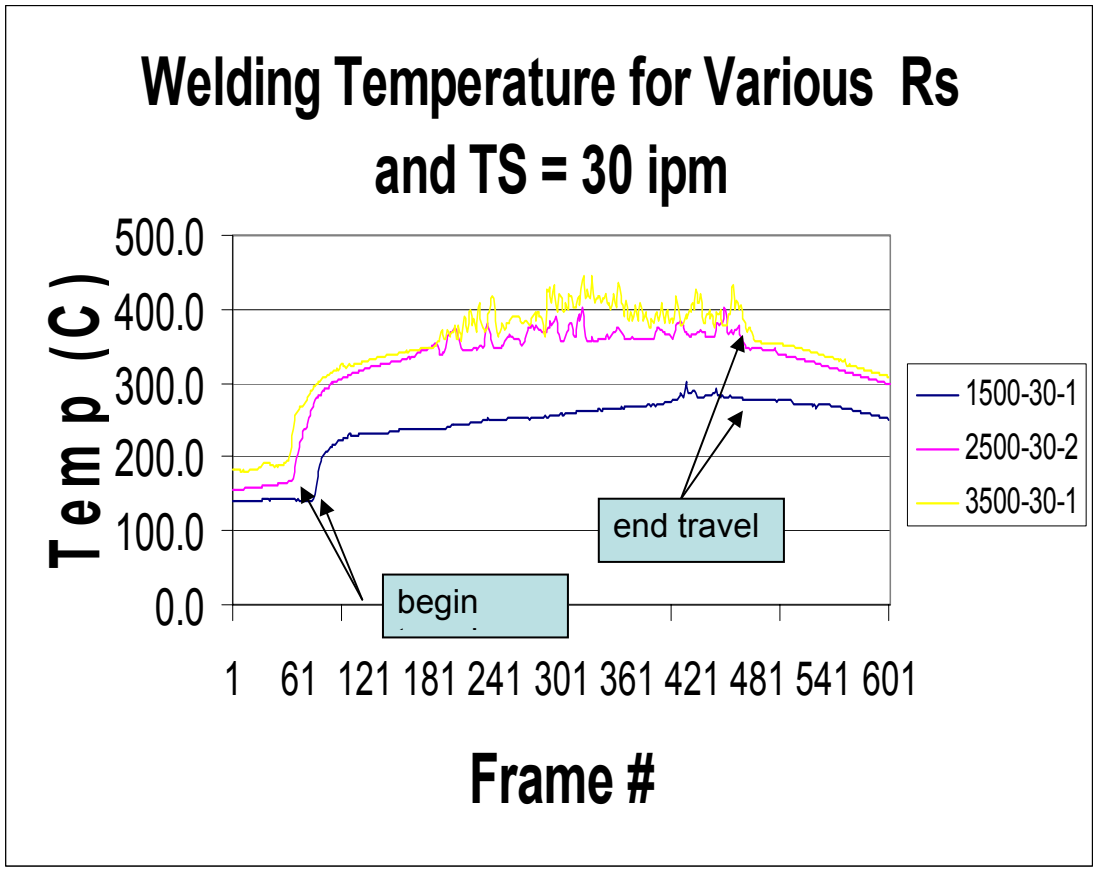

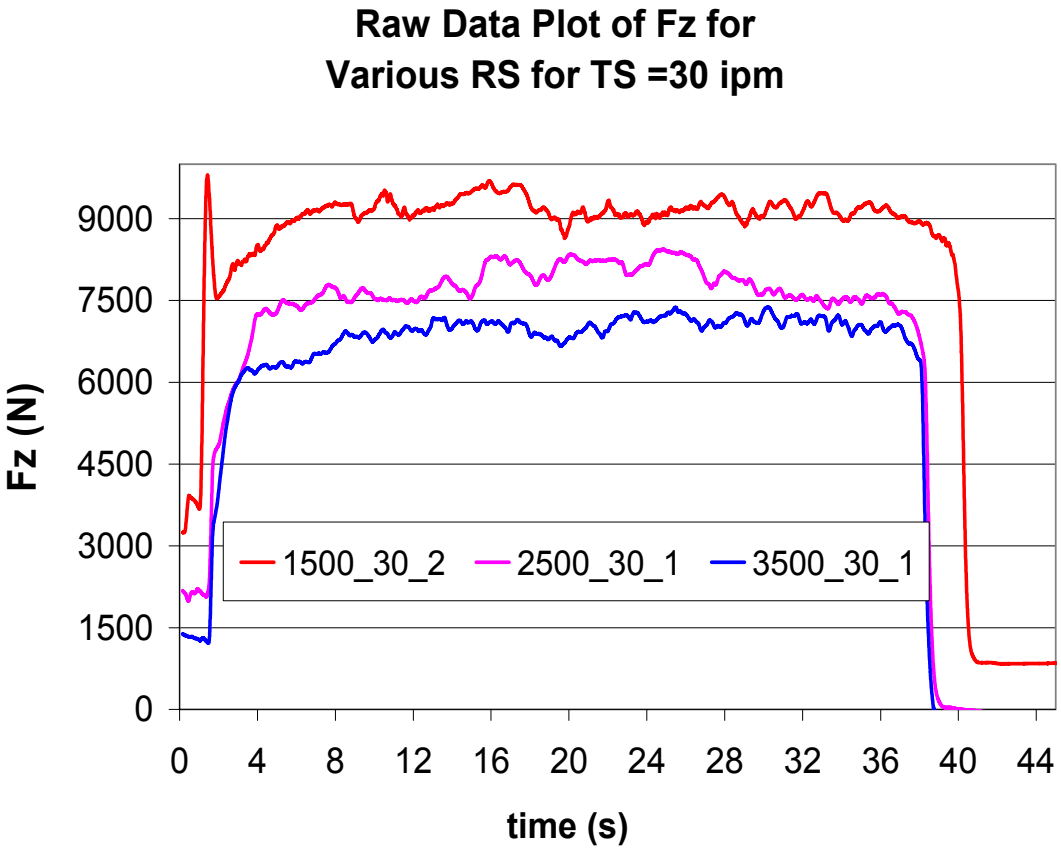
Raw Data Plot of Fz for
Various RS for TS =30 ipm
Fz (N)
9000
7500
6000
4500
3000
1500
0
0
4
8
12
16
20
24
28
32
36
40
44
time (s)
1500_30_2
2500_30_1
3500_30_1

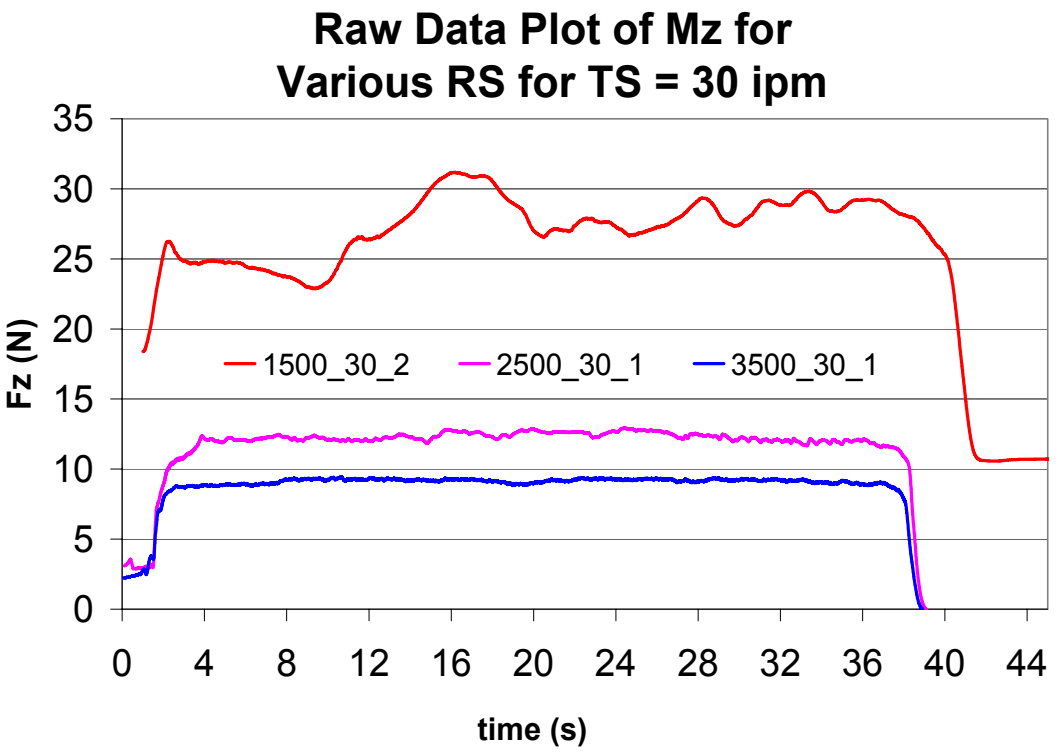
Raw Data Plot of Mz for
Various RS for TS = 30 ipm
Fz (N)
35
30
25
20
15
10
5
0
0
4
8
12
16
20
24
28
32
36
40
44
time (s)
1500_30_2
2500_30_1
3500_30_1

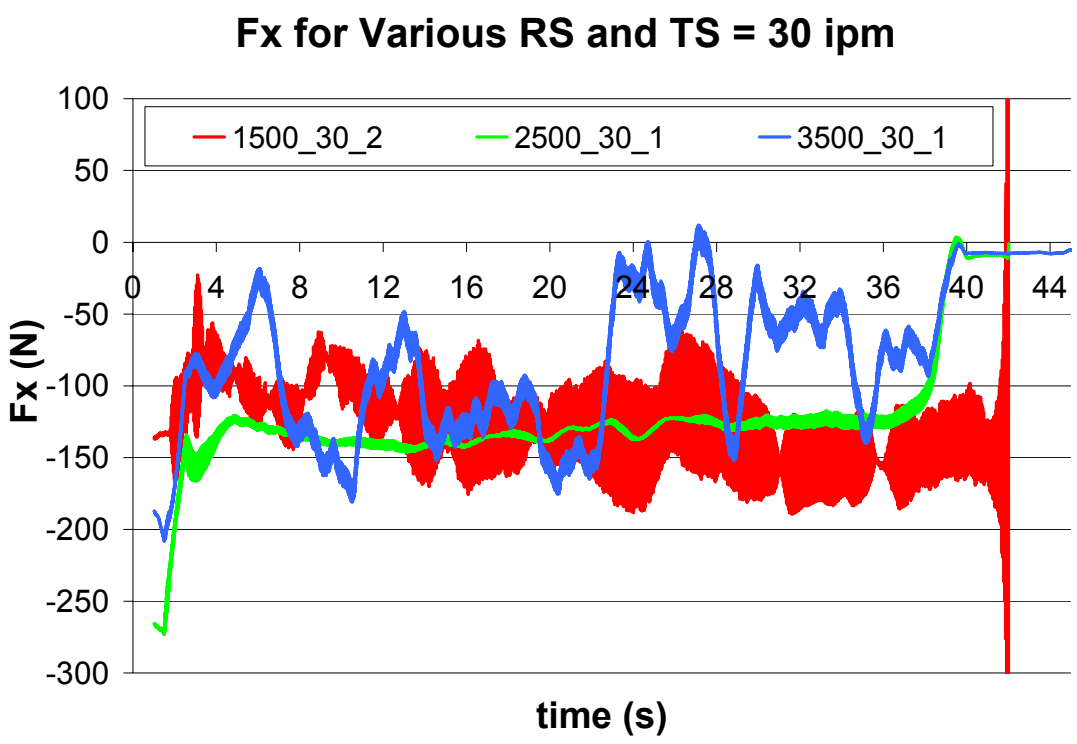
Fx for Various RS and TS = 30 ipm
1500_30_2
2500_30_1
3500_30_1
100
50
0
-50
-100
-150
-200
-250
-300
0
4
8
12
16
20
24
28
32
36
40
44
Fx (N)
time (s)

50ipm

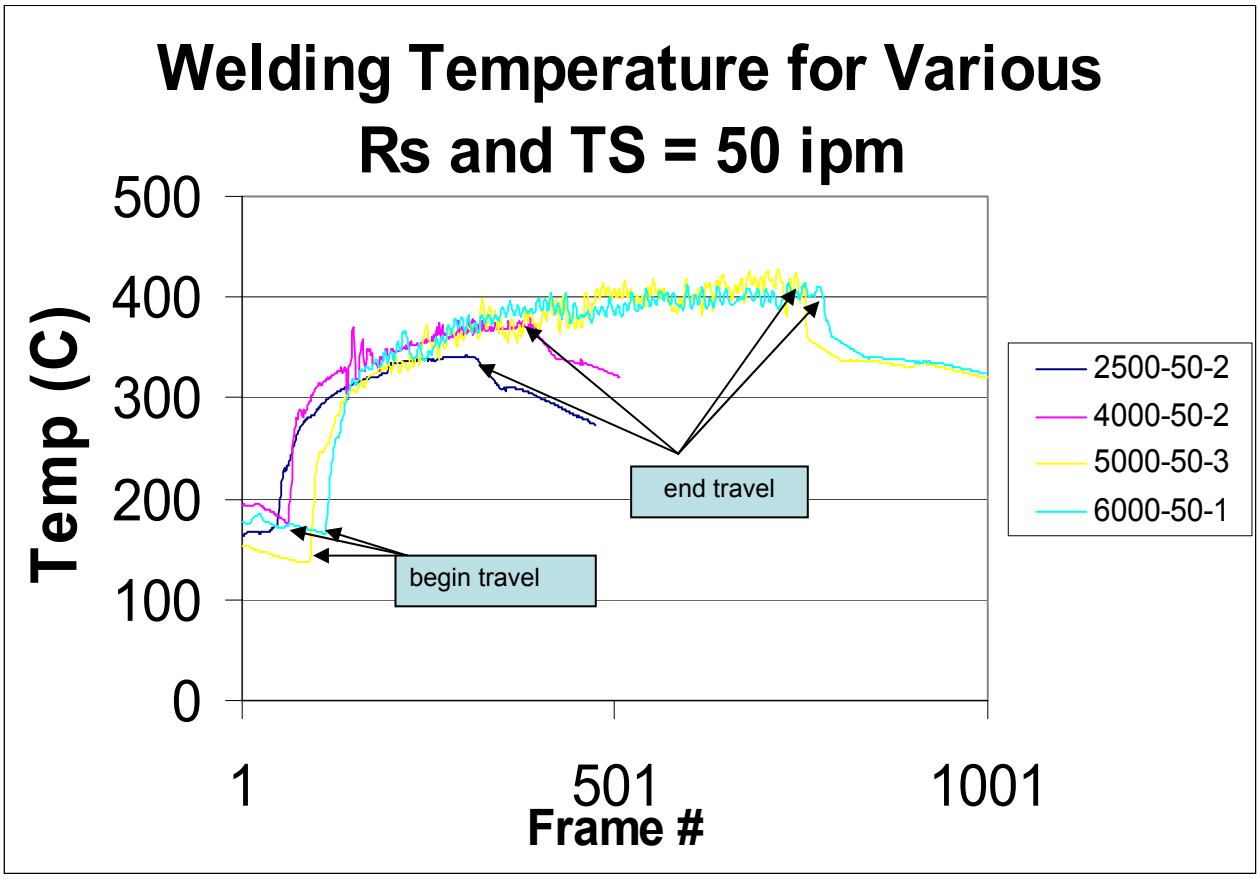
Welding Temperature for Various Rs and TS = 50 ipm
Temp (C)
500
400
300
200
100
0
1
501
1001
Frame #
end travel
begin travel
2500-50-2
4000-50-2
5000-50-3
6000-50-1

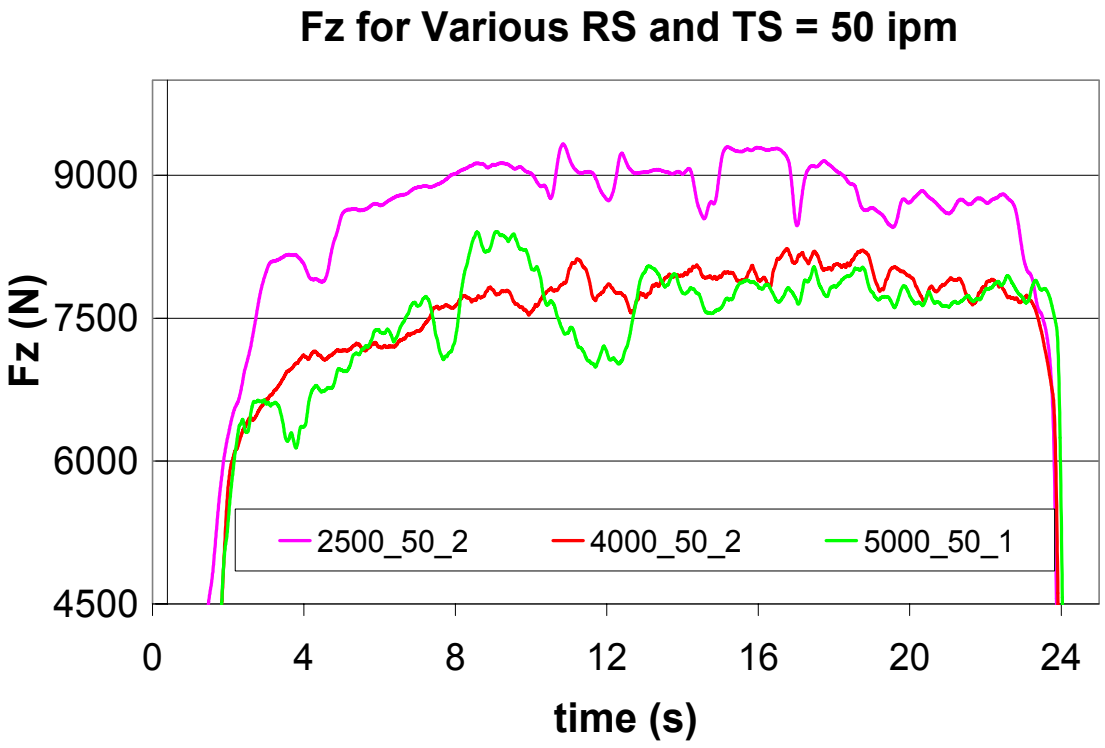
Fz for Various RS and TS = 50 ipm
Fz (N)
9000
7500
6000
4500
0
4
8
12
16
20
24
time (s)
2500_50_2
4000_50_2
5000_50_1

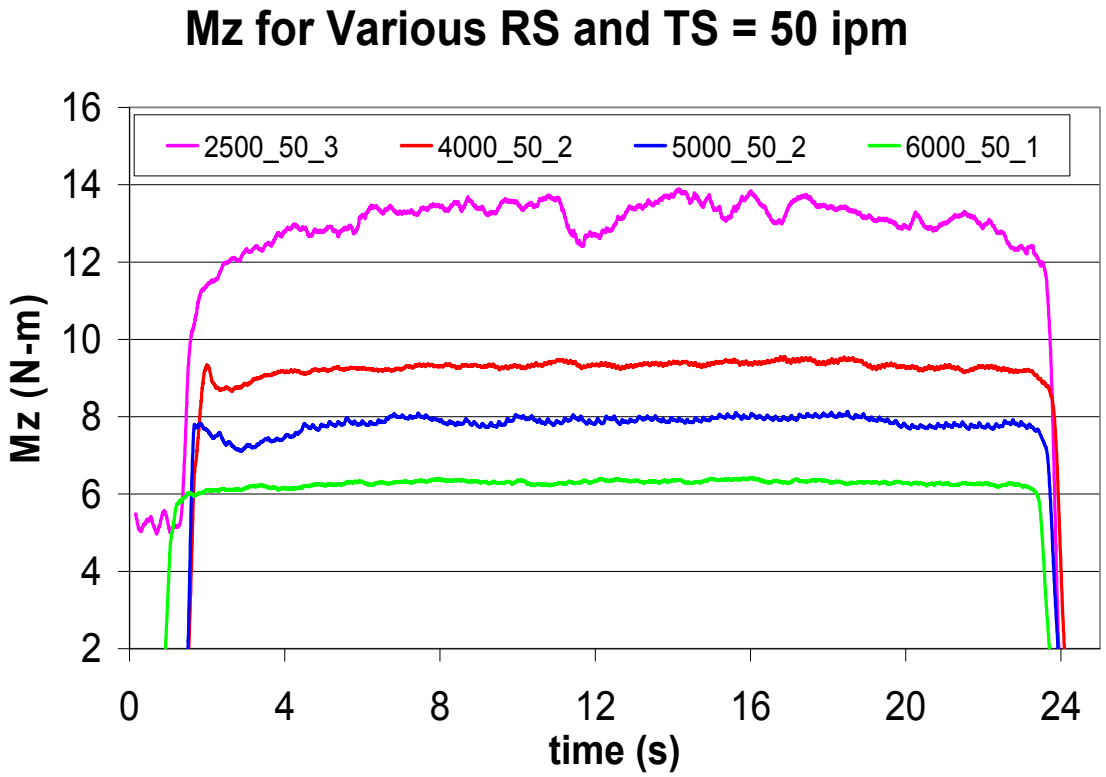
Mz for Various RS and TS = 50 ipm
Mz (N-m)
16
14
12
10
8
6
4
2
0
4
8
12
16
20
24
time (s)
2500_50_3
4000_50_2
5000_50_2
6000_50_1

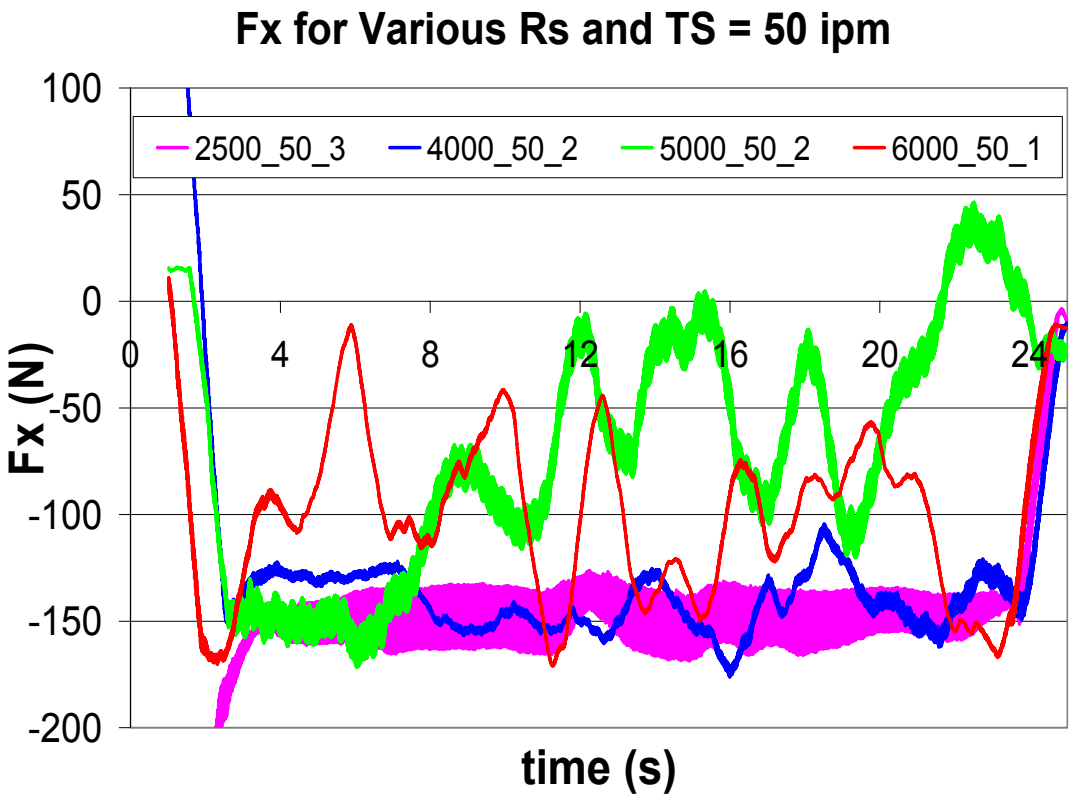
Fx for Various Rs and TS = 50 ipm
2500_50_3
4000_50_2
5000_50_2
6000_50_1
100
50
0
-50
-100
-150
-200
Fx (N)
0
4
8
12
16
20
24
time (s)

70pm

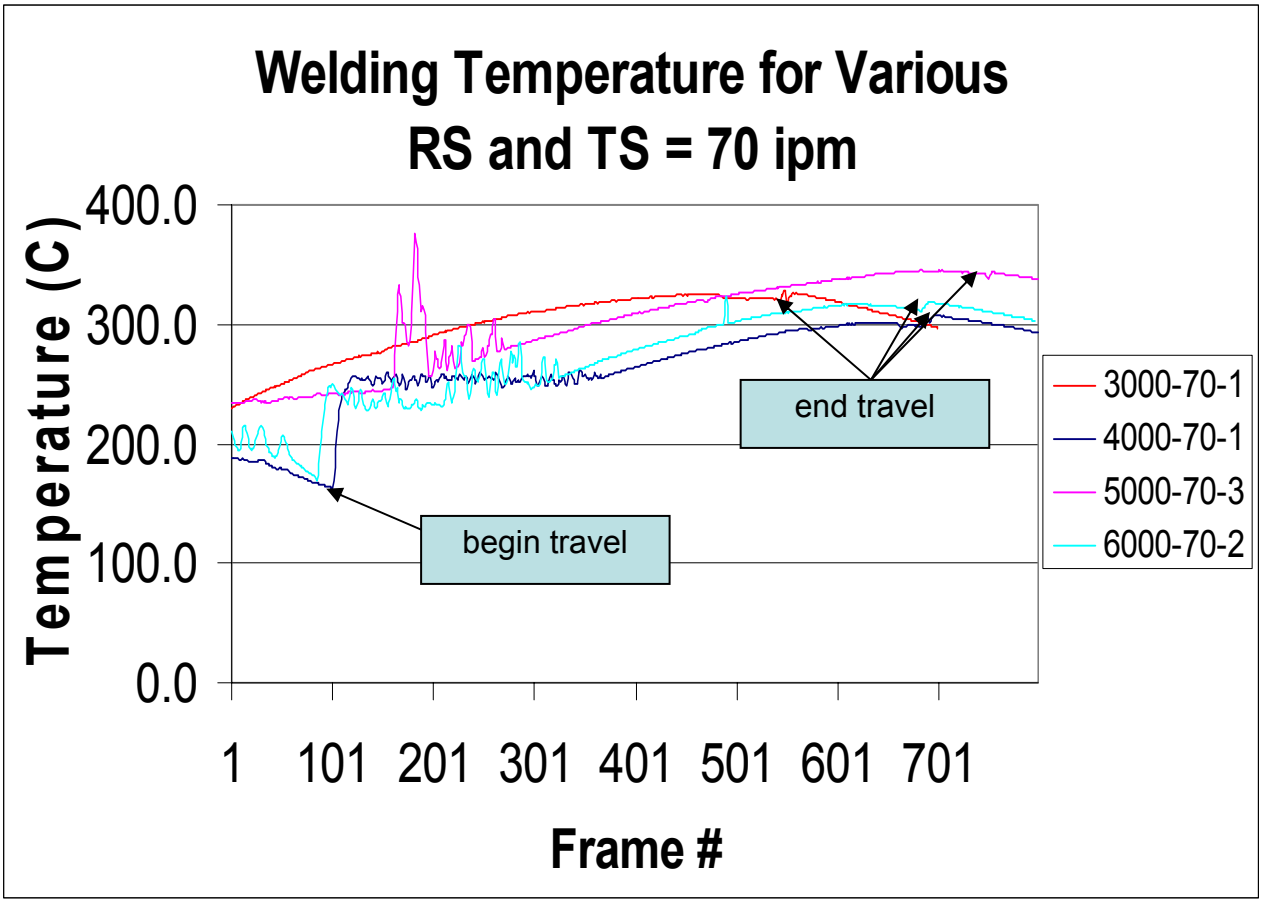
Welding Temperature for Various
RS and TS = 70 ipm
Temperature (C)
400.0
300.0
200.0
100.0
0.0
1
101
201
301
401
501
601
701
Frame #
begin travel
end travel
3000-70-1
4000-70-1
5000-70-3
6000-70-2

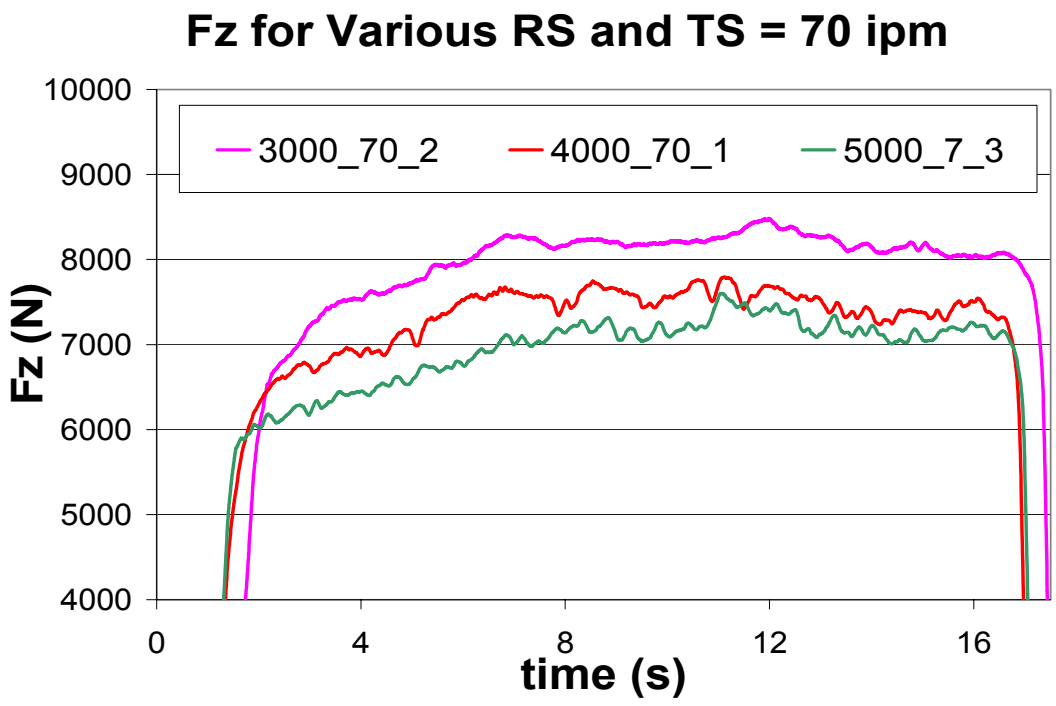
Fz for Various RS and TS = 70 ipm
10000
9000
8000
7000
6000
5000
4000
Fz (N)
3000_70_2
4000_70_1
5000_7_3
0
4
8
12
16
time (s)

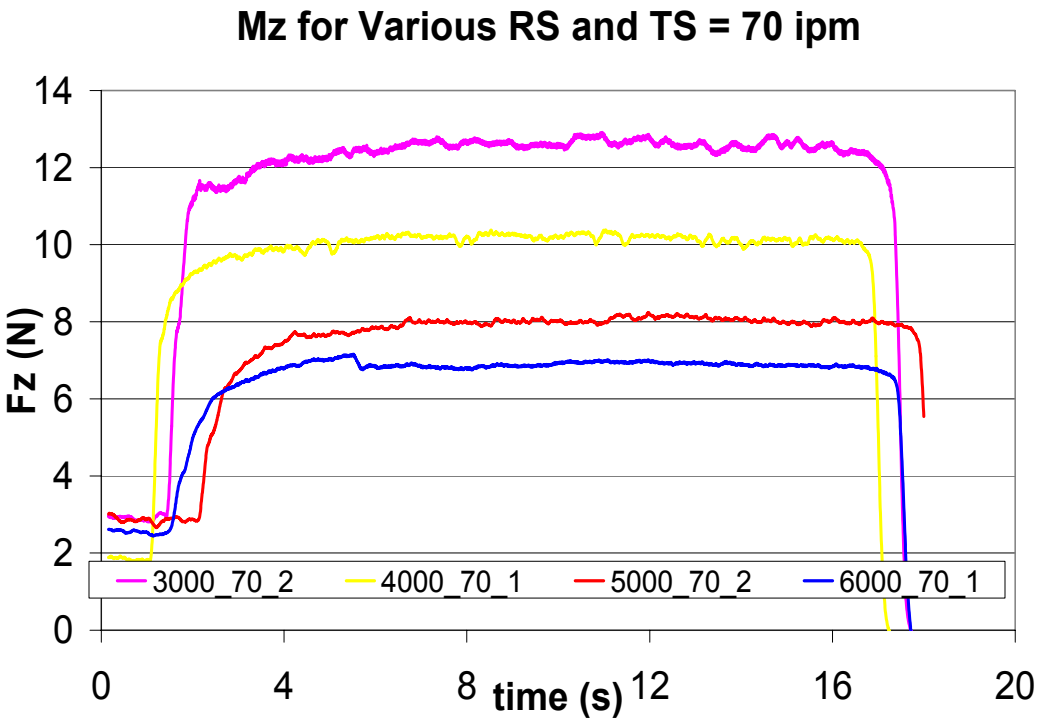
Mz for Various RS and TS = 70 ipm
14
12
10
8
6
4
2
0
Fz (N)
3000_70_2
4000_70_1
5000_70_2
6000_70_1
0
4
8
time (s)
12
16
20

90 ipm

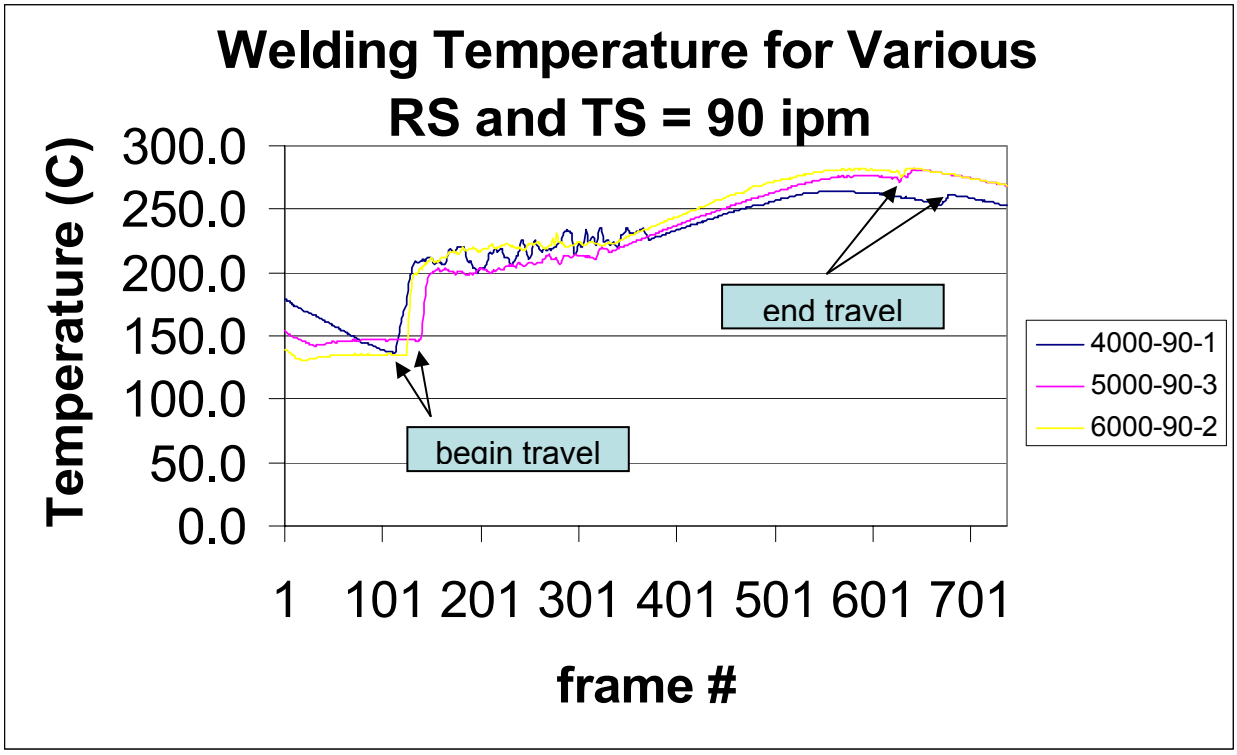
Welding Temperature for Various RS and TS = 90 ipm
Temperature (C)
300.0
250.0
200.0
150.0
100.0
50.0
0.0
1
101
201
301
401
501
601
701
frame #
end travel
begin travel
4000-90-1
5000-90-3
6000-90-2

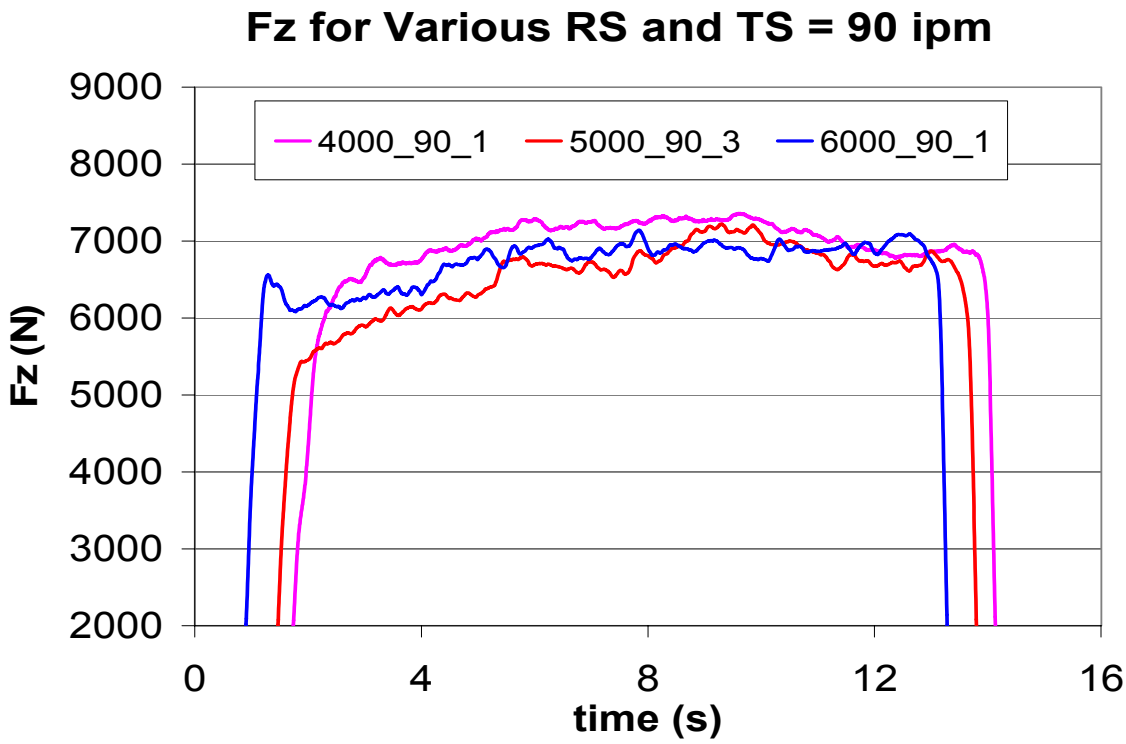
Fz for Various RS and TS = 90 ipm
9000
8000
7000
6000
5000
4000
3000
2000
Fz (N)
4000_90_1
5000_90_3
6000_90_1
0
4
8
12
16
time (s)

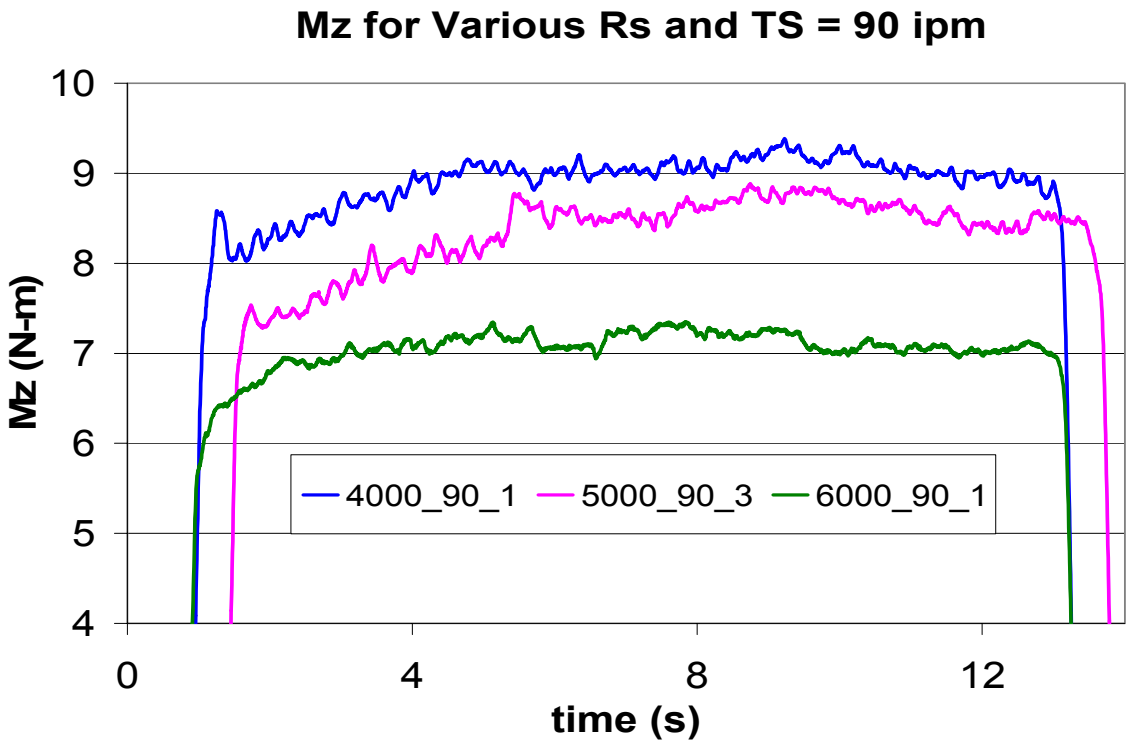
Mz for Various Rs and TS = 90 ipm
10
9
8
7
6
5
4
Mz (N-m)
4000_90_1
5000_90_3
6000_90_1
0
4
8
12
time (s)

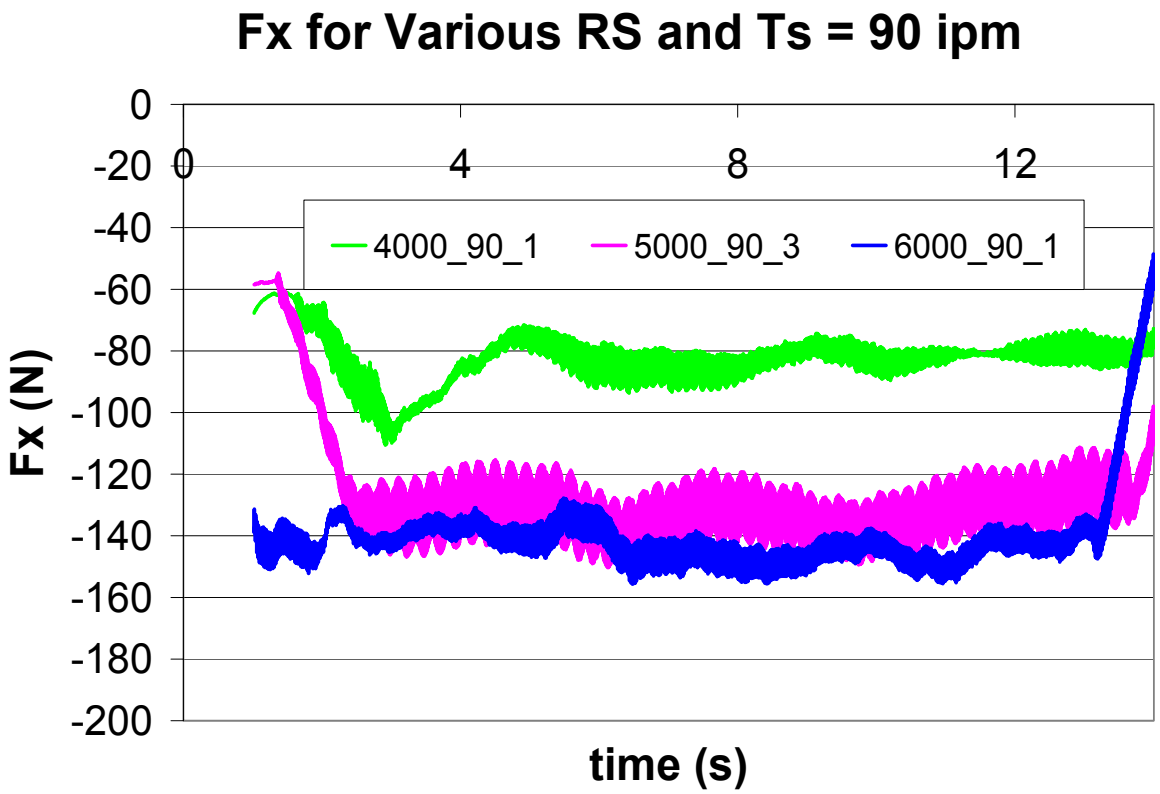
Fx for Various RS and Ts = 90 ipm
0
-20
-40
-60
-80
-100
-120
-140
-160
-180
-200
0
4
8
12
4000_90_1
5000_90_3
6000_90_1
Fx (N)
time (s)

110 ipm

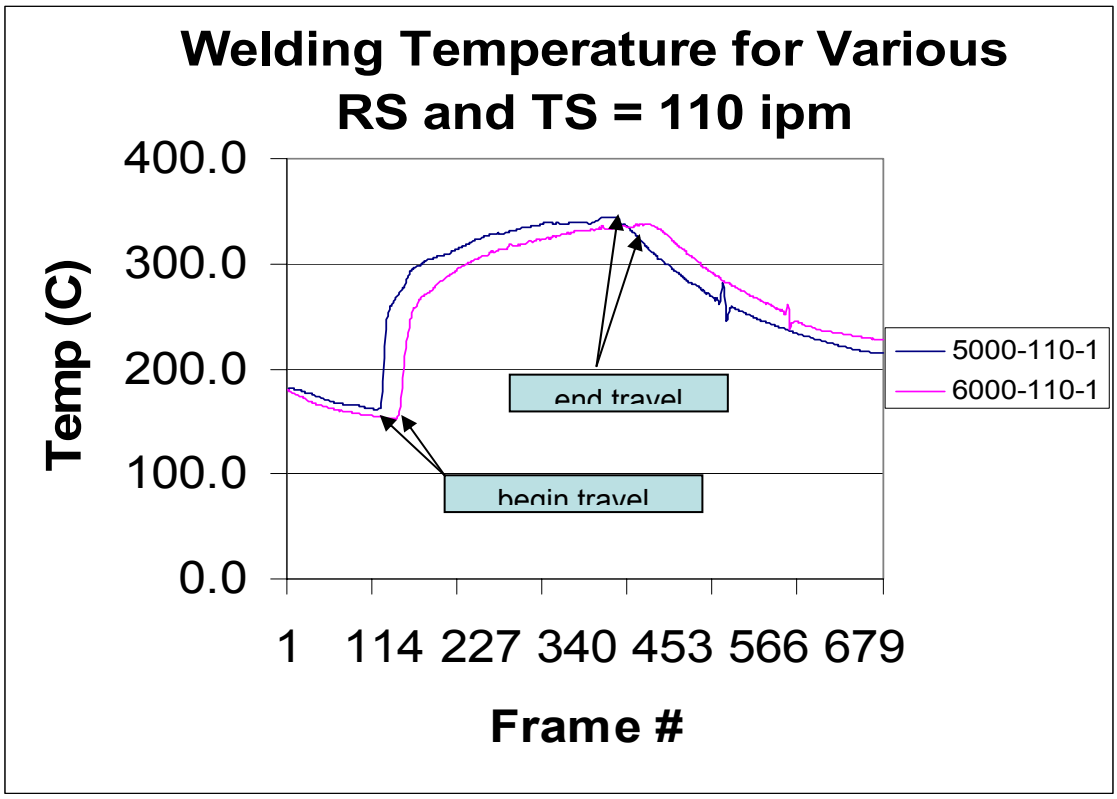
Welding Temperature for Various
RS and TS = 110 ipm
Temp (C)
400.0
300.0
200.0
100.0
0.0
1
114
227
340
453
566
679
Frame #
end travel
begin travel
5000-110-1
6000-110-1

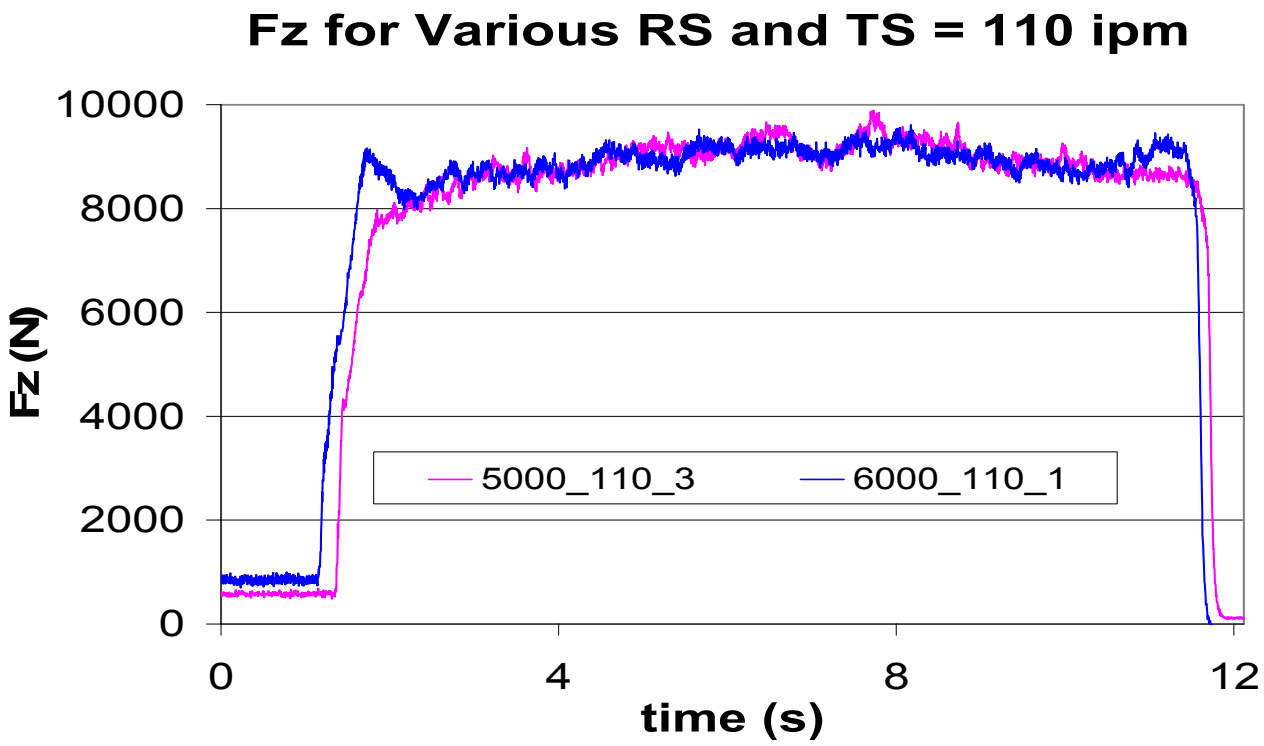
Fz for Various RS and TS = 110 ipm
10000
8000
6000
4000
2000
0
Fz (N)
0
4
8
12
time (s)
5000_110_3
6000_110_1

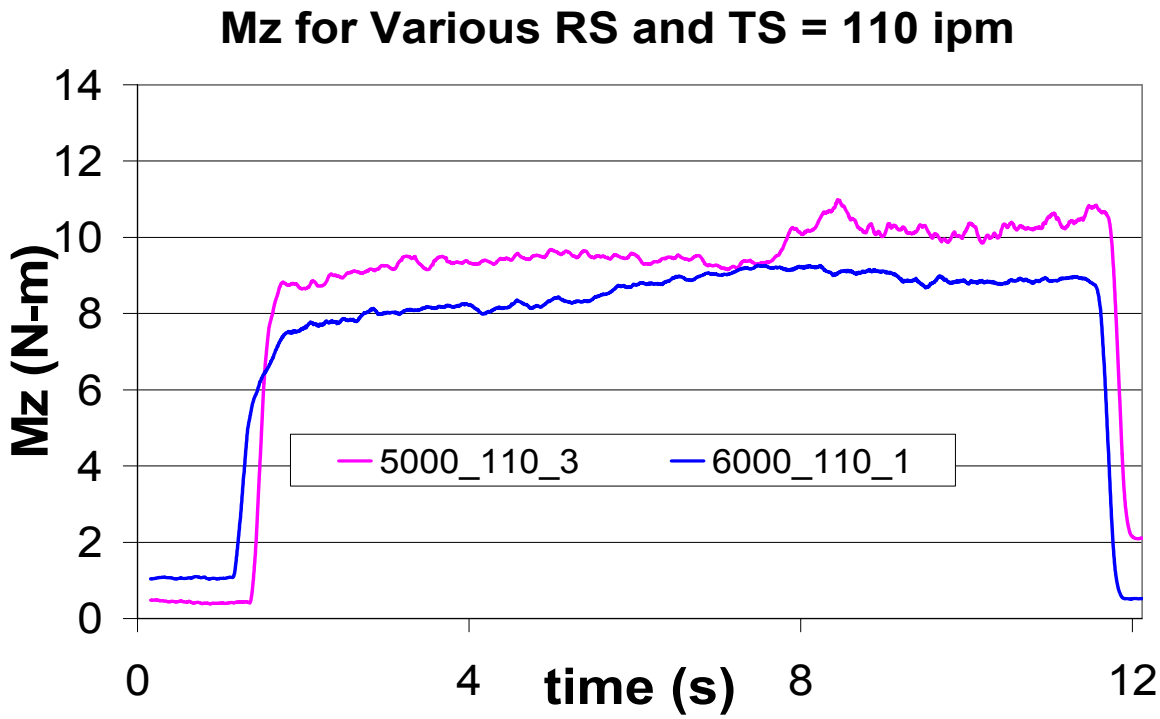
Mz for Various RS and TS = 110 ipm
14
12
10
8
6
4
2
0
Mz (N-m)
0
4
8
12
time (s)
5000_110_3
6000_110_1

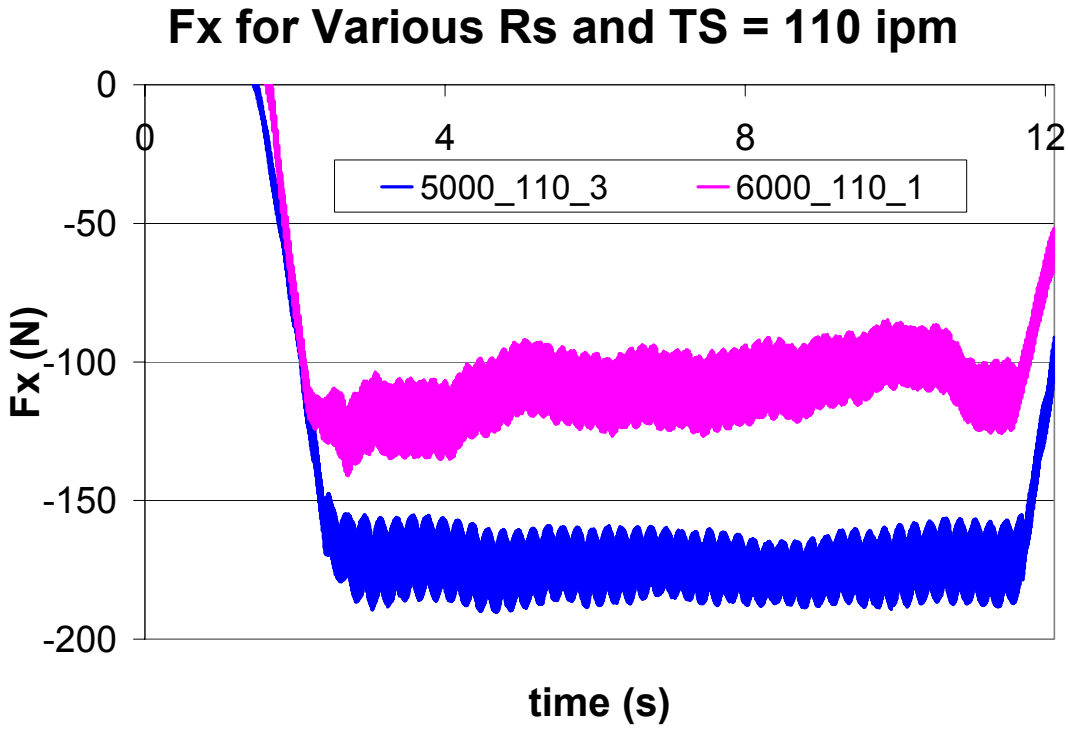
Fx for Various Rs and TS = 110 ipm
0
-50
-100
-150
-200
Fx (N)
0
4
8
12
5000_110_3
6000_110_1
time (s)

120 ipm

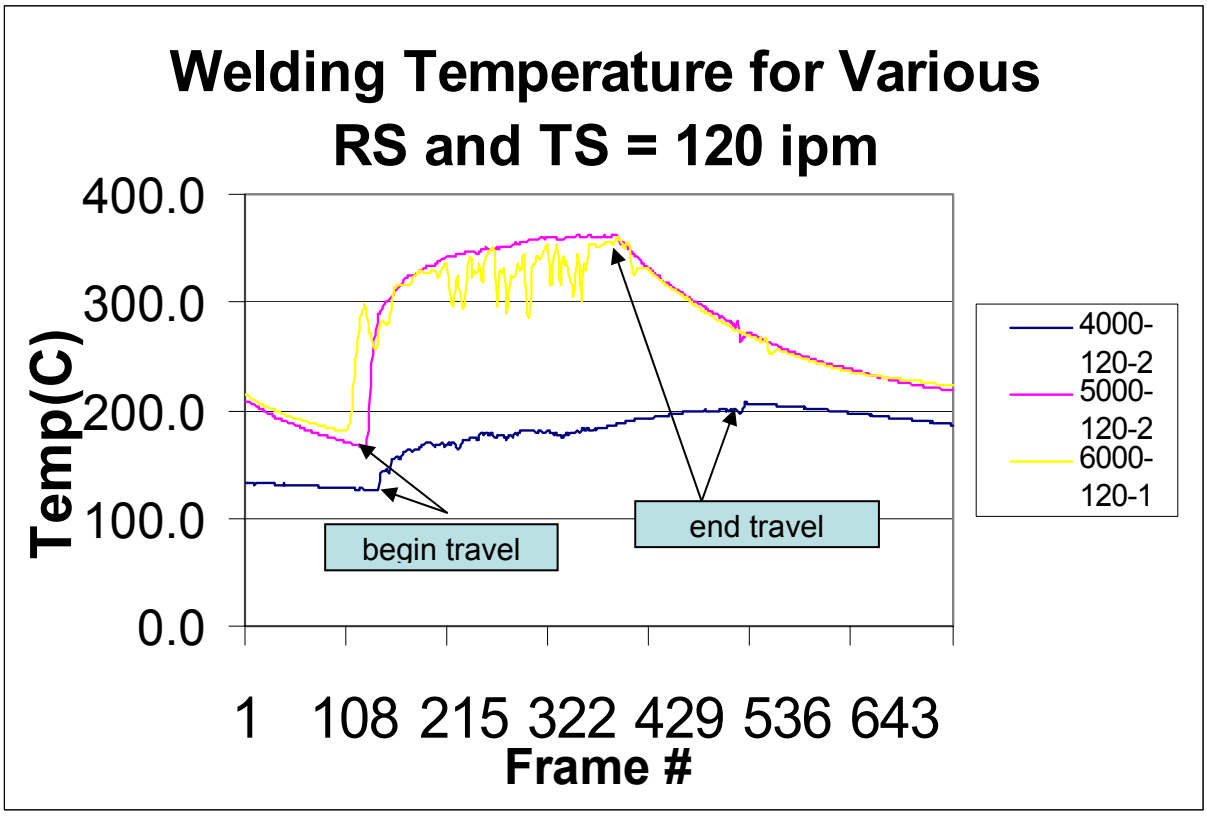
Welding Temperature for Various
RS and TS = 120 ipm
400.0
300.0
200.0
100.0
0.0
Temp(C)
1
108
215
322
429
536
643
Frame #
begin travel
end travel
4000-120-2
5000-120-2
6000-120-1

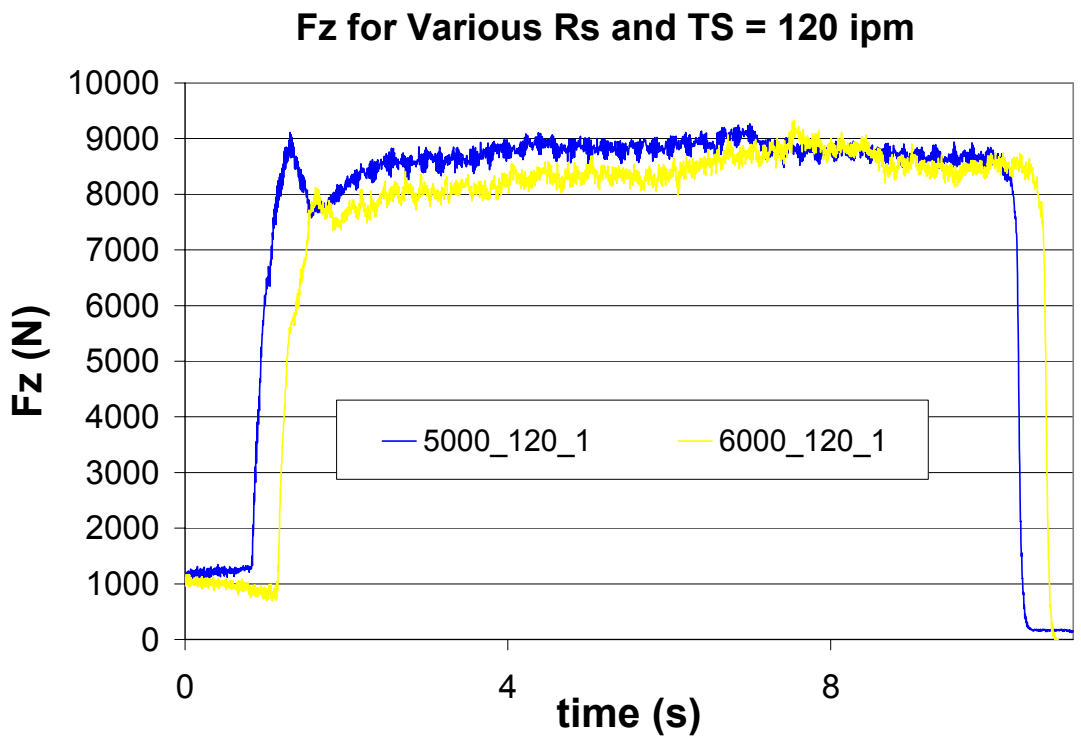
Fz for Various Rs and TS = 120 ipm
10000
9000
8000
7000
6000
5000
4000
3000
2000
1000
0
Fz (N)
0
4
8
time (s)
5000_120_1
6000_120_1

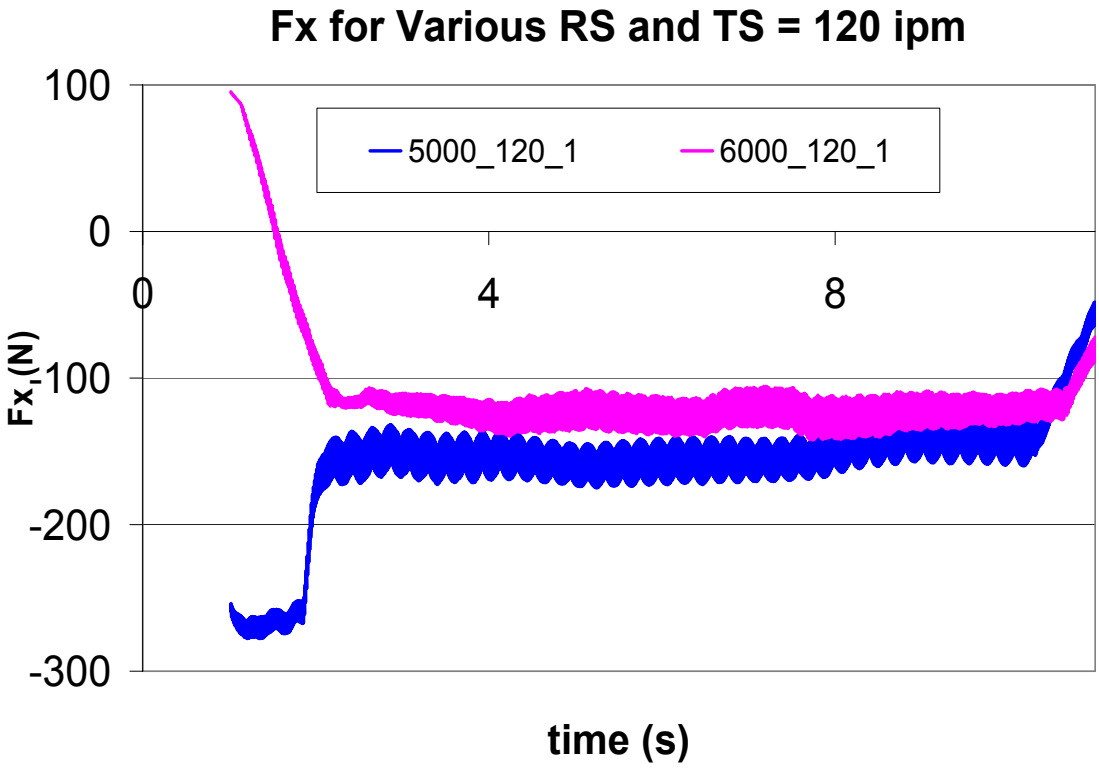
Fx for Various RS and TS = 120 ipm
100
0
-100
-200
-300
Fx (N)
0
4
8
time (s)
5000_120_1
6000_120_1

130 ipm

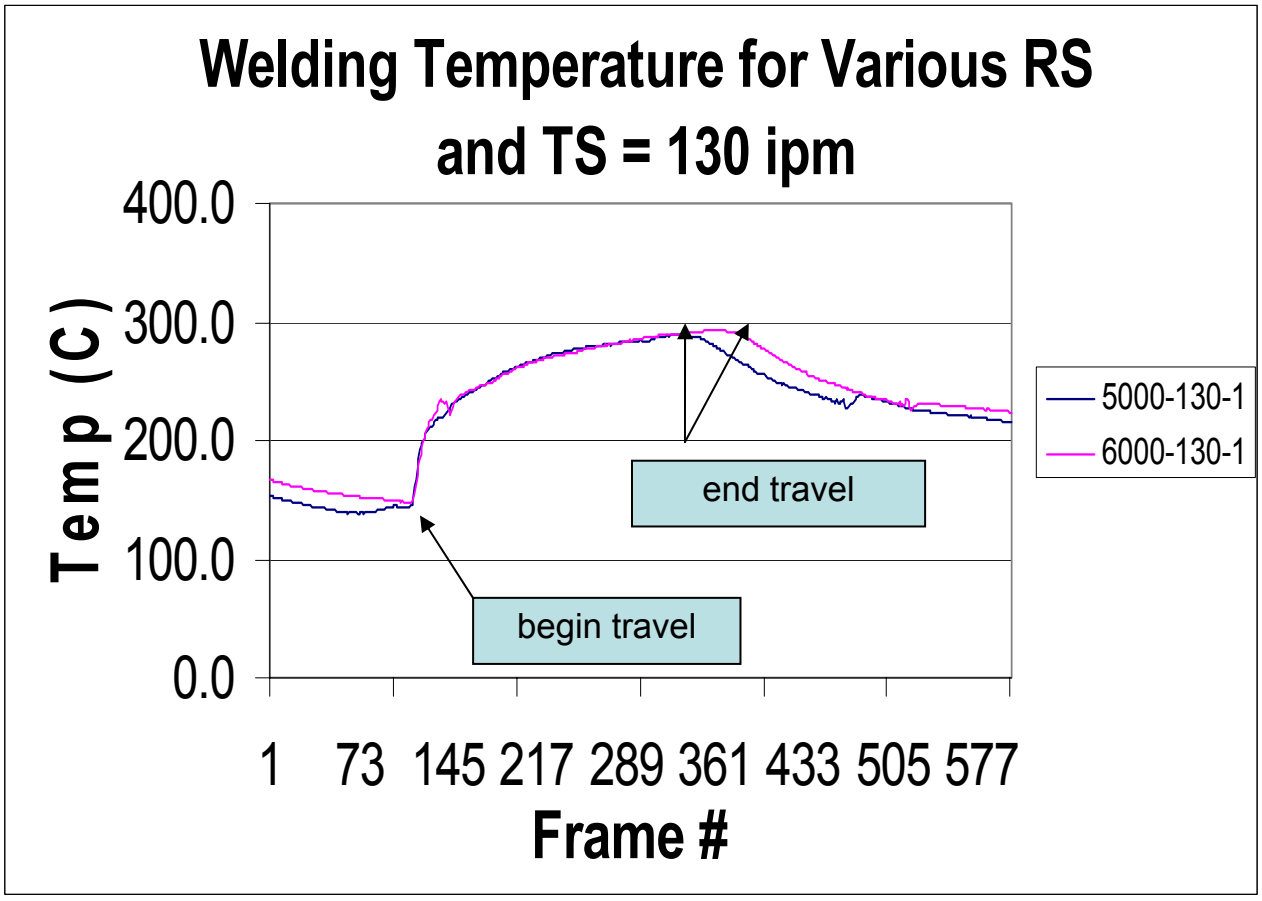
Welding Temperature for Various RS and TS = 130 ipm
Temp (C)
400.0
300.0
200.0
100.0
0.0
1
73
145
217
289
361
433
505
577
Frame #
5000-130-1
6000-130-1
end travel
begin travel

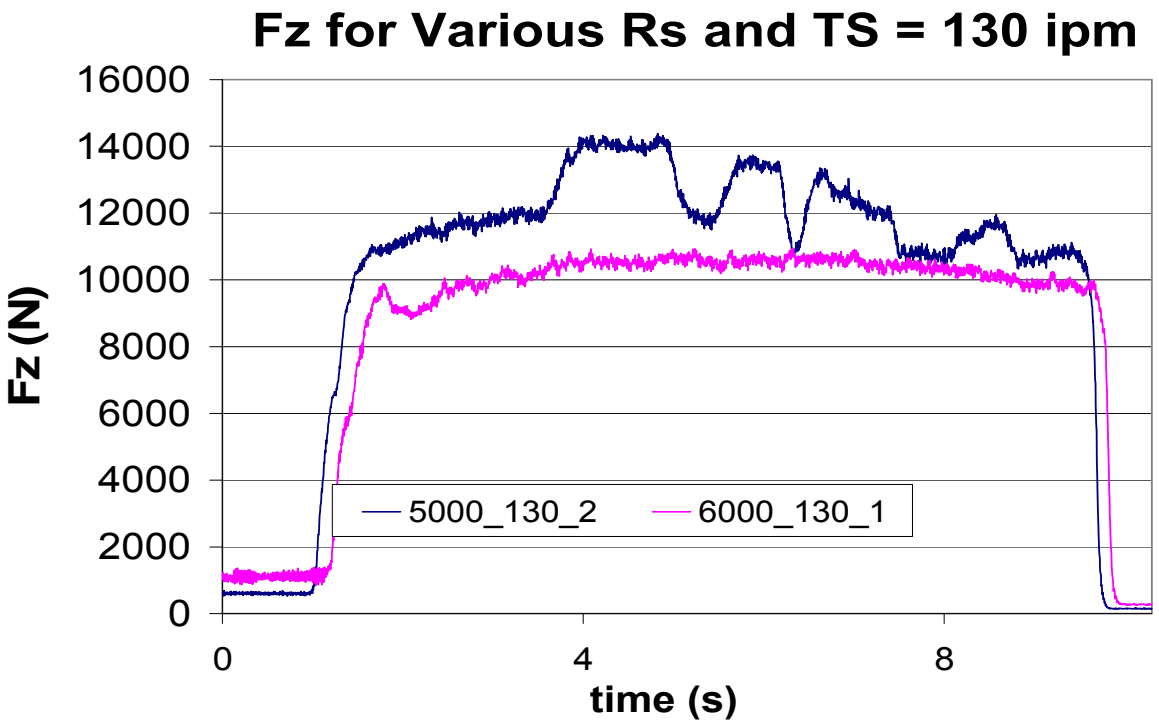
Fz for Various Rs and TS = 130 ipm
16000
14000
12000
10000
8000
6000
4000
2000
0
Fz (N)
0
4
8
time (s)
5000_130_2
6000_130_1

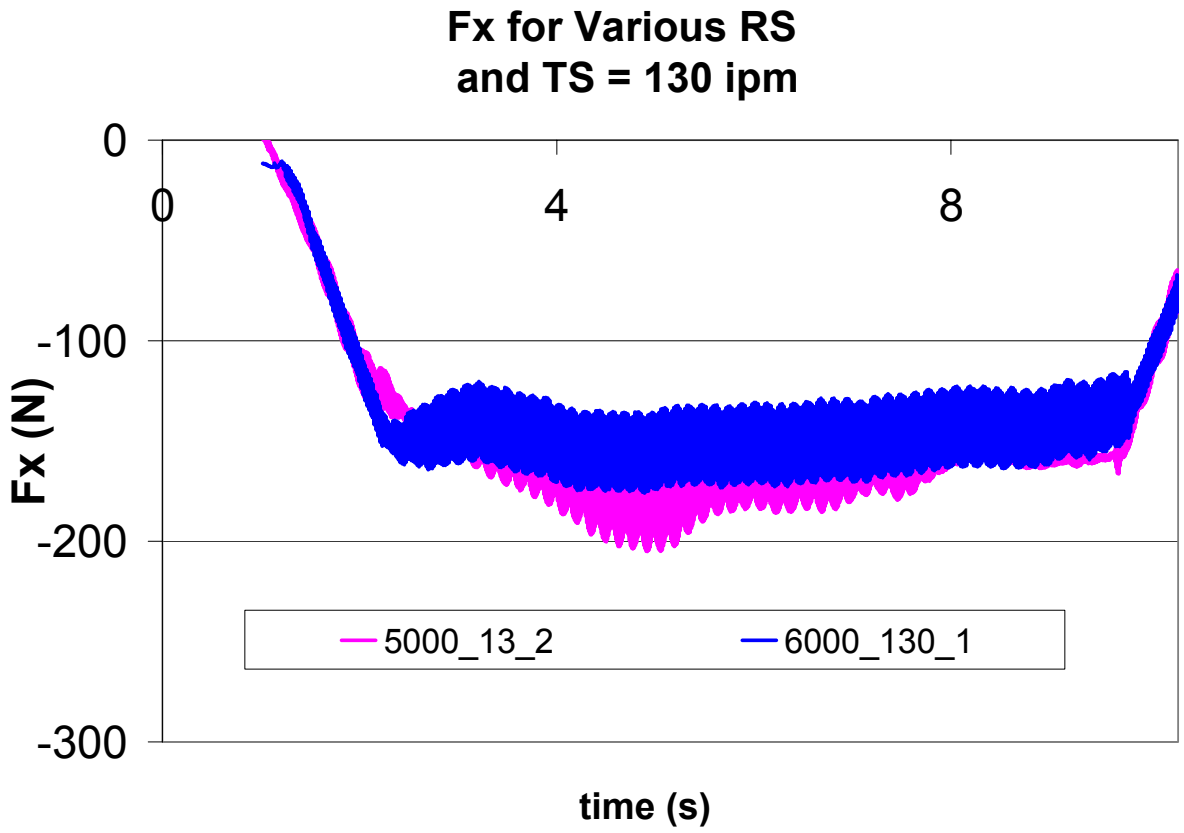
Fx for Various RS
and TS = 130 ipm
0
-100
-200
-300
Fx (N)
0
4
8
time (s)
5000_13_2
6000_130_1

APPENDIX B

NUMERICAL MODEL VERTICAL VELOCITY PREDICTIONS

This Appendix will present a short discussion of pin profile effect on material flow. As stated throughout this dissertation, the tool pin threads are used primarily to induce downward material flow.

In Chapter 7, weld macrographs were presented (Figure 40) which showed worm hole defect formations for 1500 rpm 44.8 and 63.3 ipm. These defects are assumed to form due to a lack of weld material heating and insufficient material flow to the bottom of the weld material. Figures B1 to B4 show simulations of the material flow for the parametric regimes just stated.

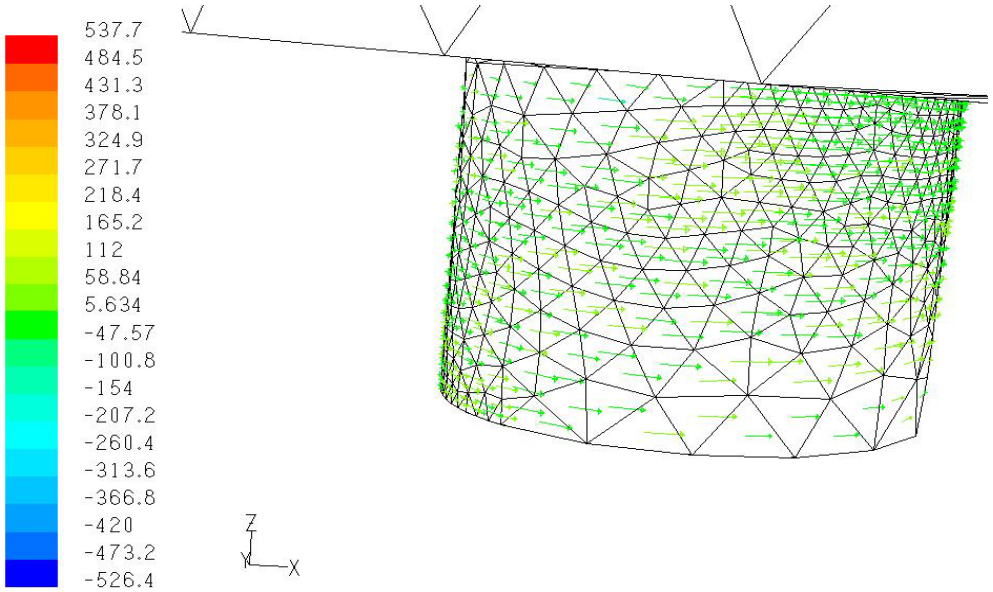

Figure B1: Smooth Pin Z velocity (ipm) for 1500 rpm and 44.8 ipm.

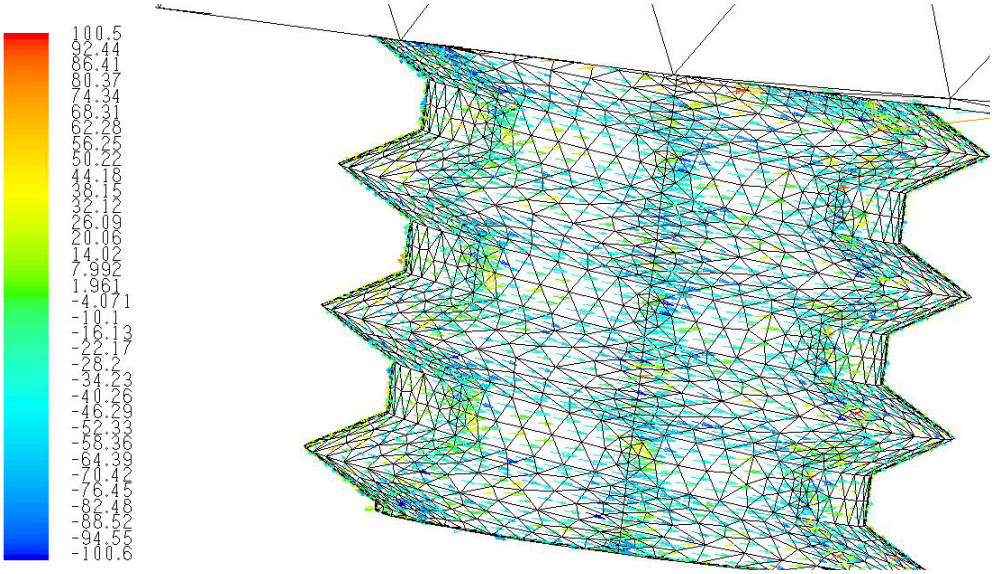

Figure B2: Threaded Pin Z velocity (ipm) for 1500 rpm and 44.8 ipm.

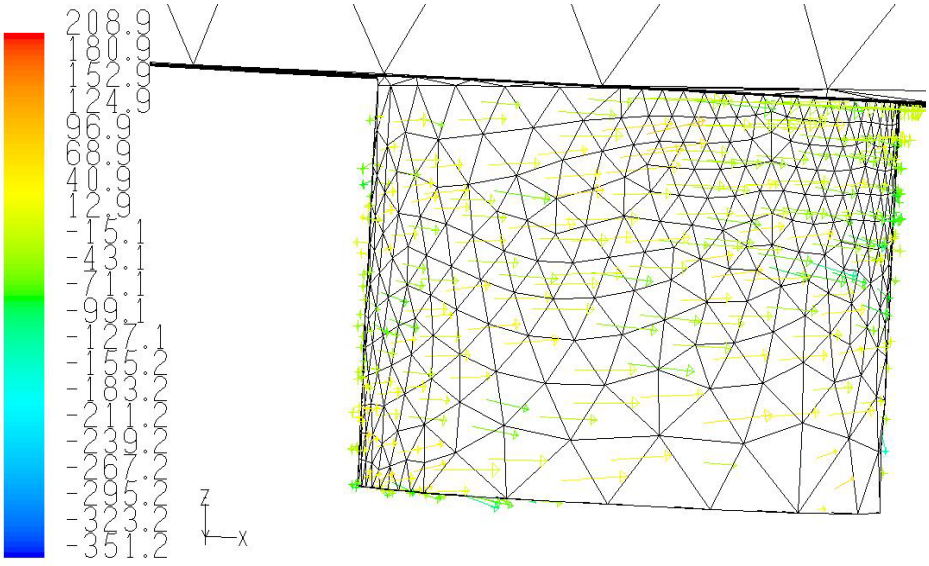

Figure B3: Smooth Pin Z velocity (ipm) for 1500 rpm and 63.3 ipm.

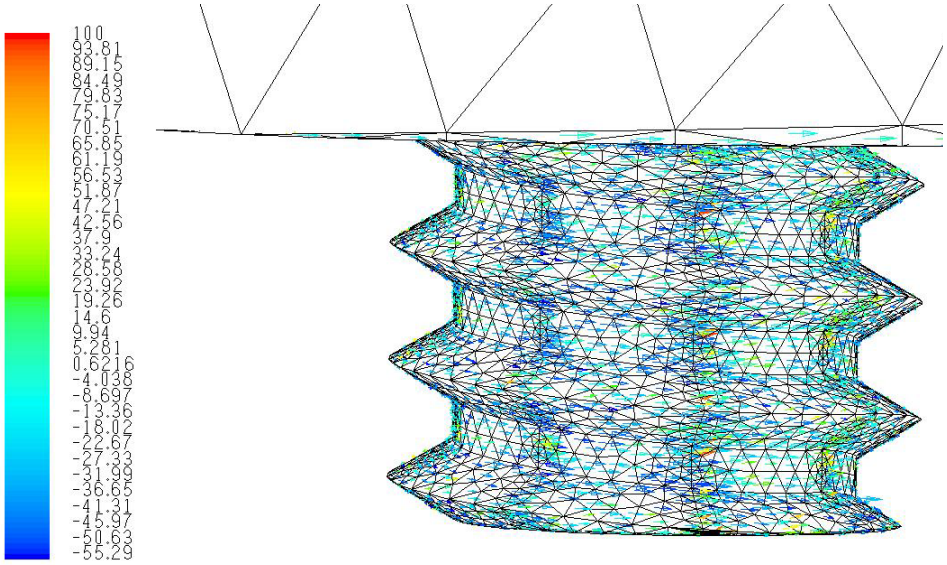

Figure B4: Threaded Pin Z velocity (ipm) for 1500 rpm and 63.3 ipm.

Careful observation of the arrows indicating flow direction in Figures B1 to B4 , show that the smooth pin induces an upward flow while the threaded pin induces a downward flow. The wormholes in Figure 40 were created using a threaded pin. This indicates that while the threaded pin channels material flow downward, there is a minimum velocity at which the magnitude of material flow downward can prove to be insufficient.

This is a limiting factor that is only intensified by using a non-profiled or smooth pin for welding. FSW has not been successfully performed using a smooth tool pin. The minimum weld pitch for FSW at which no wormhole will form using a threaded tool pin is estimated to be is 33 rpi.

REFERENCES

[1] Thomas W.M., et al. 1991, Friction Stir Butt Welding. International Patent Application # PCT/GB92/02203, GB Patent Application #9125978.8, and GB Patent # 2,306,366.

[2] Nicholas E. D., and Kallee, S.W., 2000, "Friction Stir Welding – A decade on." IIW Asian Pacific International Congress. Sydney 29 October to 2 November

[3] http://www.memagazine.org/medes03/coolweld/coolweld.html

[4] Carter, Robert W., *Proceedings of the NASA MSFC Friction Stir Welding Workshop and Showcase, Huntsville, Al, September 2003*

[5] Heideman R. J. et al., 2000, Friction Stir Welding Tool. U.S. Patent #6,053,391

[6] Thomas, W.M., et al., 1995, Friction Welding. U.S. Patent # 5,460,317

[7] Cocks, E. E., et al., 2000, Enantiomorphic Friction-Stir Welding. U.S. Patent # 6,029,879.

[8] Su, J. Q., 2003, *Acta Materialia*, **51**, 713-729.

[9] Lee, W.-B., Schmuecker, M., Mercardo, U.A., Biallas, G. and Jung, S.-B., 2006, *Scripta Materialia,* **55**, 355–358.

[10] Mahoney, M.W., Rhodes, C.G., Flintoff, J.G., Spurling, R.A. and Bingel, W.H., 1998, *Metall. Mater. Trans. A*., **29A**, 1955-64.

[11] Heinz, B., Skrotzki, B. and Eggler, G., 2000, *Mater. Sci. Forum*., **331–337**, 1757-62.

[12] Svensson, L.E., Karlsson, L., Larsson, H., Karlsson, B., Fazzini, M. and Karlsson, J., 2000, *Sci. Technol. Welding Joining*, **5**, 285-296.

[13] Reynolds, A.P., Lockwood, W.D. and Seidel, T.U., 2000, *Mater. Sci. Forum.,* **331–337**, 1719-24.

[14] Lumsden, J.B., Mahoney, M.W., Pollock, G. and Rhodes, C.G., 1999, *Corrosion*, **55**, 1127-1135.

[15] Murr, L.E., Liu, G. and McClure, J.C., 1998, *Mater. Sci.,* **33**, 1243-1251.

[16] Rhodes, C.G., Mahoney, M.W, Bingel, W.H., Spurling, R.A. and. Bampton, C.C., 1997, *Scripta Mater.,* **36**, 69-75.

[17]. Jata, K.V., Sankaran, K.K. and Ruschau, J.J., 2000, *Metall. Mater. Trans. A,* **31A**,

2181-2192.

[18] Liu, G., Murr, L.E., Niou, C.S., McClure, J.C. and Vega, F.R., 1997, *Scripta Mater.,* **37**, 355-361.

[19] Sato, Y.S., Kokawa, H., Enomoto M. and Jogan, S., 1999, *Metall. Mater. Trans. A,* **30A**, 2429-2437.

[20] Su, J.-Q., Nelson, T.W., Mishra, R. and Mahoney, M., 2003, *Acta Mater.,* **51**, 713-729.

[21] Kwon Y.J., Shigematsu, I. and Saito, N., 2003, *Scripta Materialia.,* **49**, 785-789.

[22] Lee W. B., Yeon, Y. M. and Jung, S. B., 2003, *Materials Science and Technology*, **19**, 1513 – 1518.

[23] Ulysse, P., 2002, *International Journal of Machine Tools & Manufacture*., **42**, 1549–1557

[24] FIDAP, Fluid Dynamic Analysis Package, version 7.6, Fluid Dynamics International, Evanston, IL. 2002

[25] Reynolds A. P., Deng X., Seidel T. and Xu S., 2000, *Proc. Joining of Advanced and Specialty Materials* (St Louis, MO, ASM International) pp 172–177.

[26] Colegrove P., 2000, *2nd Int. Symp. on Friction Stir Welding (Gothenburg, Sweden)*

[27] Shercliff, H. R. and Colgrove, P. A., 2002, *Math. Modelling Weld. Phenom.,* **6**, 927–974.

[28] Shmidt, H., Hattel, J. and Wert, J., 2004, *Modeling and Simulation in Materials Science and Engineering*, **12**, 143–157.

[29] Colligan, K., 1999, *Welding Journal*, **6**, 229 –237.

[30] Chen C.M. and Kovacevic, R., 2003, *International Journal of Machine Tools & Manufacturing,* **43**, 1319–1326.

[31] Nunes A.C., Bernstien, E.L. and McClure, J.C., 2000, *Proc. of the 81st American Welding Society Annual Convention*, Chicago, IL.

[32] Mitchell, J., 2002, *Experimental Thermo-mechanics of Friction Stir Welding,* M.S.

Thesis, Vanderbilt University, Nashville, Tennessee.

[33] Heurtier, P., Jones, M.J., Desrayaud, C., Driver, J.H., Montheillet, F. and Allehaux, D., 2006, *Journal of Materials Processing Technology*, **171**, 348–357.
[34] Buffa, G., Hua, J., Shivpuri, R. and Fratini, L., 2006, *Materials Science and Engineering A,* **419**, 381–388.

[35] Buffa, G., Hua, J., Shivpuri, R. and Fratini, L., 2006, *Materials Science and Engineering A,* **419**, 389–396.

[36] Nandan, R., Roy, G.G. and Debroy, T., 2006, *Metallurgical and Materials Transactions A,* **37A**, 1248-1259.

[37] Guerra M., Schmidt, C., McClure, J.C., Murr, L.E. and Nunes, A.C., 2003, *Materials Characterization*., **49**, 95-101.

[38] Zhao, Y.-H., Lin, S.-B. , Qu, F.-X., and Wu L., 2006, *Materials Science and Technolo*gy, **22 (1)**, 45-50.

[39] Schmidt, H.N.B, Dickerson, T.L. and Hattel, J.H., 2006, *Acta Materialia*, **54**, 1199–1209.

[40] Crawford, R., 2005, *Parametric Quantification of Friction Stir Welding,* M.S. Thesis, Vanderbilt University, Nashville, Tennessee.

[41] North, T. H., Bendzsak, G.J. and Smith, C., 2000, *Proc. 2nd Int. Symp. on Friction Stir Welding*, Gothenburg, Sweden.

[42] Mills, K.C., 2002, *Recommended Values of thermophysical properties for commercial alloys*, Cambridge, UK.

[43] Arbegast, W. and Braun, G.F., 2000, *Proc. 11th Annual Advanced Aerospace Materials and Processes Conference and Symposium*, Seattle, Wa.

[44] Schmidt, H., Hattel, J. and Wert, J., 2004, *Modeling and Simulation in Materials Science and Engineering*, **12**, 143–157.

[45]. Cook, G.E., Crawford, R., Clark, D.E. and Strauss, A.M, 2004, *The Industrial Robot*, **31(1)**, 55-63.

[46] Talia, G. E. and Chaudhuri, J., 2004, *Department of Mechanical Engineering Presentation*. Wichita State University.

[47] De Schutter, J. and Van Brussel, H., 1988, *International Journal of Robotics Research*, **7(4)**, 3-33.

[48] FLUENT, Fluid Dynamic Analysis Package, version 6.122 Fluid Dynamics International, Evanston, IL.